Development and application of functional composite surfaces with tunable wettability and photoreactivity

PhD dissertation

László Mérai

Chemistry MSc – specialization in quality control

Supervisor:

Dr. László Janovák

senior lecturer

Doctoral School of Chemistry

Department of Physical Chemistry and Materials Science

University of Szeged - Faculty of Science and Informatics

2022

Szeged, Hungary

Table of contents

List of abbreviations

μCT – micro X-ray computed tomography

AgNP – silver nanoparticle

Ag-TiO_2 – silver-doped titanium dioxide (visible light-active plasmonic photocatalyst)

Ag-TiO_2/FP – composite of Ag-TiO_2 and FP

Ag-TiO_2/FP+pHEA – composite of Ag-TiO_2, FP and pHEA

Ag-TiO_2/PDMS oleogel – composite of Ag-TiO_2 and silicone oil-infused PDMS oleogel

Ag-TiO_2/PDMS-co-INI – composite of Ag-TiO_2, cFe and PDMS

Ag-TiO_2/PDMS-gr-PNIPAAm – composite of Ag-TiO_2 and pNIPAAm-grafted PDMS

Ag-TiO_2+cFe/PDMS – composite of Ag-TiO_2, cFe and PDMS

ARGET-ATRP – activators regenerated by electron transfer – atom transfer radical polymerization

ATRP – atomic transfer radical polymerization

BET – Brunauer-Emmett-Teller (method for specific surface area determination)

C_6D_6 – deuterated benzene

cFe – carbonyl iron

d.H_2O – deionized water

$DDSiCl_3$ – dodecyltrichlorosilane

DR – diffuse reflectance

DSC – differential scanning calorimetry

EDX – energy-dispersive X-ray spectroscopy

FP – solids content of the Capstone ST-110 aqueous cationic fluoropolymer dispersion

HEA – 2-hydroxyethyl acrylate

INI – 10-undecenyl 2-bromoisobutyrate

L/G – liquid/gas (interface)

LCD – liquid crystal display

LCST – lower critical solution temperature

LDO – layered double oxide

LED – light-emitting diode

MB – methylene blue

NIPAAm – N-isopropylacrylamide

NMR – nuclear magnetic resonance

PDMS – poly(dimethylsiloxane)

PDMS-co-INI – copolymer of PDMS and INI

PDMS-gr-PNIPAAm – pNIPAAm-grafted PDMS

pHEA – poly(2-hydroxyethyl acrylate)

PMDETA – *N*,*N*,*N*′,*N*″,*N*′-Pentamethyldiethylenetriamine

pNIPAAm – poly(N-isopropylacrylamide)

PZC – point of zero charge

RAFT – reversible addition-fragmentation chain-transfer

r-FP – composite consisting of of 80 wt.% Ag-TiO_2 and 20 wt.% FP

RLU – relative light unit

r-pHEA – composite consisting of of 80 wt.% Ag-TiO_2 and 20 wt.% pHEA

rt. – room temperature

s.a. – sliding angle

S/G – solid/gas (interface)

S/L – solid/liquid (interface)

SEM – scanning electron microscopy

SLIPS – slippery liquid-infused porous surfaces

TEM – transmission electron microscopy

TG – thermogravimetry

UCST – upper critical solution temperature

UV – ultraviolet (radiation)

UV-VIS – ultraviolet-visible (range of electromagnetic radiation)

VIS – visible (radiation)

VOC – volatile organic compound

XPS – X-ray photoelectron spectroscopy

Θ – contact angle

Θ_{adv} – advancing contact angle

Θ_{rec} – receding contact angle

List of figures and tables

1. Introduction

The popularity of functional surfaces with extreme wetting properties and liquid manipulation capabilities is rapidly increasing, as they offer new perspectives to various fields, such as microfluidics, analytics, environmental protection, and healthcare. Ranging from the well-known, lotus-inspired superhydrophobic self-cleaning surfaces to superhydrophilic antifogging glasses and mirrors, these materials also offer application possibilities for everyday users.

The elaboration of extreme wetting properties requires not only the right choice surface chemistry, but the presence of hierarchical, micro- and nanoscale surface roughness, as well, which – among many possibilities – can be achieved through enhancing the inherently hydrophobic or hydrophilic surfaces with particulate materials. Depending on the properties of these roughening agents, the resulting composite surfaces may possess additional functionalities, such as magnetism, electric conductivity, optical transparency, or even photocatalytic activity.

In the light of recent years' epidemic and environmental crises, this latter property gained increased attention from both academic and industrial researchers, as semiconductor oxide photocatalysts, such as TiO_2 or ZnO and their modified versions can eliminate harmful organic compounds and microorganisms, without relying on additional chemical treatment, due to their ability to generate reactive oxidative species (such as $HO^{\bullet}$, $HOO^{\bullet -}$ or O_2^{2-}) upon ultraviolet (UV) or visible (VIS) light illumination.

Besides the effect of photocatalyst content on wetting properties, the effectiveness and mechanism of action of photocatalytic processes is highly influenced by wetting, as well, therefore studying, and influencing the effect of interfacial parameters on the photocatalytic reactions are of high importance. Despite the modifications of photocatalyst particles and the resulting changes in reactivity are already extensively documented, the wettability alterations and their effects on the photocatalytic performance of macroscopic composite surfaces and coatings are less studied.

To fill this vacancy in the literature, the aim of my doctoral work was the preparation and characterization of novel, visible light-active plasmonic Ag-TiO_2 photocatalyst nanoparticle-containing composite coatings with different water wettability and photocatalytic efficiency. In the presented approaches spray-coating and doctor blade techniques were utilized to prepare composite surfaces with polyacrylate or

silicone matrices. The wettability and photocatalytic performance at the solid/gas (S/G) and solid/liquid (S/L) interfaces were initially adjusted by changing the roughness via photocatalyst-addition, and by changing the ratio of matrix components. Surfaces with real-time thermo- and magnetoresponsivity were prepared, as well, via the addition of thermoresponsive poly(N-isopropyl acrylamide) (pNIPAAm) polymer and carbonyl iron microparticles, respectively. To introduce another functionality, a silicone-based composite coating was enhanced with self-healing ability to provide durable superhydrophobic character.

The developed multifunctional photoreactive composites may open new routes for further developments in liquid manipulation, environmental and healthcare scenarios.

2. Literature background

2.1. Wetting phenomena

The wetting of solid surfaces is a well-developed area of interfacial science and of major importance [1-5]. Despite the solid theoretical background of this field, some wetting-related functional applications are still limited, while others are being discovered (or rediscovered) at emerging areas of interest, such as environmental protection [6,7], power saving [8] or healthcare [9,10].

As contemporary scientific literature is teeming with surfaces with wetting-related applications, such as antimicrobial- or self-cleaning coatings, it is increasingly vital to understand their behaviour and application possibilities in order to create more advanced systems and to improve the existing ones.

[1]The wettability of a macroscopic solid surface is mostly quantified by the contact angle (Θ) [2], described as the angle between the macroscopic plain of the surface and the tangential of the contour line of the liquid drop, drawn towards the three-phase (solid, liquid and gas/vapour) connection point. As **Fig. 1 a)** shows, the overall wetting characters can be categorized according to different Θ ranges. The Θ value can range from 0 to 180°, which means in the case of Θ-s, smaller than the intermediate 90°, the surface is considered well wetted (*lyophilic*, e.g., hydrophilic), while over 90°, the surface is non-well-wetted (*lyophobic*, e.g., hydrophobic). In the case of extreme spreading of the liquid (Θ<10°), the surface is *superlyophilic* (e.g., superhydrophilic), while in the case of extremely low spreading (Θ>150°), it is denoted as *superlyophobic* (e.g., superhydrophobic).

[1] The paragraph is a part of the following publication: Mérai L, Deák Á, Dékány I, Janovák L. Adv Colloid Interface Sci 2022;303:102657. (reference [11])

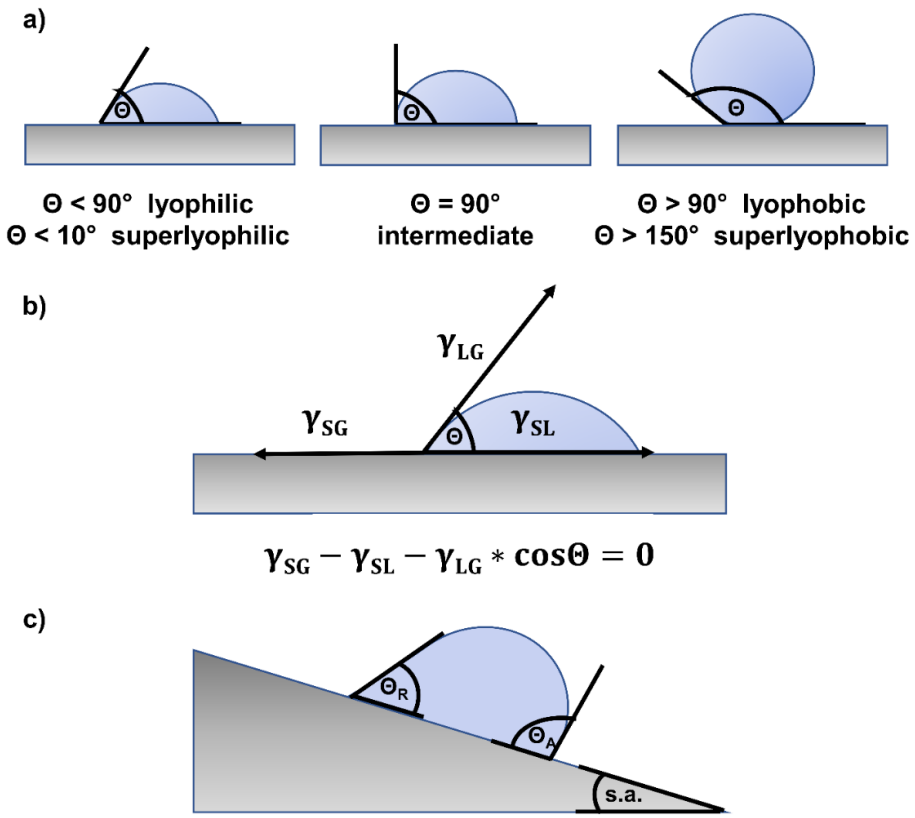

Figure 1. Wetting modes of plain surfaces, categorized according to Θ values **a)** visualization of the Young-equation **b)** and representation of the sliding angle (s.a.) and the dynamic contact angles **c)** [11]

The Θ values are dependent on the magnitude of interfacial free energies (or tensions) at the boundaries of the incident phases: this dependence is described by Young's equation (**Eq. 1**), which is visualized in **Fig. 1 b**). This simplified relation applies to perfectly plain, energetically homogenous and non-reactive solid surfaces in mechanical equilibrium:

$$\gamma_{SG} - \gamma_{SL} - \gamma_{LG} = cos\Theta \qquad \textbf{(Equation 1.)}$$

The interfacial tension between solid- and gas phases (γ_{SG}) works towards the spreading of the liquid and towards the increase of S/L-contact area, while it is counteracted by the S/L-interfacial tension (γ_{SL}). However, the L/G-interfacial tension (γ_{LG}) can contribute to both, depending on the magnitude of Θ, which is usually determined via sessile-drop method [12-14].

In a non-equilibrium state, (or under dynamic conditions) the upper- and lower limits of Θ at a particular temperature are called the advancing- (Θ_A) and receding contact angles (Θ_R), respectively (**Fig. 1 c**)). These are the so-called dynamic Θ-s and they can be observed upon the movement of liquids on solid surfaces [15-17]. Θ_A is mainly dependent on internal the cohesion of the liquid phase, while Θ_R is proportional to the adhesion between the solid and liquid phases. Their difference (Θ_A-Θ_R) is the so-called contact angle hysteresis, which is an important attribute of wettability [18]. Dynamic Θ-s can simply be measured applying the tensiometric Wilhelmy-method with a probe liquid with known surface tension [19], or by increasing or decreasing the droplet size in a conventional sessile drop setup [12].

Another useful wetting parameter is the so-called sliding angle (s.a.) [20], which is the particular tilting angle of a surface at which the droplet starts moving downwards, thanks to its own weight (**Fig. 1 c**)). The s.a. values of superlyophobic surfaces are usually referred as roll-off angles since the S/L-contact area in their case is particularly small [21]. A higher s.a. implies a more wettable surface as less contribution is required from the gravitational pull (F_g is proportional to sin tilting angle) to overcompensate the interfacial adhesion. The contact angles at the front (facing the direction of movement) and at the back of a moving droplet are equal to Θ_A and Θ_R, respectively: this creates the possibility to determine dynamic Θ-s, based on images of sliding droplets [11] (**Fig. 1 c**)).

While wettability is mainly quantified by the mentioned angles and surface tensions, their values are influenced by three main factors, which are surface texture (rough or smooth surfaces, see **Chapt. 2.2.2.** for more details) [22], surface chemistry (functional groups facing the liquid phase, see **Chapt. 2.2.1.** for more details) [23] and external stimuli (such as magnetic field, light, temperature, pH) [24]. While the wettability is directly affected by texture and chemistry, these both may be influenced by external stimuli (see **Chapt. 2.2.3.** for more details). Although, stimulus-responsivity is in fact, dependent on the composition, it can independently affect wettability, even in real-time, therefore it is increasingly considered as a distinct influencing factor. Besides wettability (and stimulus-responsivity), texture and surface chemistry may define other physical- and chemical parameters, such as antimicrobial- and photocatalytic activity (see **Chapt. 2.3.2**), as well.

The γ_{LG} values are easy-to-measure via tensiometry, however, γ_{SG} or the so-called surface free energy (γ_{SG} multiplied by 1/distance) are implicit quantitities. The existing

determination methods of γ_{SG} are based on the results of Θ- or adhesion force measurements [25]. As surface free energy in general may be affected by several possible interactions, there is no such thing as a universal approach, therefore the existing models are applicable under different conditions. For example, the Zisman method [26] is a one-component method and can only handle dispersive interactions, therefore its real-world applications are restricted to hydrophobic (low surface energy) polymer surfaces. It also provides a so-called critical surface tension (γ_c) value that is in correlation with, but not equal to the actual γ_{SG}. However, there are two-component methods, which can deal with both polar- (or non-dispersive) and dispersive interactions. The most popular ones among them are the Owens-Wendt-Rabel & Kaelble [27], or Wu methods [28]. In the case of these, highly apolar test liquids, such as diiodomethane are applied besides water, therefore contribution of polar interactions to the occuring wetting can be excluded.

Despite considering more than one type of possible chemical interactions, these models still fail when wettability is significantly influenced by roughness. To overcome this limitation, e.g., the theory of Emil Chibowsky **(Eq. 2)** can be applied, which is based on contact angle hysteresis [29], according to the following equation:

$$\gamma_s^{tot} = \gamma_{LG} \times \frac{(1+cos\Theta_{adv})^2}{(2+\cos\Theta_{rec}+cos\Theta_{adv})} \qquad \textbf{(Equation 2.)},$$

where the apparent total surface free energy of a solid (γ_s^{tot}) can be calculated knowing the Θ_{adv} and Θ_{rec} values of a test liquid with a given γ_{LG}.

2.2. Factors influencing the wetting of solid surfaces

2.2.1 Surface chemistry

As Young's equation (**Fig. 1 b), Eq. 1**) describes, the wettability is dependent on the relation of interfacial tensions, which are the overall outcomes of both chemical and physical interactions at an interface. These are mostly the results of hydrogen-bonding and van der Waals forces, which are in the order of increasing of magnitude: London-type dispersive interaction, induced dipole-dipole interaction, dipole-dipole interaction,

and charge-dipole interaction). In general, the excess of apolar surface groups leads to the dominance of the two weaker interactions, resulting in lower γ_{SG} and higher Θ, while in the case of polar surfaces the stronger hydrogen bonding, dipole-dipole or dipole-induced dipole interactions are dominant, which leads to to higher γ_{SG} and lower contact Θ [30].

The γ_{LG} of a liquid is based on the same interactions, as well [31]: for instance, the strong dipole-dipole interactions and hydrogen bonds between water molecules result in an γ_{LG} value of 72.8 mN/m (25 °C) [29], while apolar organic solvents, such as cetane (n-hexadecane) possess lower γ_{LG} (27.3 mN/m; 25 °C) [31]. Mercury is an illustrous liquid due to its extremely high γ_{LG} (485 mN/m; 25 °C), which can be attributed to the presence of metallic bonds [32]. Besides metallic bonds, electromagnetic interactions can also affect wettability in the case of of ionic liquids [33] or magnetic fluids [34].

A common way of reducing γ_{LG} and γ_{SL} and to promote wetting is the application of surfactants [35]. In this case, the decrease of γ_{SL} is achieved through surfactant adsorption [36]: as charged surfaces promote the adsorption of oppositely charged chemical species, they are popular agents of surface charge neutralization and hydrophobization [37]. However, multilayer adsorption is also possible, which turns the surface oppositely charged as it was in the beginning [38]. This weaker physisorption can also occur at charge-neutral surfaces, rendering them charged [39]. γ_{SL} can be affected by the adsorption of other surface-active molecules, such as polymers [40].

Reactive surface functional groups also influence wettability: for instance, on oxygen-deficient inorganic oxide surfaces - such as UV-irradiated TiO_2 - the dissociative chemisorption of water may occur, resulting in superhydrophilic character [41].

2.2.2 Surface texture

The applicability of Young's equation (**Fig. 1 b), Eq. 1.**) is limited by the assumption that the wetted surface is perfectly flat, which is a rare occurence in practical scenarios, in which wettability is also influenced by both the curvature (macroscopic texture) and the roughness (microscopic- or submicroscopic texture) of a surface. On the macroscopic scale, the surface inhomogenities may lead to different contact areas between solid and liquid and therefore different magnitudes of adhesion, while the presence of (sub)microscopic irregularities may increase the contribution of capillary

action to the overall wetting character [23]. The effects of roughness on wettability were initially described by two main models: in the case of the so-called Wenzel surfaces [42], the liquid completely fills the gaps on the surface, resulting in enhanced contact area and adhesion, while Cassie-Baxter surfaces [43] possess impenetrable gaps. As a third option, the so-called impregnating Cassie-state is usually mentioned: these surfaces have Θ and s.a. values similar to those of the Cassie-Baxter surfaces, however, in their case the liquid penetrates the surface texture [44]. Although, these basic concepts are useful for visualization, they become inaccurate in the case of multiscale roughness (e.g., hierarchical micro- and nanoroughness), therefore the initial concepts were enhanced over time [45], besides new modes of wetting (mainly on liophobic surfaces) were also observed [44] (**Fig. 2**).

The most well-known among these wetting states are the so-called rose petal- and lotuf effects [44]. At first sight, both plant parts are inherently hydrophobic and have hierarchical roughness, however, the microgrooves of the rose petal surface can be filled water, leading to higher contact area, adhesion, and s.a., while the microtexture of the lotus leaf is is filled with air pockets, leading to lower contact area (0.6% of the macroscopically visible contact surface), adhesion and s.a. In practice, transitions between these liophobic modes also occur [47], and transition states, such as the so-called metastable Cassie-state (partially penetrated microstructure) are also possible [48]. As **Fig. 2** shows, the main liophobic states can be categorized based which type of roughness (micro-, nano- or both) [49] (**Fig. 2**)

However, these wetting states only have practical importance in the case of water due to its relatively high γ_{LG} (72 mN/m; 25 °C) (as the droplets of a liquid with lower γ_{LG} tend to spread and fill surfacial capillaries at S/L/Air phase connections) and organic liquids at S/L/L phase connections (e.g., the behaviour of oil droplets on an underwater oleophobic surface [49,50]).

Despite the presented significant improvements of this field, the Wenzel- and Cassie-Baxter models are still the fundamental to the representation of roughness-regulated wetting alterations (**Fig. 2 and 3**). These models introduce the concept of the visually observable, apparent contact angle (Θ_{app}), which is in relation with the Young-contact angle (Θ) and the surface roughness.

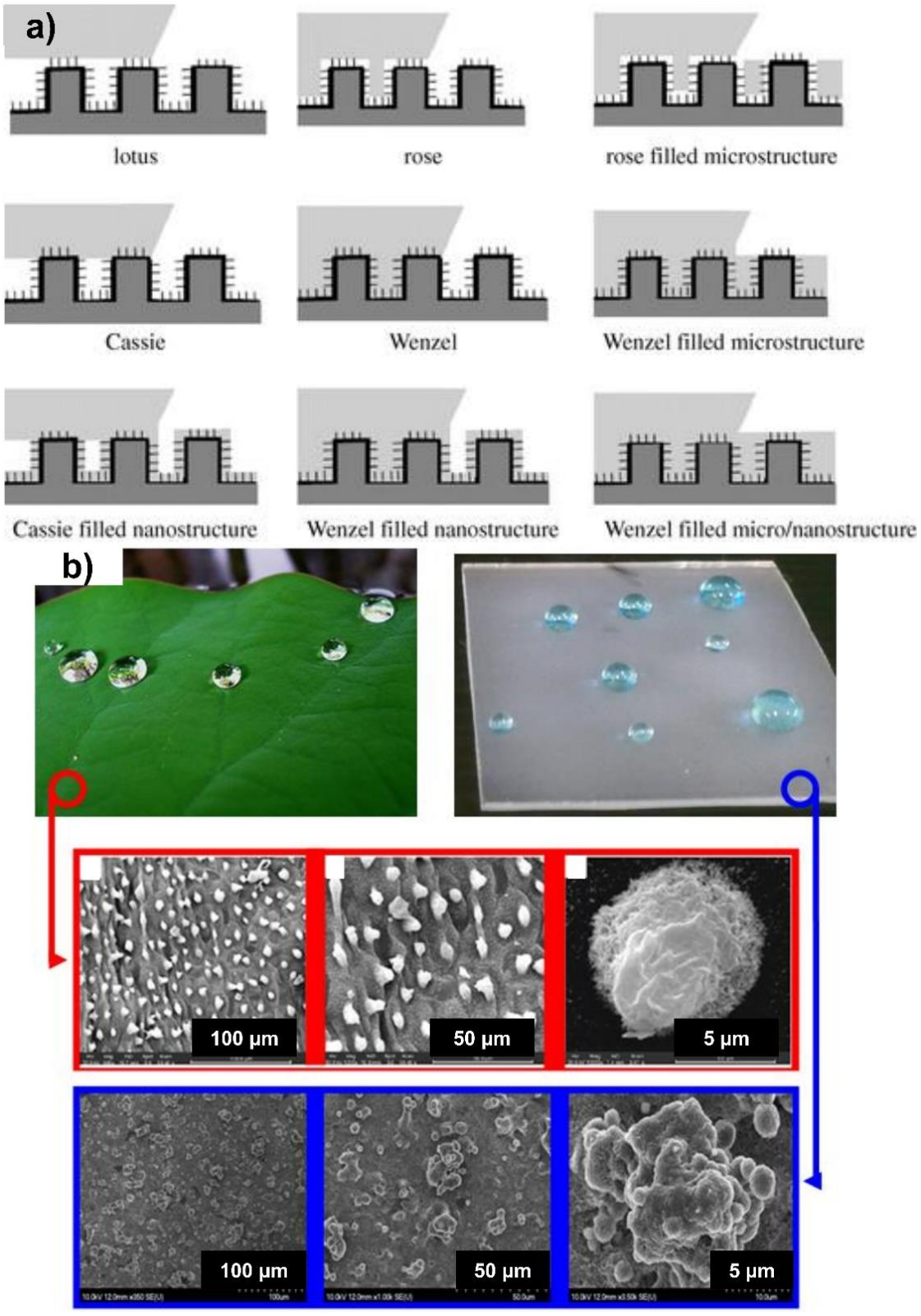

Figure 2. Scheme of the nine possible liophobic interactions on a surface with hierarchical (micro- and nano-) roughness [44] **a)** Photos and SEM images of a lotus leaf and an artificial superhydrophobic coating [46] **b)**

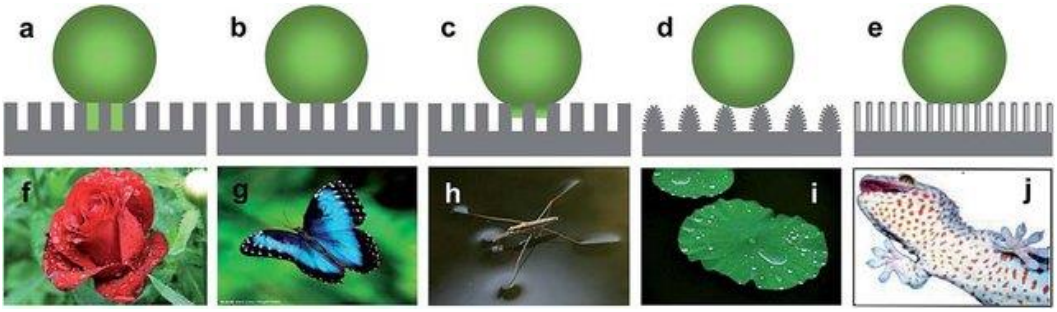

Figure 3. The five most well-known natural water-repellent surfaces: rose petal (Wenzel) **a) f)** butterfly wing (Cassie) **b) g)** strider leg (Wenzel-Cassie) **c) h)** lotus leaf **d) i)**; gecko skin **e) j)** [60]

To address the latter one, the Wenzel model (**Eq. 3**) introduces a roughness factor (r) to Young's equation, however, the Cassie-Baxter model (**Eq. 4**) also introduces the wetted fraction of surface area (f) in addition. It is also worth to mention, that in the case of complete wetting (f=1), **Eq. 4** becomes identical to **Eq. 3**.

$$\Theta_{app} = r \times \cos\Theta \qquad \textbf{(Equation 3.)}$$

$$\Theta_{app} = r \times \mathrm{f} \times \cos\Theta + f - 1 \qquad \textbf{(Equation 4.)}$$

The initial determination method of the roughness factor involved contact angle measurements on both smooth and rough surfaces of the same material, however, there are more sophisticated methods available, such as laser-scanning confocal microscopy [43] or contact profilometry [51]. The so-called Wenzel-Cassie-Baxter phase diagram [52,53] – which plots cosine values of Θ and Θ_{app} to – can also be useful in the examination of roughness-dependent wettability. As it was shown in the previous examples (**Fig. 2 and 3**), the Cassie state is superior in terms of low adhesion, liquid-repellency and low contact angle hysteresis, therefore this wetting mode - non-surprisingly - has the highest popularity among materials scientists [44].

The relation between roughness and (extreme) wettability was first evidenced upon examining natural superhydrophobic surfaces (Θ>150°) via electron microscopy [54,55]. The main reason behind plants developing natural superhydrophobicity was the self-cleaning character, which allows the contaminants to be washed away even upon the slightest contact with water (**Fig. 3. d) i)**). Since lotus leaf is very effective in this regard, the artificial surfaces usually mimic its surface structure [56,57].

Besides roughness can amplify the initial hydrophobic or hydrophilic character of a surface, it can also increase adhesion: a popular example from nature is the gecko skin, which – despite being superhydrophobic – grants exceptional climbing skills to the reptile [58,59] (**Fig. 3. e) j)**).

The aimed surface roughness can be provided applying various additive- (bottom-up) or destructive (top-down) methods. These additive methods include spray- [61] or spin-coating [62], solvent-precipitation [63], film-casting [64], chemical vapor deposition [65], physical- [66] or electrochemical deposition [67], hydrothermal- [68], or templating methods [69], in-situ polymerization [70], and even 3D-printing [71]. The destructive approaches utilize different ething methods (chemical- [72], laser- [73] or plasma [74]). While destructive methods provide better control over roughness besides exceptional reproducibility, additive methods are more economical, more scaleable and easier-to-apply. Despite rough composite materials are more popular in wetting-related applications due to their enhanced properties (see **Chapt. 2.3.1.**) [75,76], one-component systems can also be produced in both destructive [77] and additive processes, such as filtrate deposition [63], foam sintering [78] and templating [79].

Rough surfaces in general are vulnerable to mechanical damage: this can be avoided by choosing the proper, durable starting materials (e.g., metals [77] or inorganic solids [80]) or by enhancing the surfaces with self-healing character [81-84]. This property can be elaborated by infusing the matrix material with a „repairing agent", which is preferably a reactive monomer, being able to rebuild the surface upon being released due to mechanical damage [85] or by utilizing external stimuli, such as temperature [86].

As a result of damage, a rough superhydrophobic surface may start pinning liquid droplets [87], which promotes condensation and wetting and therefore leads to limited applicability in anti-wetting scenarios (anti-fouling, anti-icing, self-cleaninh, anti-corrosion). The pinning may be prevented by applying slippery liquid-infused porous surfaces (SLIPS) [87], containing a surface-covering lubricant, which is chemically inert and wets the solid with higher affinity than the test liquids besides being immiscible with it. For this purpose, the most efficient combinations are those of, hydrophobic silicone matrices ad hydrophobic silicone oils [88]. SLIPS are popular in anti-fouling- [88], anti-icing- [89,90], anti-corrosion scenarios [90] and, while they may also provide reduced drag and friction [91], self-healing character [92], lower contact angle hysteresis [93] and more uniform evaporation for the test liquids [94].

2.2.3. External stimuli

2.2.3.1. The importance of external stimuli

Although, the importance of surface chemical properties and texture in wetting-related scenarios is generally well-described, the effects of external stimuli are less studied in this regard. However, the so-called stimulus-responsive materials have been in the focus of other scientific fields in the last few decades [95,96].

Stimulus-responsive materials can reversibly alter their physical and/or chemical properties upon exposure to external stimuli, such as temperature- and pH-change, light or magnetic field, ionic strength etc. Stimulus-responsivity can be achieved in both the bulk phase and on the surface, therefore it is a popular feature of novel functional materials. The application of stimulus-responsive materials is already wide-spanning, enough to think about liquid crystal displays (LCD), intelligent windows [97,98], or pharmaceutical formulations that exploit stimulus-responsivity to achieve the controlled release of drugs in a specific target organ and/or at a specific rate [99]. Such drug formulations mostly consist of materials with pH- or thermoresponsive swelling [100], however, there are examples of magnetoresponsive formulations, as well. Latter can be achieved by the help of magnetic particles, such as maghemite (γ-Fe_2O_3) or magnetite (Fe_3O_4) [101]. Stimulus-responsivity can also improve in analytics, where the property can serve as a core mechanism in sensing physical quantities, such as pH or temperature [102]. In microfluidics, stimulus-responsivity is widely utilized to propel small volumes of liquids by mechanical response or wettability alteration [103,104].

In the case of 3D materials, the most popular properties to influence are as swelling degree, density, shape, size [105], optical features, while 2D materials can have surface properties, such as chemical functionality, charge excess and roughness [106,107] subjected of stimuli-responsiveness and these may affect wettability, as well [108-110].

2.2.3.2. Thermoresponsivity

As it is already well-known, interfacial tension is a temperature-dependent quantity, however, in practical scenarios of water, temperature only has a negligible effect on the observable Θ-s. The properties of a so-called thermoresponsive material undergo reversible alteration upon changing their temperature [111,112]. The thermoresponsive wettability also implies that the temperature-dependency of γ in magnitude is also exceeded upon these alterations.

The most popular and most-studied tool to create thermoresponsive wettability is poly(N-isopropyl acrylamide) (pNIPAAm) (**Fig. 4**): it remains miscible with water at room temperature, however, over ~32 °C, an entropy-driven precipitation (intramolecular hydrogen bonds become dominant) and phase separation occurs [113]. This lower critical solution temperature (LCST) is almost identical to the the ~37 °C temperature of the human body, which implies its applicability at the field of medicine. The LCST can also be modified by adjusting the molecular mass distibution or by copolymerization with different monomers. The versatility of pNIPAAm further improves its application possibilities, as the polymer can be immobilized on various substrates (through chemical binding or grafting), such as silicon [114], glass [101], or polymers [113] and as the most beneficial monodisperse mass-distribution (narrowest possible LCST-range) is easily achievable applying living polymerization methods, such as atomic transfer radical polymerization (ATRP) or reversible addition-fragmentation chain-transfer (RAFT) [115,116].

pNIPAAm-based materials are utilized in fields: besides the popularity of thermoresponsive drug delivery systems [117], analytical applications are also emerging [118]. In an example, a thermoresponsive surface was utilized in cell attachment-detachment scenarios: the cell adhesion was preferred over the LCST, while at lower temperatures the decoiled pNIPAAm molecules hindered the adhesion through sterical hindrance [111].

Although, the field is dominated by pNIPAAm-based materials, other thermoresponsive polymers with LCST, such as Pluronics, elastin-like polypeptides and poly(*N*-vinylcaprolactam) are are also popular in medicine [111]. To prepare materials with upper critical solution temperatures (UCST), zwitterionic polymer can be applied, however, their relevance rather low as their application is difficult to implement under physiological conditions [111,119].

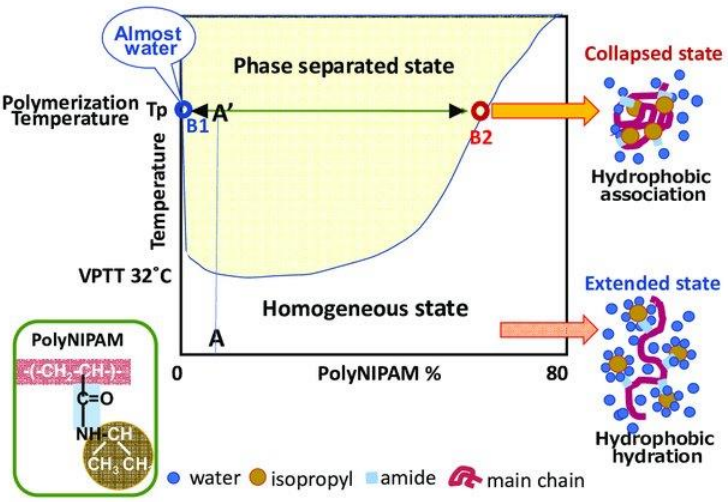

Figure 4. Structure of poly(N-isopropylacrylamide) (left), its interactions with water, displayed as a phase diagram (middle; VPTT=LCST) and as schematic images (right) [120]

Despite thermoresponsive wetting is extensively studied at the scale of colloidal- and nano systems, there fewer examples for thermoresponsive macroscopic surfaces. As these wetting transitions are affected by heat transfer, increasing the surface area may lead to difficulties in maintaining a fest-response heating-cooling cycle (insufficient heating- and/or cooling power, thermal conductivity, volume of the overall system, convection etc.), which then may lead to limited reversibility and applicability [121,122]. The other main applicability-limiting factor is the high cost of the ingrendients (NIPAAm, chemicals for living polymerization).

pNIPAAm also set foot at the field of catalysis, as well [123,124]. Thermoresponsive polymers can also be exploited in the thermal separation of a modified catalysts from a reaction mixture [125]. Despite these photocatalytic particles are extensively studied, there are less examples for macroscopic thermopresponsive photocatalytic surfaces in the literature.

In a literature example for particle modification, Jia et al. covered photoreactive Cu_2O nanoparticles in a pNIPAAm shell, which rendered the photoreactivity of the particles thermoresponsive during methyl-orange degradation tests [126]. The authors proposed that not only the wetting of the coated particles was affected, but the diffusion of the dye towards the catalyst surface also became hindered over the LCST, and as a result, reducing the reaction rates, as well.

2.2.3.3. Magnetoresponsivity

A plenty of surfaces with both magnetic and superhydrophobic characters are known, such as magnetic sponges for oil-water separation [127] and coatings for electromagnetic shielding [128], however, magnetoresponsive wettability is still less studied than any other stimulus-responsive wetting characters. While a liquid, containing dispersed magnetic particles can be manipulated by magnetic field [129], the infusion of solids with such particles offers more favourable routes as the liquid can remain intact.

The so-called magnetorheological elastomers are capable of reversibly changing their mechanical properties and shape upon exposure to external magnetic field, such as the doctor blade-casted coatings of Lee et al. [130] and Sorokin et al. [131], containing iron microparticles in poly(dimethylsiloxane) (PDMS) matrices. In these composites, the particles can align with the external magnetic force-field lines, leading to the deformation of the matrix and to pincushion-like texture with increased roughness and hydrophobicity. As this behaviour was achieved by applying uncured PDMS or high amounts of plasticizer (e.g. silicone oils), their sticky nature limits their applicability and the achievable Θ-ranges, as well. To overcome these limitations, permanently pillar-shaped magnetic structures are also preparable [132] through curing the magnetic particle-containing (e.g., magnetite, iron, etc.) in matrix prepolymers in a magnetic field: in this case, the surface structure can be tuned by changing the magnetic flux density and direction The resulting elastic, pillar-like protrusions can then also be directed by magnetic field, which thereforemay alter both the surface structure and the wetting properties, real-time.

In the work of Yang et al., the authors prepared and characterized magnetic pillars of carbonyl iron and PDMS applying magnetic field-assisted spray-coating [133]. Without magnetic field, the pillars could collapse under the impacting water droplets, increasing the S/L contact area and adhesion, however, as a magnetic field was introduced perpendicularly to the substrate surface, the stiffened pillars pinned the droplets, resulting in smaller contact area and adhesion, and therefore in an apparently increased hydrophobic character, as well (**Fig. 5**).

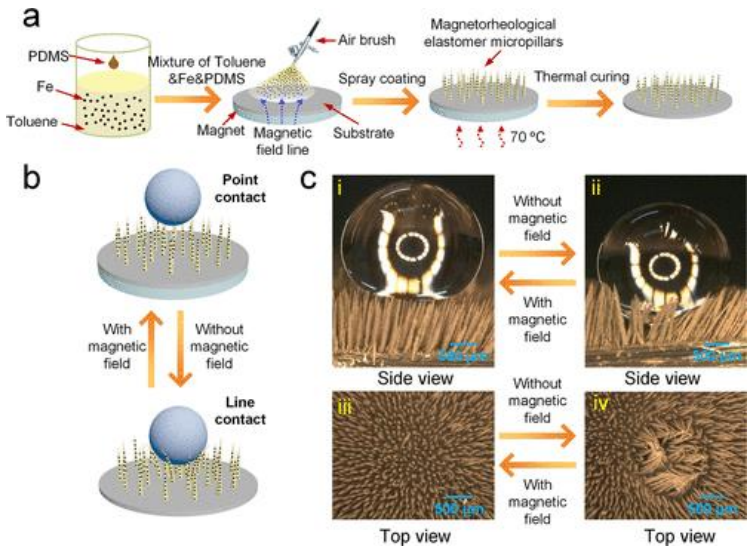

Figure 5. Preparation of a magnetoresponsive superhydrophobic composite. **a)** Reversible switching of wettability and adhesion by external magnetic field **b)** Images showing the adjustable stiffness of the micropillars under an external magnetic field, which can transform the micropillars from the collapsed, water-adhesive morphology to the stiffened water-repellent state. **c)** [133]

Due to their stimulus-responsive character, these composites may make sophisticated liquid manipulation tools, as water droplets can be picked up, transferred, and released losslessly by switching between the two wetting states. This type of composite also has the advantages of being capable of spontaneous response, while the starting materials are cheap, and the preparation methods are simple, quick, and scaleable. However, their applicability my be limited many factors, such as the improper density, height, or thickness of the pillars.

2.3. Functional composite surfaces

2.3.1. Wettability-tuning of composite surfaces

Composites are in general consist of two or more different materials, namely the matrices and the fillers: these pairings allow us the utilization of the beneficial properties of both, while in many cases, they may lead to entirely new advantages.

As the number of possible composite formation routes are virtually limitless, it is non-surprising that till this day, several composites have already been developed for and

utilized in wetting-related scenarios, such as microfluidics [129], analytical sensing [134], oil-water separation [63], antimicrobial [64], or self-cleaning purposes [62].

According to the previously presented general classification scheme, the wettability of a composite surface also mostly depends on its surface chemistry and texture, which can be tailored through the proper choice of starting materials, their ratio, or even by choosing the right preparation method [11]. As an example, applying hydrophilic or hydrophobic polymers as matrix materials can determine the initial wetting character [135], while the application of a particulate filler material increase roughness and/or porosity and therefore may lead to extreme wetting properties [136]. While applying stimulus-responsible materials in composites is gaining ground, their application in wettability alteration is still less widespread. As the previously presented examples of pNIPAAm- and magnetic particle-containing systems show, the desired stimulus-responsive character can be originated from either the matrix material (e.g., pNIPAAm-grafted polymers [117]) or the filler material (e.g., magnetic particles [133]). Taking these considerations into account, the right choice of composition may lead to extreme and even tunable wetting properties, as well.

2.3.2. Semiconductor photocatalysts and their application in composite surfaces

Besides the function of wettability alteration through roughness, filler materials can bring other functionalities to the formed composites, including improved mechanical and/or chemical resistance, different optical properties (colour, transmittance), magnetizability or electric conductivity [137]. Another interesting option is the application of photocatalyst particles as filler materials as they introduce both roughness and photoreactivity to the resulting composite surface [136].

As humanity is facing global environmental problems, the importance of greener, chemical-less solutions in environmental protection have increasing importance. In alignment with this, semiconductor photocatalysis gained increased attention recently, and materials, such as TiO_2 and ZnO and their composites became prioritized in scientific research. These semiconductors are capable of generating reactive, oxidative radicals ($^{\bullet}OH$, $O_2^{\bullet-}$ or $^{\cdot}OOH^{-\bullet}$) in aqueous media upon illumination [85,138,139], as a result of the occuring electron-hole separation. These species are then capable of decomposing organic molecules [63], even through complete oxidation (or mineralization), resulting in CO_2 and H_2O as final products. The photoreactivity at the

S/L-interface depends on several parameters, such as temperature, λ and intensity of the incident light, while the wettability of the solid surface and its adsorption affinity towards pollutants are also vital [140,141], especially in the light of the fact, that the reactive oxygen species have very short lifetime (up to a few μs half-life [142]).

The band gap energies (E_g) of the semiconductor photocatalysts usually fall within the UV-range (E_g>3 eV). As the UV-radiation gives only a small contribution (~5%) to the overall power output of the solar radiation, tuning of the E_g values to the visible region may result in higher photocatalytic efficiency in ambient sunlight, which ultimately leads to greener photocatalysis. The two most notable ways of E_g-tuning are the doping of semiconductors with other elements (e.g., N, S, I [143]), and the addition of plasmonic noble metal nanoparticles (e.g., Cu, Ag, Au [144]), which latter can increase the catalytic efficiency by the means of the inhibition of charge recombination (electron and hole) through surface plasmon resonance, as well [144] (**Fig. 6**).

Previously, our research group at the Deparment of Physical Chemistry and Materials Science of the University of Szeged prepared visible light-active plasmonic Ag nanoparticle-enhanced TiO_2 powder (Ag-TiO_2) and applied it (and its composites) in several photocatalytic experiments, such as in the elimination of different organic compounds [146], bacteria [147] or even viruses [148]. The effectivity of pohotocatalysts in such scenarios implies their capability for improving the self-cleaning nature surperphilic/-phobic surfaces, moreover, photocatalyst particles themselves can be applied as roughening agents to achieve extreme wettability.

In the light of this, our research group previously demonstrated the roughening and wettability-altering effects of ZnO-based layered double oxide (LDO) particles on fluoropolymer films. In the range of 80-90 wt.% LDO loading, the spray-coated surfaces possessed superhydrophobic character, besides LDO loading-dependent photoreactivity at the S/G-interface. [136]

As Fujishima and his co-workers discovered in 1997, the TiO_2 itself possesses UV-induced superhydrophilicity, as well, due to the formation of surficial oxygen-vacancies and the concomitant chemisorption of water **(Fig. 7)** [41].

This extreme wetting character is also utilized in self-cleaning scenarios; however, it diminishes over time without illumination as the crystalline surface returns to its original state. Popular aim of new related research is the lifetime-increasing of this superhydrophilic character besides the elaboration of this state without the need for any UV-treatment [149].

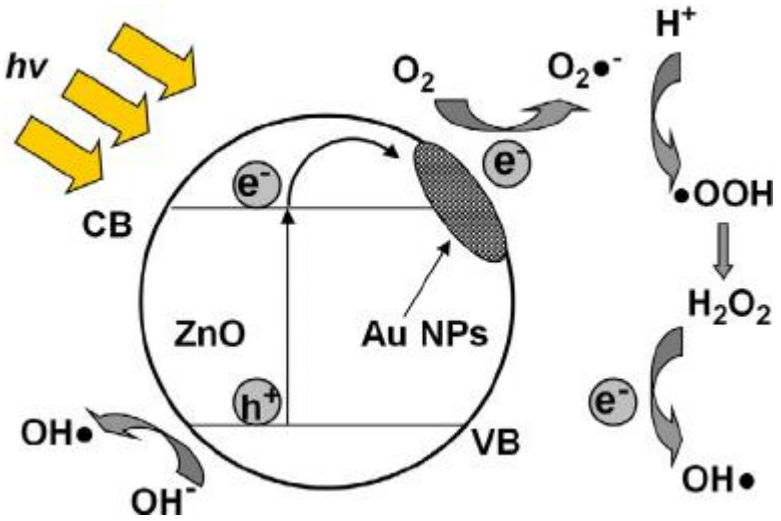

Figure 6. Reactions of semiconductor photocatalysts in auqaeous medium, and the schematic representation of the electron-trapping capability of a plasmonic additive, presented through the example of Au nanoparticle-modified ZnO particles. [145]

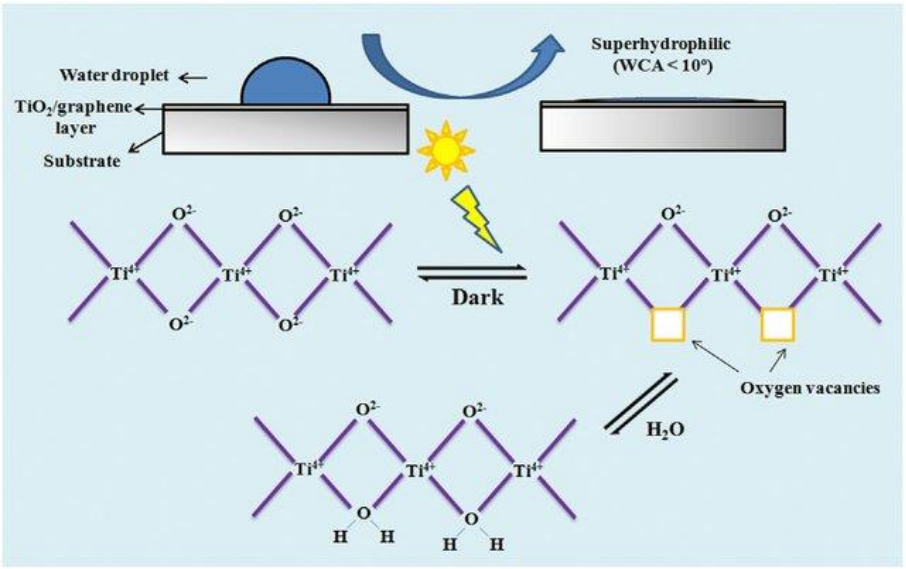

Figure 7. Representation of the wetting transitions of an UV-illuminated, TiO_2-containing surface [41]

While the contemporary scientific literature extensively covers both the topics of photoreactive composites and surfaces with extreme wettability, the simultaneous utilizations of these features are less common. Moreover, our knowledge on photoreactive surfaces with tuneable wettability are even more limited, which may pave the way towards a yet-unexploited area of materials science.

3. Motivation and aims

Despite the recent emergence of wetting- and photocatalysis-related research, our knowledge over the implementation of functional macroscopic composite surfaces and coatings with both tunable wettability and photoreactivity is still scarce. Considering the possible high potential of novel multifunctional surfaces, my doctoral work aimed the preparation and characterization of photoreactive composite surfaces with extreme and/or tunable wetting properties.

To achieve this goal, I planned to utilize:

- previously developed plasmonic Ag-TiO_2 photocatalyst nanoparticles as filler material to enhance composite surfaces with visible-light photoreactivity.
- easy-to-process and easy-to-functionalize polyacrylate and silicone matrix materials
- scalable, cheap, and simple spray-coating and doctor blade-casting coating techniques and plain glass substrate surfaces

The main focuses of the research work were the investigation of wettability, structure and photoreactivity of the model composite surfaces applying different

- photocatalyst loadings
- matrix compositions
- external stimuli, such as temperature and magnetic field using different additives and surface modification routes
- other functionalities, such as self-healing ability to provide lasting surface structure and wettability

As it was presented in the introductory chapters, the wettability of solid surfaces depends not solely on surface chemistry, but it is influenced by surface texture and external stimuli, as well. Therefore, my doctoral work focused on their effect on the wettability and photocatalytic performance of photocatalyst-containing composite coatings. In the light of this - as the schematic representation in **Fig. 8** shows - this thesis discusses the influence of composition (roughening agent and/or photocatalyst-loading, matrix composition), external stimuli (magnetic field, temperature, mechanical

damage, and moisture), besides aiming to provide an overview on the overall functionality of the presented composite surfaces.

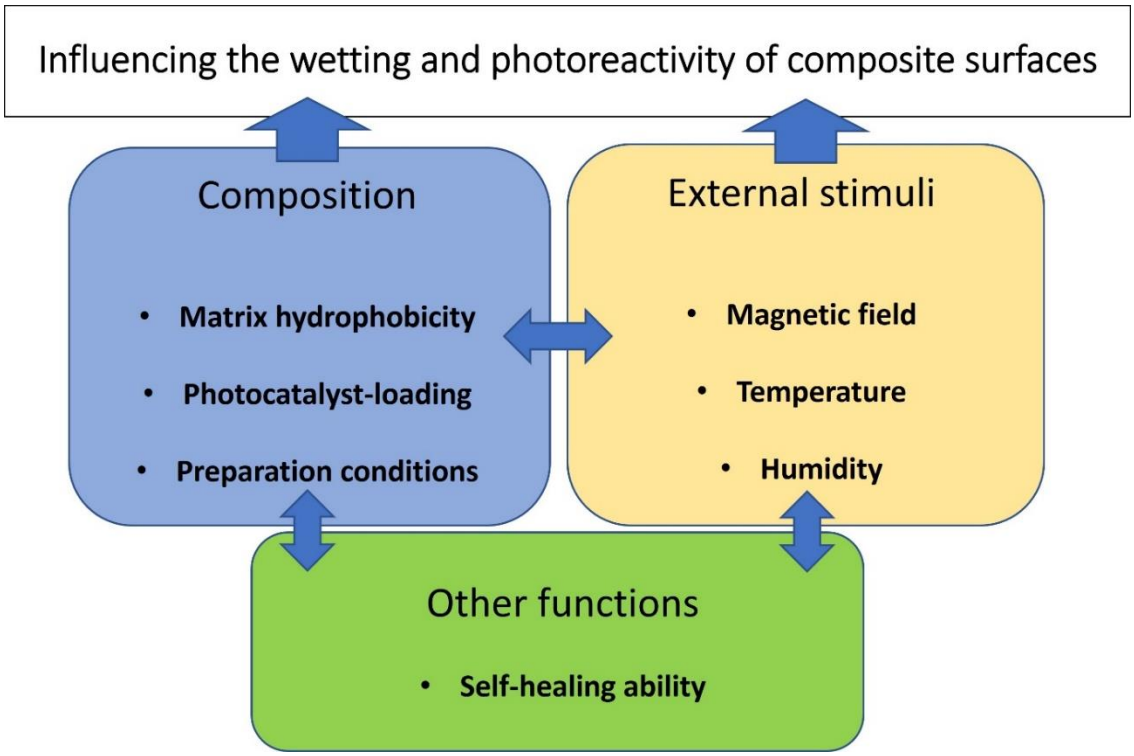

Figure 8. Schematic representation of PhD research goals

4. Experimental

4.1. Materials

Preparation and characterization of Ag-TiO_2/fluoropolymer (Ag-TiO_2/FP) composite coatings

- Ag-TiO_2 plasmonic photocatalyst nanoparticles (previously synthesized by our research group [146])
- Capstone ST-110 aqueous cationic fluoropolymer (**FP**) dispersion (solids content: 25 wt.%; pH=4-6; DuPont)
- EtOH (abs.; Molar)
- methylene-blue (**MB**; a.r.; Reanal)
- Sudan IV (a.r.; Reanal)
- N_2 (3.5; Messer)
- deionized water (**d.H_2O**)
- plain glass plates

Preparation and characterization of Ag-TiO_2/polyacrylate (Ag-TiO_2/FP+pHEA) composite coatings

- Ag-TiO_2 photocatalyst nanoparticles (previously synthesized by our research group [146])
- Capstone ST-110 aqueous cationic fluoropolymer (**FP**) dispersion (solids content: 25 wt.%; pH=4-6; DuPont)
- 2-hydroxyethyl acrylate (**HEA**; a.r.; Fluka) and its homopolymer (**pHEA**; in 5 g/l aqueous solution)
- Irgacure 651 (2,2-Dimethoxy-2-phenylacetophenone; 99%; Sigma)
- EtOH (abs.; Molar)
- methylene-blue (**MB**; a.r.; Reanal)
- Sudan IV (a.r.; Reanal)
- H_2O_2 (30%; Sigma)
- NaOH (a.r.; Molar)
- luminol (97%; Sigma)

- N_2 (3.5; Messer)
- deionized water (**d.H_2O**)
- plain glass plates

Preparation and characterization of magnetoresponsive photoreactive composites (Ag-TiO_2+cFe/PDMS)

- Ag-TiO_2 photocatalyst nanoparticles (with 0.5 wt.% Ag content, previously synthesized by our research group [146])
- carbonyl iron (**cFe**) microparticles (d=0.5-4 μm; Sigma)
- poly(dimethylsiloxane) (**PDMS**; Elastosil C1200 A and B component; Wacker)
- toluene (a.r.; Molar)
- methylene-blue (**MB**; a.r.; Reanal)
- nitrogen (3.5; Messer)
- plain glass plates (VWR microscope slides with polished edges)

Synthesis of the 10-undecenyl 2-bromoisobutyrate surface ATRP initiator (INI)

- 10-undecen-1-ol (98%; Sigma)
- triethylamine (a.r.; Fluka)
- dichloromethane (a.r.; Molar)
- Na_2SO_4 (anhydrous; puriss; Reanal)
- 2-bromoisobutyril bromide (98%; Sigma)
- cc. HCl (a.r.; Molar)
- Kieselgel-G silica gel (Reanal)
- deionized water (**d.H_2O**)

Preparation and characterization of PDMS-gr-pNIPAAm and Ag-TiO_2/PDMS-gr-pNIPAAm thermoresponsive photoreactive composites

- Ag-TiO_2 photocatalyst nanoparticles (with 0.5 wt.% Ag content, previously synthesized by our research group [146])
- poly(dimethylsiloxane) (**PDMS**; Elastosil C1200 A and B component; Wacker)
- cyclohexane (99.8%; Carlo Erba)
- MeOH (abs.; Molar)
- L-ascorbic acid (Molar Chemicals; a.r.)

- $CuBr_2$ (Sigma-Aldrich; 99%)
- *N*,*N*,*N*′,*N*″,*N*′-Pentamethyldiethylenetriamine (**PMDETA**) (Sigma-Aldrich; 99%)
- 10-undecenyl 2-bromoisobutyrate (**INI;** synthesized for this work)
- N-isopropyl acrylamide (**NIPAAm**) (Sigma-Aldrich; Schnelldorf, Germany; 97%)
- deionized water (**d.H_2O**)
- methylene-blue (**MB**; a.r.; Reanal)
- N_2 (3.5; Messer)
- plain glass plates (VWR microscope slides with polished edges)

Preparation and characterization of the self-healing Ag-TiO_2/PDMS oleogel composites

- Ag-TiO_2 photocatalyst nanoparticles (with 0.5 wt.% Ag content, previously synthesized by our research group [146])
- poly(dimethylsiloxane) (**PDMS**; Elastosil C1200 A and B component; Wacker)
- silicone oil (viscosity: 45-55 cSt; for melting and boiling point apparatus, Sigma-Sigma)
- dodecyltrichlorosilane (**$DDSiCl_3$;** 99%; Fluka)
- deionized water (**d.H_2O**)
- methylene-blue (**MB**; a.r.; Reanal)
- N_2 (3.5; Messer)
- plain glass plates
- polypropylene sample holders (laboratory vial bottle caps with polished threading; cylindrical, V=6 ml)

4.2. Preparation methods

4.2.1. Preparation of Ag-TiO_2/fluoropolymer composite coatings (Ag-TiO_2/FP)

The Ag-TiO_2 photocatalyst with 0.5 wt.% Ag nanoparticle loading was prepared during the direct functionalization of TiO_2 particles, which involved the reduction of Ag^+ ions adsorbed on the surface of TiO_2 by $NaBH_4$. The exact process was previously published [146]. The solids content of Capstone ST-110 fluoropolymer dispersion (FP) was

applied as matrix material. The Ag-TiO_2/FP photoreactive coatings with d=1.0±0.05 mg/cm^2 specific mass were elaborated on plain glass substrates, applying spray-coating technique. During preparation, 40 g/l aqueous dispersions were prepared with different Ag-TiO_2/FP ratios (0–100 wt.% Ag-TiO_2) which where then evenly sprayed on 2 cm × 2 cm and 5 cm × 5 cm glass plates from 15 cm, with the help of an R180 type Airbrush sprayer (operated with nitrogen at 3 bar).

4.2.2. Preparation of Ag-TiO_2/polyacrylate composite coatings (Ag-TiO_2/FP+pHEA)

Ag-TiO_2 [146] was kept as composite filler, while FP was kept as a hydrophobic matrix material. The additional, hydrophilic polyacrylate matrix component was synthesized by the freeradical UV polymerization of 2-hydroxyethyl acrylate (HEA) monomer in aqueous medium (50 mg/ml), applying Irgacure 651 photoinitiator (0.57 wt%). The mixture was irradiated by UV light (Q81 lamp, Heraeus Gmbh; 70 W; λ_{max}=265 nm; spectrum can be seen in **Fig. A1**) for 30 min and the resulting viscous, aqueous poly-2-hydroxyethyl acrylate (pHEA) solution (nominal polymer content: 50 mg/ml) was applied in further steps of preparation. The 5 cm ×5 cm composite coatings and the 2 cm × 2 cm plain, pure polyacrylate coatings were both prepared via spray-coating. The specific mass of the layers was set to d=5.5±0.5 mg/cm^2. During the preparation process, 40 g/l (32 g/l Ag-TiO_2 and 8 g/l polymer) aqueous dispersions were prepared with different FP/pHEA ratios (the FP content in the matrix of the resulting composites were 0, 20, 40, 60, 80, 100 wt.%, respectively) and were evenly sprayed on 4 and 25 cm^2 glass substrates from 15 cm using an R180 Airbrush sprayer (operated with nitrogen at 3 bar).

4.2.3. Preparation of magnetoresponsive grass coatings (Ag-TiO_2+cFe/PDMS)

1.5-1.5 g portions of the two PDMS components (A and B) were dissolved in 9 ml of toluene; then 4.5 g of carbonyl iron (cFe) particles (d=0.5-4 μm) were dispersed in the solution alongside 0.5, 1.0 or 1.5 g Ag-TiO_2 (6.3, 11.8 and 16.7 wt.% nominal Ag-TiO_2 loading, respectively) followed by 1 min ultrasonication. The dispersions were then sprayed (R180 Airbrush sprayer; operated with nitrogen at 3 bar) on 7.6 cm × 2.6 cm microscope slides, while a permanent magnet (surface magnetic flux density: 0.30 T or

0.35 T) was placed right behind the substrate. For contact angle measurements, the grass heights were uniformly set to 3±0.1 mm with the help of a caliper, but in the case of photocatalytic tests the specific masses were uniformized and set to 63.3±1.6 mg/cm^2. The samples were cured at room temperature for 3 h without the removal of the magnet. [150]

4.2.4. Synthesis of the 10-undecenyl 2-bromoisobutyrate surface ATRP initiator (INI)

The 10-undecenyl 2-bromoisobutyrate (initiator; INI) was synthesized according to a modified version of a previously published method [151] (**Fig. 9**). A magnetic stir bar, 5.9 ml (29.5 mmol) 10-undecen-1-ol, 5.3 ml (38 mmol) triethylamine, and 50 ml dichloromethane (predried over anhydrous Na_2SO_4) were added to a round bottom flask (100 ml) in an ice bath. 3.7 ml (29.9 mmol) 2-bromoisobutyryl bromide were added dropwise; then, the flask was removed from the ice bath and stirred at room temperature for 24 h. The solution was washed with 65 ml of 0.5 M HCl and with 65 ml d.H_2O three times; then, the organic solvent was removed with the help of a rotary evaporator. The solution was run through a column of 60 ml silica gel with 100 ml n-hexane eluent. At last, the eluent was removed with the help of a rotary evaporator to obtain the product in the form of 6.08 g (~65% yield) yellowish clear liquid. The chemical structure and the purity of the product was evidenced by ^{1}H- and ^{13}C-NMR spectroscopy [116] in deuterated benzene (C_6H_6) solvent. *NMR spectral data:* ^{1}H-NMR (500 MHz, C_6D_6), δ [ppm]: 5.77‑5.83 (m, 1H, =*CH*), 4.98‑5.07 (d, 2H, =*CH*$_2$), 3.97‑4.00 (t, 2H, ‑*CH*$_2$O), 1.97‑2.01 (m, 2H, =CH*CH*$_2$), 1.75 (s, 6H, ‑*CH*$_3$), 1.37‑1.46 (m, 2H, ‑*CH*$_2$CH$_2$O), 1.29‑1.35 (m, 2H, ‑*CH*$_2$CH$_2$CH$_2$O), 1.14‑1.23 (m, 10H, ‑*CH*$_2$*CH*$_2$*CH*$_2$*CH*$_2$*CH*$_2$‑) ^{13}C-NMR (125 MHz, C_6D_6), δ [ppm]: 171.04 (O=*C*‑O), 138.86 (*CH*=CH$_2$), 127.74 (C_6D_6), 114.23 (=*CH*$_2$), 65.65 (‑*CH*$_2$‑O), 55.83 (*C*‑Br), 33.86 (*CH*$_2$‑CH=CH$_2$), 33.85 (‑*CH*$_3$), 30.39, 29.42, 29.38, 29.10, 28.96, 28.29, 25.69 (‑*CH*$_2$*CH*$_2$*CH*$_2$*CH*$_2$*CH*$_2$*CH*$_2$*CH*$_2$*CH*$_2$‑) (the spectra can be seen in **Fig. A2**)

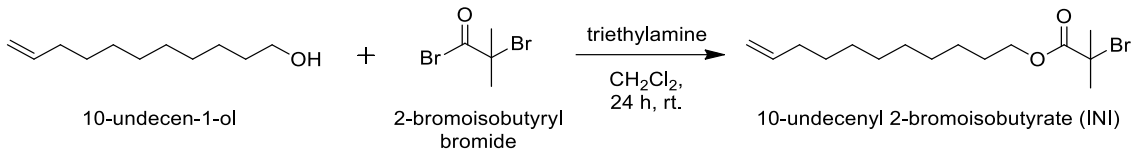

Figure 9. Synthetic scheme of the 10-undecenyl 2-bromoisobutyrate (INI) ATRP-initiator

4.2.5. Preparation of PDMS-co-INI and Ag-TiO_2/PDMS-co-INI samples

To study the elastic properties of PDMS-co-INI polymers, cylindrical bulk samples (h=0.5 cm, d=2.5 cm) were prepared with 11:0, 11:0.13, 11:0.25 or 11:0.5 PDMS-to-initiator mass-to-mass ratios (0, 1.2, 2.2 and 4.3 wt% INI, respectively). The mixtures were cured at 70 °C for 2 h in an oven, and then the samples were left at rt. for 24 h. To remove initiator residues, the cross-linked sample were immersed in 40 ml of cyclohexane for another 24 h, then was washed with 2×20 ml cyclohexane and dried at rt. for 24 h. For grafting polymerization studies, the doctor blade method (**Fig. 10**) was utilized: 2.5×2.5 cm^2 and 200 μm thick PDMS-co-INI and 15 wt% Ag-TiO_2-containing $AgTiO_2$/PDMS-co-INI layers (0, 1.2, or 4.3 wt% INI) were prepared on clean glass substrates, applying a stainless steel Zehntner ZAF 2010.8050 applicator frame. The polymer films were cured at 70 °C for 2 h in an oven, then were left for 24 h at room temperature, and then were rinsed with 2×10 ml cyclohexane and dried at room temperature. For the purpose of photocatalytic tests, 2.5 cm × 2.5 cm, d=19 mg/cm^2 spray-coated layers of Ag-TiO_2/PDMS-co-INI (1.2 wt% INI, 15 wt% Ag-TiO_2) were prepared: at first, suspensions were prepared with a total amount of 1.5 g of the raw materials (PDMS, INI, $AgTiO_2$) in 10 ml toluene. The mixtures were evenly sprayed on glass substrates from a 15 cm distance (R180 Airbrush sprayer; operated with nitrogen at 3 bar).

Figure 10. Schematic representation of the doctor blade film casting process and the photograph of the applied applicator frame

4.2.6. ARGET-ATRP synthesis of thermoresponsive PDMS-gr-PNIPAAm and Ag-TiO_2/PDMS-gr-pNIPAAm samples

To functionalize the PDMS-co-INI and Ag-TiO_2/PDMS-co-INI layers (**Chapt. 4.2.5.**) with PNIPAAm, a previously published ARGET-ATRP (Activators Regenerated by Electron Transfer – Atom Transfer Radical Polymerization) method was applied with minor modifications [115]. Glass beakers containing the coatings (on glass substrates) were charged with 0.30, 0.60, 1.25, 2.50, 5.00, 6.25, 7.50 or 10.0 M NIPAAm, 18 mg $CuBr_2$ and 20 μl PMDETA dissolved in 6 ml 1:1 (volume-to-volume ratio) water/MeOH mixture. As a reducing agent, 28 mg L-ascorbic acid was used in each case. The polymerization was initiated by adding the reducing agent to the reaction mixture. After allowing the reaction to propagate at rt. for 24 h, the samples were rinsed with 6×50 ml d.H_2O and dried at rt.

4.2.7. Preparation of the self-healing Ag-TiO_2/PDMS oleogel composites

The bulk oleogel samples were prepared in cylindrical polypropylene sample holders (h=1.2 cm, d=1.6 cm), using $DDSiCl_3$, silicone oil and PDMS prepolymers (A and B components in 1:1 ratio) in 0.10 : 0.37: 0.52 (V:V:V) ratio. The above components (with or without 25 wt.% Ag-TiO_2) were thoroughly mixed and the curing took place under dry N_2 atmosphere for 24 h at rt. to obtain oleogel samples. For the photocatalytic tests, 10 cm × 10 cm spray-coated layers (d=1±0.05 mg/cm^2) of Ag-TiO_2/PDMS oleogel were prepared and cured under N_2 atmosphere for 24 h at rt.

4.3. Methods of sample characterization

4.3.1. Scanning electron microscopy (SEM) and energy-dispersive X-ray spectroscopy (EDX)

The morphology of the composite surfaces was examined by field emission scanning electron microscopy (SEM-Hitachi S-4700 microscope), applying a secondary electron detector and 5, 10 or 20 kV acceleration voltage. The elemental analysis was performed based on energy-dispersive X-ray (EDX) spectra, recorded applying a Röntec QX2 EDS detector (Bruker).

4.3.2. Transmission electron microscopy (TEM)

To study the morphologies of the photocatalyst nanoparticles, transmission electron microscopy (TEM) measurements were conducted applying FEI Tecnai G2 20 X-TWIN and Philips CM 100 transmission electron microscopes, equipped wit tungsten cathodes, which were operated at 200 kV acceleration voltage.

4.3.3. Contact profilometry

The surface topography of the polyacrylate-containing and self-healing composites were investigated with the help of a Form Talysurf Series 2 mechanical profilometer (Taylor Hobson) with resolutions of 0.25 μm, 1 μm and 3 nm in x, y and z directions, respectively. The thickness of the Ag-TiO_2/FP composite coatings was measured applying an Elcometer 224 type digital profile gauge. Upon evaluating each of the surfaces, the root mean square deviations of displacements from the baseline (R_q) were compared.

4.3.4. X-ray computed tomography

The micro X-ray computed tomography (μCT) analysis of the films was performed with a Multiscale X-ray nanotomograph (Skyscan 2211, Bruker). In the case of Ag-TiO_2/FP composites, the examined sample volume was 1 mm^3 besides 110 kV acceleration

potential was applied and a voxel size of 0.343 mm^3 was achieved. To obtain representative images, the micro CT measurements were performed applying thickened coatings (15.1±1.3 mg/cm^2). From the resulting dataset a volume of 0.7 mm × 0.7 mm × 0.1 mm was clipped for further data analysis (porosity determination).

During the examination of Ag-TiO_2+cFe/PDMS magnetic grasses, samples with a base area of 1 cm × 1 cm were prepared and examined. The grasses were stiffened during the recordings applying a 0.45 T neodimium magnet with 1 cm × 1 cm base area, placed right below the samples. The applied acceleration potential was 110 kV in this case, as well, while the pixel resolution was 2 μm. Before the recordings, water droplets were placed on the grass applying a syringe. The height of the grass (3 mm) was confirmed with the help of μCT images and an internal scalebar of the applied software.

The reconstruction and the data analysis were carried out by NRecon, CTAn and CTVox softwares.

4.3.5. Nitrogen adsorption measurements

The specific surface area of the Ag-TiO_2 photocatalyst nanoparticles and the Ag-TiO_2+cFe/PDMS composite with 16.7 m/m% Ag-TiO_2 content was measured via nitrogen adsorption at 77 K, applying a Micromeritics gas adsorption analizer (Gemini 2375), and the Brunauer-Emmett-Teller (BET) method [152].

4.3.6. Oscillatory rheology

The elasticity of PDMS and PDMS-co-INI bulk samples was studied via oscillatory viscometry (Anton Paar Physica MCR 301) at 25 °C, applying a PP20 probe with 1-1.2 mm gap width. The storage- (G') and loss (G") moduli were determined while constantly increasing the load on the samples (0.01-1000% deformation range). The applied angular frequency was 10 s^{-1}.

4.3.7. Thermoanalytical measurements

The lower critical solution temperature (LCST) of the grafted PNIPAAm chains on PDMS-gr-pNIPAAm layers was investigated via differential scanning calorimetry (DSC) analysis. The samples were heated from 25 to 50 °C and then cooled back to 25 °C at a heating/cooling rate of 2 °C/min (Mettler-Toledo DSC822e Instrument) in sealed aluminum sample holders. In the case of each sample, the sample holder contained 2.0±0.1 mg of the corresponding layer, wetted by 20 µl d.H_2O. The applied carrier gas was dry nitrogen (flow rate: 50 ml/min). The thermogravimetry (TG) measurements were performed applying a Mettler Toledo TGA/SDTA 851e instrument: the samples with ~10 mg initial weight were heated from 25 to 500 °C (heating rate: 5 °C/min. The carrier gas was dry synthetic air (4.5) (flow rate: 50 ml/min). The obtained thermoanalytical data was processed using STARe software in both cases.

4.3.8. Magnetic flux density measurements

The magnetic flux density of the applied bar magnets was measured applying an AlphaLab Model GM2 DC Magnetometer.

4.3.9. Static contact angle and sliding angle measurements

To measure the apparent static contact angles (Θ) of the composite surfaces, the common sessile drop technique was applied, using a laboratory drop analyzer (EasyDrop, Krüss) and d.H_2O as probe liquid at 25.0±0.5 °C and 100% relative humidity (evaporating water source in the closed Peltier sample chamber) in the case of most samples. The temperature was kept constant with the help of the TC40-MK2 Peltier Temperature Assembly (Krüss) and a TC3013 Digital Thermometer (Krüss). During the measurements, 8±1 µl water droplets were placed on the samples with the help of syringe, equipped with a stainless steel needle (d=0.5 mm). The Θ values were obtained upon using the camera of the goniometer, as the drop contours in the registered images were evaluated by the DSA100 software. To determine a characteristic contact angle value of a particular surface, 5 (polyacrylate-containing and self-healing composites) or 8 (stimulus-responsive composites) parallel measurements were performed and the resulting values were averaged.

In the case of Ag-TiO_2/FP+pHEA composites, Θ values were recorded 15 minutes after the drop placement, while in other cases, freshly deposited (t=0 s) and 1 min old droplets (in the case of thermoresponsive surfaces) were analized.

In the case of Ag-TiO_2+cFe/PDMS, the magnetic field-dependence of Θ values was measured while a 0.30 T bar magnet was placed under the samples to maintain the vertical stiffening of the composite grass. To align and stiffen the strands horizontally, the magnet was turned by 90°. The s.a. were measured using a custom-made tilting cradle and the camera of the drop analyzer.

To measure the temperature-dependency of the apparent static contact angles on PDMS-gr-pNIPAAm and Ag-TiO_2/PDMS-gr-pNIPAAm layers, contact angles were measured at 25.0±0.5, 40.0±0.5, 50.0±0.5, and 60.0±0.5 °C. The Θ values were measured right after the drop placement (initial Θ) and after 1 min (quasi-equilibrium Θ)

4.3.10. Dynamic contact angle measurements

The dynamic Θ-s were determined applying the previously introduced Krüss EasyDrop instrument, and the so-called embedded-needle sessile drop measurement technique [12]. Preceding the measurements, the tip of the applied d=0.5 mm stainless steel needle was rubbed with parafilm to render it hydrophobic and less adhesive to the test liquid upon embedding. During these measurements, the size of the water droplets were firstly increased through the needle, until reaching a maximum Θ value (Θ_{adv}). The drop size was then reduced by embedding the needle and pumping up the liquid, until it reached a stable minimum value (Θ_{rec}). The obtained dynamic Θ-s were then evaluated according to the theory of Chibowsky [29] and the apparent total surface free energies (γ_s^{tot}) were calculated according to **Eq. 2**, applying the γ_{LG} value of deionized water (γ_{LG}=72.0 mN/m; 25 °C)

The dynamic contact angles and the corresponding γ^s_{tot} values were determined at both 25 and 50 °C (d.H_2O γ_{LG}=60.76 mN/m at 50 °C) in the case of the Ag-TiO_2/PDMS-co-INI and the thermoresponsive Ag-TiO_2/PDMS-gr-pNIPAAm layers.
The Θ_{adv} and (Θ_{rec}) values of the polyacrylate-based coatings were also measured applying the Wilhelmy plate method [19], using a Krüss K100 force tensiometer, 19.5 mm × 12.8 mm × 0.3 mm steel probes, spray-coated with 1.0±0.05 mg/cm^2 (Ag-TiO_2/FP) or 5.3±0.5 mg/cm^2 (Ag-TiO_2/FP+pHEA) on both sides and 6 mm/min

immersion speed at 25.0±0.5 °C. The obtained data was evaluated using LabDesk 3.2 software, according to the transposed Wilhelmy-equation (**Eq. 5**), where Θ is the calculated dynamic contact angle, F is the force, exerted to the immersed modified probe by the liquid, L is the wetted length (L= 2 × (probe thickness + probe width)) and γ_{LG} is the liguid surface tension. Upon immersing the plate the Θ_{adv}, while upon pulling out Θ_{rec} values could be measured.

The total apparent surface free energies (γ_s^{tot}) were also calculated based on these dynamic contact angle data, according to **Eq. 2** [29], applying the γ_{LG} value of deionized water (72.1 mN/m at 25 °C)

$$\Theta = \arccos(F \times L^{-1} \times \gamma_{LG}^{-1}) \qquad \textbf{(Equation 5.)}$$

4.3.11. UV-VIS diffuse reflectance spectroscopy

For the optical characterization of the polyacrylate-based composites and their components and Sudan IV photodegradation studies VIS diffuse reflectance (DR) spectra were recorded with the help of a CHEM2000 UV-VIS (Ocean Optics) spectrophotometer and an integrating sphere.

The self-assembly of the upper silicone layer on Ag-TiO_2/PDMS oleogel composites was followed by conducting VIS DR measurements, during which the sample specimens were left in a closed container with 100% relative humidity. The spectra were recorded in every 2 s for 4.6 h, then the obtained absorbance values (λ=700 nm) were compared and plotted as a function of polymerization time.

4.3.12. X-ray photoelectron spectroscopy (XPS)

The X-ray photoelectron spectra were recorded applying a SPECS instrument with a PHOIBOS 150 MCD 9 hemispherical analyzer (SPECS; FAT-mode, 40 eV pass energy for the survey and 20 eV pass energy for the high-resolution spectra). The excitation of the samples was performed using the Al Kα (h×ν=1486.6 eV) emission of the double anode at 150 W. During the spectra recordings, charge compensation (0.5 eV; 0.3 mA) was applied to set the position of the O 1s reference line to 532.00 eV binding energy

value, which is characteristic to the Si‑O‑Si environment [153]. The spectral data were processed with the help of CasaXPS and Origin softwares.

4.3.13. Nuclear magnetic resonance spectroscopy (NMR)

The NMR-spectra of the INI were recorded with the help of a Bruker DRX 500 device (Bruker; Berlin, Germany), using deuterated benzene (C_6D_6) as solvent and the characteristic C_6D_6 signal as the internal standard. The ^{1}H-decoupled ^{13}C-NMR spectra were recorded at 125 MHz applying J-MOD pulse-sequence. The data was processed using MestReC software.

4.3.14. Raman microscopy

The Raman-spectra and the Raman-intensity heatmaps were obtained appliying a Thermo Fisher Scientific DXR Raman microscope. A laser-light of 780 nm wavelength was applied as excitation light source, with 24 mW applied maximum power. During measurements, 50× magnification and an aperture of 25 μm was used. The size of the mapped surface area (200‑3300 cm^{-1} Raman-shift range) was 30 μm × 30 μm, while the vertical and horizontal step size was 1 μm. Both the instrument operation and the evaluation of the results were carried out utilizing the software OMNIC for Dispersive Raman 8.2.

4.3.15. Determination of EtOH (g) photodegradation efficiency of Ag-TiO_2/FP, Ag-TiO_2/FP+pHEA and Ag-TiO_2/PDMS-oleogel via gas chromatography

The photoreactivity of the layers at the S/G-interface was studied during ethanol (as model volatile organic compound or VOC) photodegradation tests, applying a LED light source (GE Hungary, λ_{max}=405 nm; **Fig. A3**). The concentration of EtOH (g) was followed via gas chromatography (Shimadzu GC-14B). During the experiments, 5 μl EtOH was injected into the reaction chamber (25.0±0.5 °C), containing 5 cm × 5 cm coatings, fixed at 5 cm from the LED lamp. At this distance, the measured intensity of the radiation was 24.3 mW/cm^2 (measured applying a Thorlabs PM100 instrument). The c/c_0 values were plotted as a function of illumination time, where c is the concentration

of EtOH (g) at a given time (t) and c_0 is the initial concentration (c_0=0.36 mM). The apparent first-order reaction rate constants (k′, given in min^{-1}) were determined, according to the following equation (**Eq. 6**):

$$\ln\left(\frac{c}{c_0}\right) = -k' \times t \qquad \textbf{(Equation 6.)}$$

4.3.16. Determination of Sudan IV photodegradation efficiency via UV-VIS diffuse reflectance spectroscopy

The photoreactivity of the 80 wt.% Ag-TiO_2-containing Ag-TiO_2/FP films (r-FP) were verified during Sudan IV photodegradation expereiments, applying a LED light source (GE Hungary, λ_{max}=405 nm; **Fig. A3**): 50 µl droplets of 0.020 g/l (52.6 µM) Sudan IV solution (solvent: n-hexane) were placed on the surface, that was then illuminated from 5 cm for 90 min, at 25.0±0.5 °C). The dye stain degradation efficiency was determined with the help of the recorded diffuse-reflectance spectra (see **Chapt. 4.3.11.**) and the previously determined calibration curve, based on the nominal specific mass of the dye stains (mg/cm^2) and the recorded absorbance values at λ=520.97 nm (**Fig. A4**). Each of the measurements were repeated two times.

4.3.17. Determination S/L-photoreactivity via UV-VIS spectrophotometry

The photocatalytic activity of the composite coatings was also studied at the S/L interface. Hydrophilic methylene-blue (MB) in d.H_2O and hydrophobic Sudan IV dye in organic medium (abs. EtOH) were chosen as model pollutants to evaluate the photocatalytic activity of the composite surfaces. The dye concentration was determined via spectrophotometry, applying a Red Tide SHIMADZU UV-1800 instrument. The experiments were conducted directly in a quartz cuvette, containing the r-pHEA- or r-FP-coated glass plate (3 cm × 0.9 cm), immersed in the 3 ml solution ofthe model pollutant. After a 30 min adsorption time in dark, the absorbance spectra were recorded after 0, 10, 20, 30, 40, 50, 60, 75 and 90 min of blue led LED-light illumination (GE Hungary, λ_{max}=405 nm; **Fig. A3**). The initial concentration of the dyes were 0.025 g/l (65 µM) and 0.002 g/l (6.25 µM) in the case of Sudan IV and MB, respectively.

4.3.18. Determination of photoreactivity of Ag-TiO_2+cFe/PDMS at the S/L-interface via UV-VIS spectrophotometry

The photoreactivity of the magnetoresponsive grass composites was studied at the S/L-interface. The coated glass plates were placed in plastic Petri dishes with the diameter of 9.0 cm; which were then carefully filled with 50 ml of 0.002 g/l (6.25 μM) aqueous MB solution, and were kept in dark for 30 min to achieve adsorption equilibrium. The plates were then illuminated for 300 min, applying a blue light LED (GE Hungary, λ_{max}=405 nm; **Fig. A3**) [20] from 5 cm distance. During illumination, the MB solution was agitated at 50 rpm. The concentration of MB was determined by regularly sampling 3.2 ml portions of the MB solution with the help of an automated pipette and recording their absorbance spectra, applying a Red Tide SHIMADZU UV-1800 instrument. The MB concentration was determined according to the previously recorded calibration curve and the obtained absorbance values at λ=660 nm). After recording each spectra (~1 min), the samples were transferred back into the experimental solution. The experiment was repeated with vertically tiffened grass, as well (0.30 T external magnetic field, bar magnet placed below the Petri dish. The MB degradation was also conducted without photocatalythic surface (MB photolysis) and with pure Ag-TiO_2 in the same nominal amount (0.208 g) as it was incorporated in the examined composites. All experiments were performed 3 times

4.3.19. Determination of photoreactivity of Ag-TiO_2/PDMS-gr-pNIPAAm at the S/L-interface via UV-VIS spectrophotometry

Methylene-blue (MB; c_0=2 mg/l or 6.25 μM) photodegradation test were run at the S/L-interface. 2.5×2.5 cm^2, 19 mg/cm^2 specific mass spray-coated layers of Ag-TiO_2/PDMS-gr-pNIPAAm (1.2 wt% INI; 5 M NIPAAm) were placed in a V=85 ml custom-made stainless steel reactor, equipped with a heating mantle and a quartz window at the top. The MB solution in the reactor was kept in continous flow, using a peristaltic pump with tubing of 15 ml overall volume; therefore 100 ml MB solution was used in each of the experiments. Prior to the photocatalytic tests, the thermostated reactor (25, or 50 °C), containing the composite layer (fixed on a clean microscope slide by 1×1 cm^2 double-sided adhesive tape) and the 100 ml MB solution was kept in dark for 40 min to ensure the adsorption equilibrium of the test molecule. The Ag-

TiO_2/PDMS-gr-pNIPAAm samples were illuminated by a blue-light LED lamp (λ_{max}=405 nm, General Electrics Hungary; **Fig. A3**) for 300 min, placed at a distance of 5 cm from the layers. 3 ml portions of MB solution were regularly sampled from the reactor with the help of a syringe, and the concentration decrease was monitored via spectrophotometry (Red Tide SHIMADZU UV-1800 instrument), applying a previously recorded calibration curve for absorbance values at λ=660 nm. The sampled portions of the MB solution were injected back into the reactor after the ~2 minutes-long spectra recordings. This sampling process resulted in less than 1% overall liquid volume decrease in the reactor after 5 hours of irradiation. Each photocatalytic experiment was conducted 3 times.

4.3.20. Luminometry measurements

The reactive oxigene-containing radicals, formed at the S/L-interface, during the illumination of Ag-TiO_2/FP+pHEA coatings were quantified applying a Sirius L Single Tube luminometer (Berthold Detection Systems, Germany): the layers were placed in 40 ml, continously agitated (50 rpm) d.H_2O, while being illuminated by an UV-lamp (15 W low pressure Hg gas lamp, λ_{max}=365 nm, LightTech) (**Fig. A3**), placed 5 cm above the samples. 100 µl samples were taken regularly and were added to the cuvette of the instrument, already containing 100 µl luminol solution (c=1.69 µM; also containing 5 mM NaOH). The H_2O_2-equivalent radical concentrations were determined on the basis of the measured chemoluminescent intensities, obtained in RLU/s (Relative Light Unit) and the previously recorded calibration curve (applying 0-5 mM H_2O_2 solutions) (**Eq. 7; Fig. A5**)

$$c_{H2O2} = \frac{RLU/s\ value\ after\ 30\ s}{41866}\ mM \quad \textbf{Equation 7.}$$

The reaction between the luminol and the reactive radicals is schematicly depicted in **Fig. 11**.

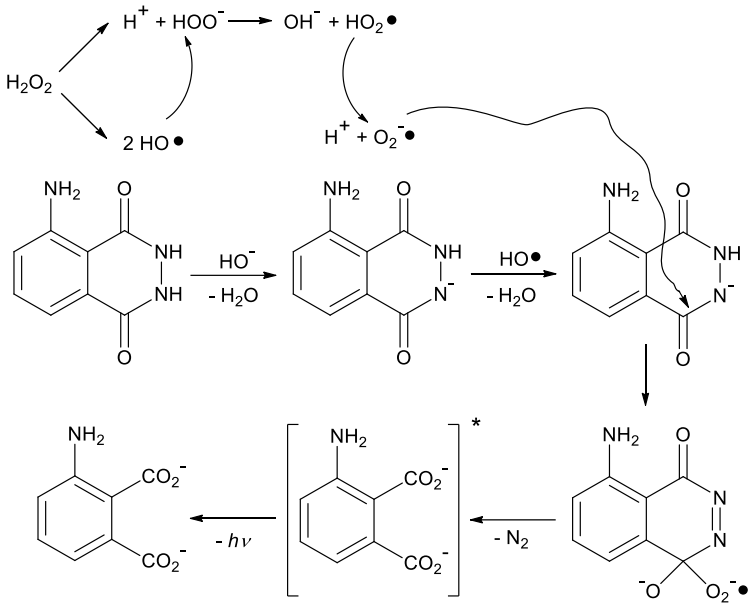

Figure 11. Proposed mechanism of the reaction of luminol and reactive oxigen-containing radicals [154]

5. Results and discussion

5.1. Characterization of the filler and matrix materials

5.1.1. Ag-TiO_2 plasmonic photocatalyst

While the composition of photoreactive composites can vary on a broad scale, regarding both the photocatalytic fillers and matrix materials, the main selection criteria for this research were the availability, processibility and applicability, latter with a big emphasis on the photocatalytic efficiency and sustainability.

Previously, our research group gained expertise in the preparation and characterization of plasmonic nanometal-modified visible light-photoreactive TiO_2 catalysts, such as Ag-TiO_2 and Cu-TiO_2, which were proven to be effective in the neutralization of different VOCs and microorganisms (*Staphylococcus aureus*, *Escherichia coli*, *Pseudomonas aeruginosa* [147]). As it is visible in the DR spectra of **Fig. 12 a)**, the TiO_2 (anatase) has an E_g value of 3.22 eV, which falls into the UV-range, while the Ag-TiO_2 has an E_g value of 3.08 eV, indicating excitability by visible-light. As the TEM image of **Fig. 12 b)** shows, the catalyst itself consist of P25 TiO_2 nanoparticles (d_{mean}=50 nm), decorated with d_{mean}=5 nm Ag nanoparticles (**Fig. 12 b)**), formed during the chemical reduction of Ag^+ ions by $NaBH_4$ [145].

As our research group published earlier, the silver nanoparticles on the TiO_2 photocatalyst resulted in a plasmonic absorbance peak in the visible light region with a λ maximum of 450 nm [46,155]. Thanks to this, the obtained band gap value (E_g) of Ag-TiO_2 was lower (3.08 eV) than that of the original P25 TiO_2 (3.22 eV), therefore it showed increased photocatalytic activity under blue (λ_{max}=405 nm) LED irradiation. In the case of this noble metal-semiconductor composite photocatalyst, visible light is harvested via surface plasmon resonance, attributed to the Ag nanoparticles, while the metal-semiconductor interface takes part in charge separation (generation of holes and electrons). The nominal surface Ag-concentration was set to 0.5 wt.%, because as it was previously evidenced, the highest photocatalytic efficiency is achievable at 0.5 wt.% Ag content in the examined composition range (0-1wt.% Ag) [156].

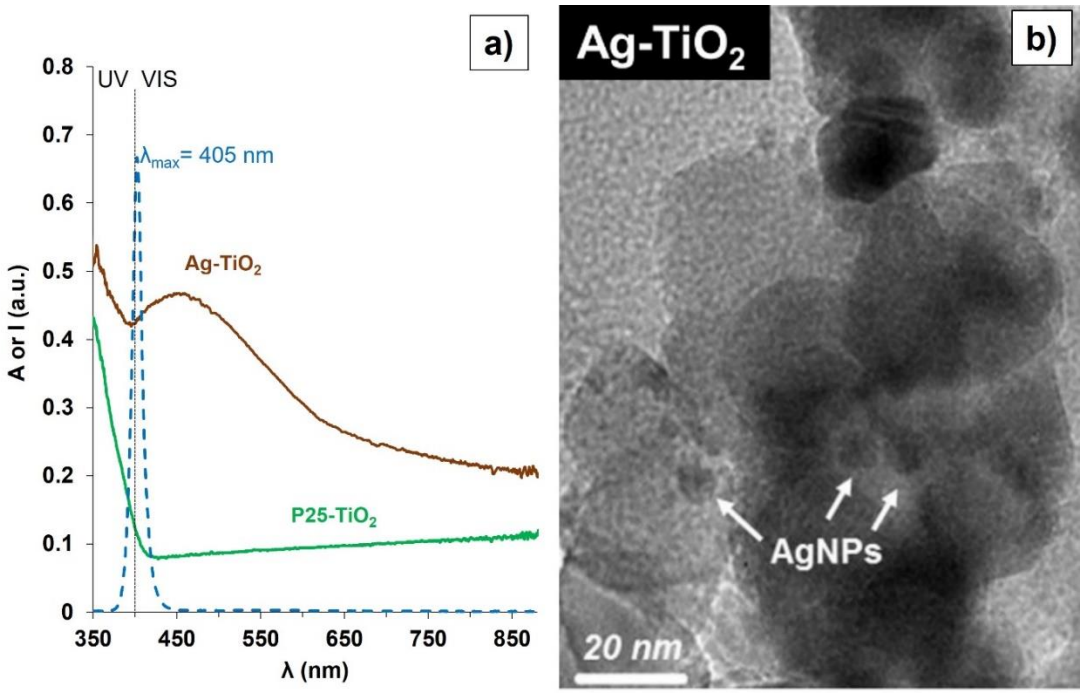

Figure 12. UV-VIS DR spectra of the commercial P25 TiO_2, the Ag-TiO_2 and the emission spectrum of the applied blue LED lightsource **a)** TEM-image of Ag-TiO_2 nanoparticles **b)** [146,155]

The detailed XPS analysis of Ag-TiO_2 was also presented in previous works, based on the evaluation of Ti 2p, O 1s and Ag 3d regions of the original and Ag-enhanced TiO_2 [155]. The spectrum of Ag-TiO_2 indicated the presence of silver oxides as the $3d_{5/2}$ component was positioned at 367.8 eV [156], which is in good accordance with the fact, that metallic Ag is prone to oxidation on the surface of TiO_2 (forming Ag_2O) [157]. It is also worth to note that the determined (XPS) surface Ag content (0.119 at%) was in good accordance with the nominal Ag content (0.125 at%), as 95.5% of the initial Ag amount was detected [155]. Similar results were obtained by Chaudhary and co-workers also came to a similar conclusion upon studying their own Ag-functionalized TiO_2 photocatalyst [158].

The immobilization of Ag-TiO_2 in transparent polymer films did not result in significant changes in E_g values (3.06-3.08 eV), which is beneficial regarding its application in photocatalytic composite coatings. As the photocatalyst itself was already well-studied and available in higher quantities, it was chosen as composite filler material.

5.1.2. Capstone ST 110 perfluorinated polyacrylate (FP)

The applied matrix materials were chosen based on their wettability, processibility and compatibility with the filler particles: as a hydrophobic matrix component, the solids content of a commercially available aqueous fluoropolymer dispersion (Capstone ST-110, denoted as FP) was selected. The Capstone ST-110 has good film-forming ability and contains fluoropolymer latex particles (**Fig. 13**), consisting of fluorinated alkyl-metacrylate and dialkyl-ammonium metacrylate acetate salt monomers. Thanks to the latter one, the latex particles may possess positive surface charge and good dispersibility in acidic aqueous medium (dispersion pH: 4-6, provided by aliphatic organic acids), which is benefficial in terms greener spray-coating applications. Despite the net positive surface charge, the spray-coated smooth layers of the polymer possess hydrophobic character (Θ=105°).

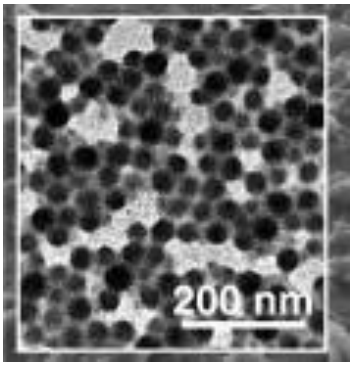

Figure 13. TEM image of Capstone ST-110 latex particles [159]

5.1.3. Poly(2-hydroxyethyl acrylate) (pHEA)

As a hydrophilic matrix component, poly(2-hydroxyethyl acrylate) (pHEA) was selected [160]: the polymer was synthesized according to the scheme in **Fig. 14**, applying a UV-photoinitiated radical polymerization method (**Chapter 4.2.2.**) in aqueous medium. Then, the resulting polymer solution could be mixed with the FP dispersion to produce various polymer- and composite coatings. The spray-coated smooth layers of the pure pHEA possess hydrophilic character with Θ=27.4°. According to the recorded UV-VIS DR spectra (**Fig. 15**), neither the pHEA, nor the FP showed significant optical absorbance in the visible region, which is preferable for photocatalytic applications.

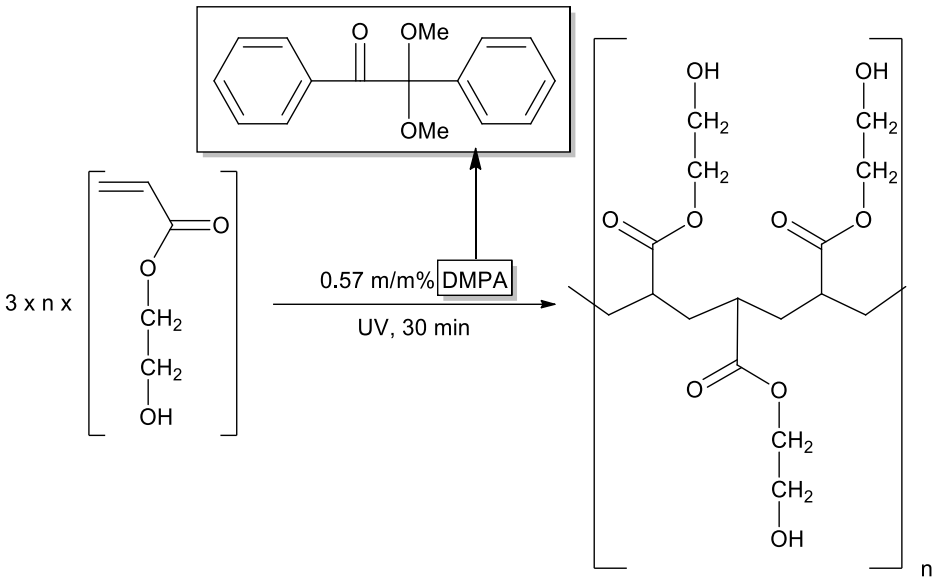

Figure 14. Scheme of pHEA synthesis

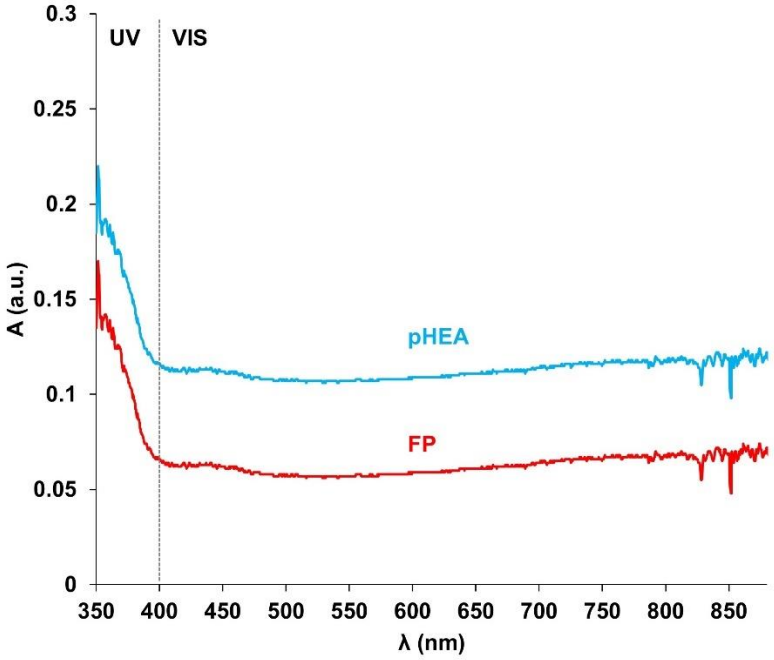

Figure 15. UV-VIS DR spectra of smooth pHEA and FP polymer films.

5.1.4. Poly(dimethylsiloxane) (PDMS)

For the preparation of stimulus-responsive composites, poly(dimethyl siloxane) (PDMS) was applied as a matrix material due to its hydrophobicity, elasticity, chemical stability and processibility. Thanks to these properties, PDMS is a popular ingrendient of stimulus responsive systems and microfluidic devices [161]. Moreover, it can be

infused with organic liquids, such as silicone oils to form oleogels, which then can be applied to prepare advanced self-healing surfaces, as well [82,88].

In this work, the commercially available Elastosil C1200 (Wacker) two-component PDMS elastomer was utilized: as it can be seen in **Fig. 16**, the A-component (crosslinker) contains silicone hydride prepolyer and vinyl-terminated silicone oligomers, while the B-component (catalyst) also contains silicone hydride, blue dye and the Pt-complex catalyst, which promotes crosslinking.

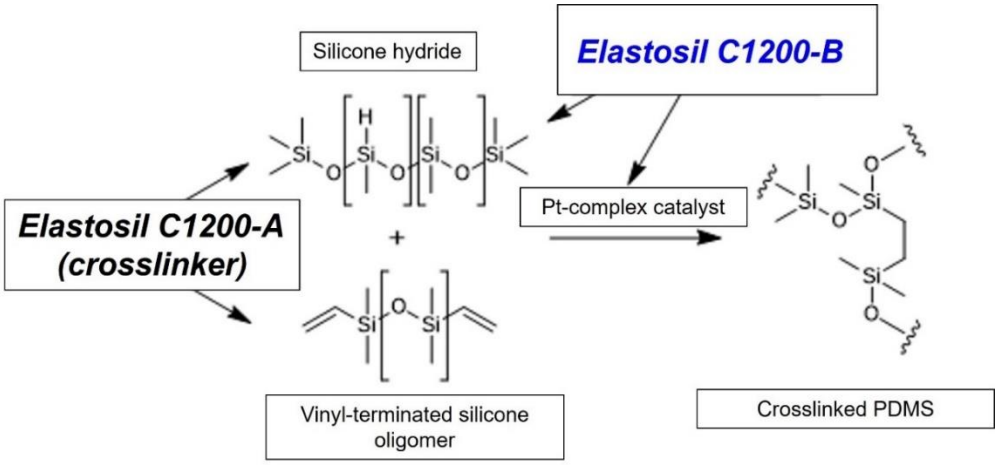

Figure 16. Components of Elastosil C1200 PDMS elastomer and the scheme of their crosslinking

After mixing components A and B, the curing takes place according to **Fig. 16** [26]. The elastic (storage moduli; G') and viscous (loss moduli; G") properties of the obtained bulk samples with different crosslinker content were determined via oscillatory viscometry (**Chapt. 4.3.6.**): as it is displayed in **Fig. 17 a)**, different crosslinker content leads to different characteristic modulus vs. deformation curves. The maximum elasticity is reached at 1 : 1 (mass-to-mass) ratio (**Fig. 17 b))**, while increasing either the concentration of either one of the components, the moduli drastically decrease, indicating a more liquid-like, viscous character.

To prepare stimuli-responsive surfaces with reversible enough shape and wetting transitions, high elasticity is vital: as the 1 : 1 proportion (also recommended by the manufacturer) provides the highest G' value and superior elasticity, this composition was applied in the further experiments.

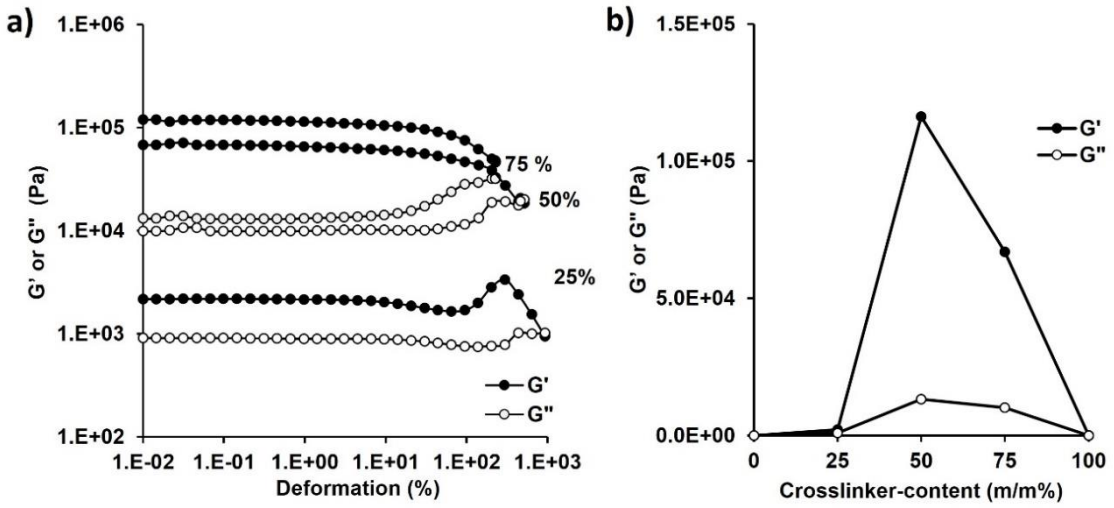

Figure 17. The measured storage (G') and loss moduli (G") of the PDMS matrix as a function of the applied deformation **a)** The effect of cross- linker (component A) content G' and G" valuess **b)** [150]

5.1.4. Other starting materials and the applied composite preparation techniques

The magnetoresponsive surfaces were elaborated using spherical carbonyl iron (cFe) microparticles (d=0.5-4 μm), as magnetic filler, due to their previously reported high compatibility to PDMS matrices [133]. The cFe also has the advantage of ferromagnetism over the popular ferrimagnetic iron oxides (maghemite and magnetite).

The thermoresponsive character was elaborated upon grafting PDMS with poly(N-isopropyl acrylamide) (pNIPAAm), which - as it has already been presented in **Chapt. 2.2.3.2.** - is the most studied thermoresponsive polymer.

As a substrate surface for the prepared coatings, plain glass was selected as it generally provides high adhesion, it is cheap and can be easily cut into the desired shape and size applying simple hand tools (e.g. diamond glass cutter knife).

The coatings were mainly applied on the glass using spray-coating or doctor blade techniques. Spray-coating is a fast, cheap and scaleable method, which is essential in producing large numbers of composite coatings with the same specific mass: achieving this is preferred for the sake of a comparison of photoreactivity, as objective as possible (polyacrylate-containing coatings). The preparation of magnetoresponsive composites was also based on spray-coating: the magnetoresponsive surface structure formed as a result of introducing a permanent magnet to the glass substrate, leading to the magnetic

force field-directed deposition of the components [133]. The also fast and cheap doctor blade method was applied during the preparation of PDMS-based surfaces, as the aim was the elaboration of a more uniform layer thickness and a smooth surface (self-healing coatings, pNIPAAm-grafted surfaces)

5.2. Regulation of wetting and photoreactivity by photocatalyst loading - characterization of Ag-TiO_2/FP composite coatings

5.2.1. Wetting properties of Ag-TiO_2/FP composite coatings

As it has already been shown earlier (**Fig. 2 and 3**), when it comes to wettability, surface morphology has an importance, equal to that of the chemical composition. Therefore, upon designing photoreactive composite surfaces with desired wettability, the surface-roughening effect of the applied photocatalyst filler should also be taken into account.

To study the effects of photocatalyst-loading on photoreactive composite coatings, at first, the Ag-TiO_2 filler was dispersed in FP matrix in different quantities via spray-coating.

As **Fig. 18 a)** shows, the measured Θ values vary with the photocatalyst-loading. The pure and smooth FP coating possess a relatively high Θ value (105.0°), indicating a hydrophobic, Teflon-like wetting character. However, the measured Θ values increased with increasing Ag-TiO_2 content (from left to right) till 80 wt.%, indicating decreased wettability, which is in good accordance with the Wenzel [42,43,47,53] and Cassie-Baxter [43,47,53] models. However, as the Ag-TiO_2 content was increased further to 100 wt.%, the photocatalyst film without polymer coating showed superhydrophilic character (Θ= ~0°), which is in good accordance with the generally good water-wettability of TiO_2 particles [162]. The hydrobhobicity peaked at around 40-80 wt.% photocatalyst content, while even reaching superhydrophobic character (Θ values of ~150.0°) [136].

Besides static Θ measurements, the total apparent surface free energies (γ_s^{tot}) of the coatings with different compositions were also determined, based on the measured Θ_{adv} and Θ_{rec} values (according to **Eq. 2** [29]), obtained during Wilhelmy plate

measurements [19]. The smaller plot of **Fig. 18. a)** displayes the measured Θ_{adv} and Θ_{rec} values, belonging to the flat FP sample, besides the γ_s^{tot} values are shown in **Fig. 18 b)** as a function of Ag-TiO_2 loading. The measured values were in accordance with the results of static Θ measurements. Without Ag-TiO_2 and considerable roughness, the smooth FP coating has relatively low γ_s^{tot} (27.3 mJ/m^2), which indicates a Teflon-like character [163]. However, the FP-free pure Ag-TiO_2 coating possesses a significantly higher γ_s^{tot} value (71.9 mJ/m^2), which is also indicative of the superhydrophilic character of the semiconductor material [164]. Therefore, it has been proven that the wetting character of coatings, made solely of Ag-TiO_2 and FP can be tuned from superhydrophopic to superhydrophilic, only by changing the filler : matrix- ratio.

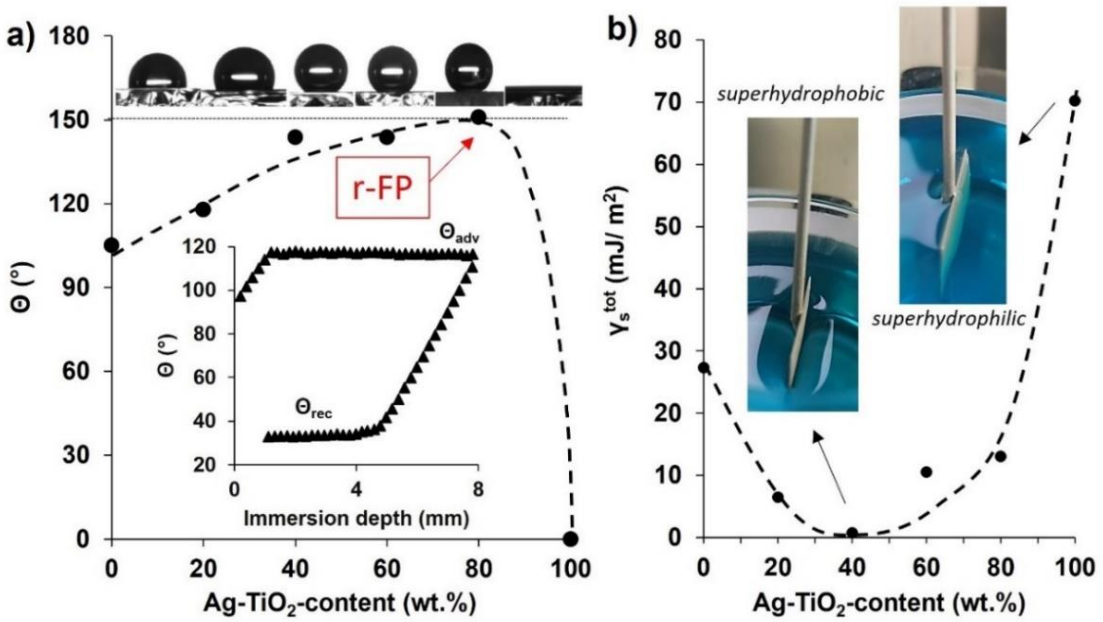

Figure 18. Measured Θ **a)** and calculated γ_s^{tot} **b)** of Ag-TiO_2/FP composite coatings as a function of photocatalyst loading (The dashed lines are for visualization only, as no mathematically accurate correlation was made). The inserted diagraph in **a)** shows the Θ_{adv} and Θ_{rec} values of the pure FP coating, determined during Wilhelmy-plate measurements [85]

5.2.2. Morphology of Ag-TiO_2/FP composite coatings

The experienced wetting behaviour of FP-based coatings can be associated with the surface texture, provided by the roughening effect of the photocatalyst. The captured SEM images of **Fig. 19** indicate increasing surface roughness with increasing photocatalyst content: **Fig. 19 a)** shows the relatively smooth surface of the pure FP layer, however, the composite films are decorated with quasi-spherical microscale aggregates (d=5-40 μm) of the primer Ag-TiO_2 nanoparticles (**Fig. 19 b)-d)**).

The profilometrically obtained R_q values are also shown in **Fig. 19**. The R_q of pure FP was determined to be 3.7±0.9 μm, however, the rough composites with 20, 40 and 80 wt.% Ag-TiO_2 showed increasing R_q values (5.2±1.5, 7.8±1.9 and 15.2±1.2 μm, respectively).

At higher magnifications, nanoroughness could also identified, indicating that the 5-40 μm spheroidal microstructures themselves formed because of primary Ag-TiO_2 particle-aggregation (d_{mean}=50 nm) during the coating process. This phenomenon led to considerable surface roughness both in micro- and nanoscale (**Fig. 20**).

The picture of **Fig. 19 e)-h)** shows the SEM image (**e**), and the EDX elemental distribution of carbon (**f**), titanium (**g**) and carbon/titanium (**h**) on the superhydrophobic surface with 80 wt.% Ag-TiO_2 content (this layer composition will be denoted as r-FP from now on). As it can be seen, at this relatively high photocatalyst loading both the C of the polymer (green) and the Ti of the photocatalyst (red) were observable by EDX, which indicates an only partial coverage of the photocatalyst particles by the FP matrix. As it will be presented in the followings, this dual presence and relatively homogenous distribution of the catalyst and the FP resulted in surfaces with simultaneous photoreactive and superhydrophobic characters.

Besides surface roughness, porosity is also crucial both in terms of wettabilityalteration and in terms of photoreactivity. As it was also evidenced by micro-CT images (**Fig. 21)**, the spray-coated superhydrophobic r-FP composite film consists of adhered microspheres, however, the nanoroughness was only observable via SEM.

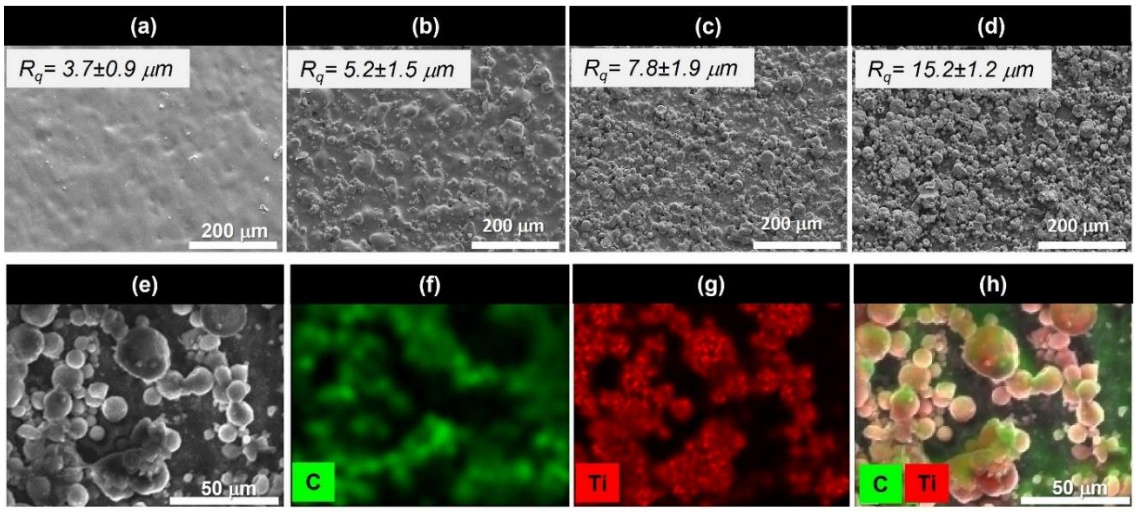

Figure. 19. SEM images ofof FP-based coatings with the increasing Ag-TiO_2 loading: 0 wt.% **a)**, 20 wt.% **b)**, 40 wt.% **c)**, and 80 wt.% **d)**, with the profilometric R_q values were also inserted. A SEM image **e)**, and EDX elemental mapping for carbon **f)**, titanium **g)** and carbon/titanium **h)** content of the r-FP surface (80 wt.% Ag-TiO_2) [85]

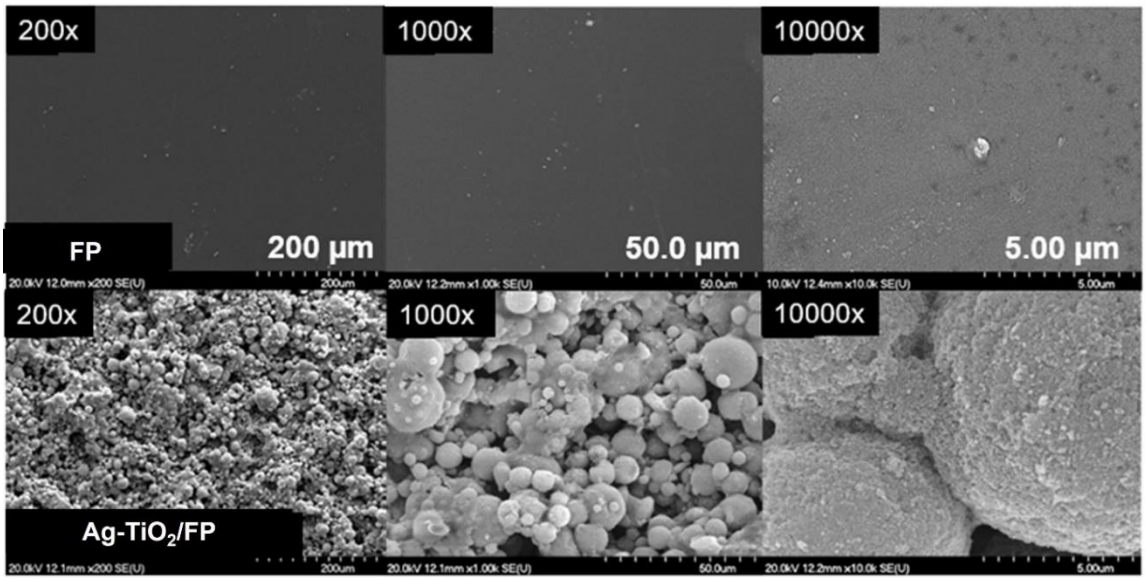

Figure 20. SEM images of smooth spray-coated FP surface (top row) and the r-FP composite at different magnifications [85]

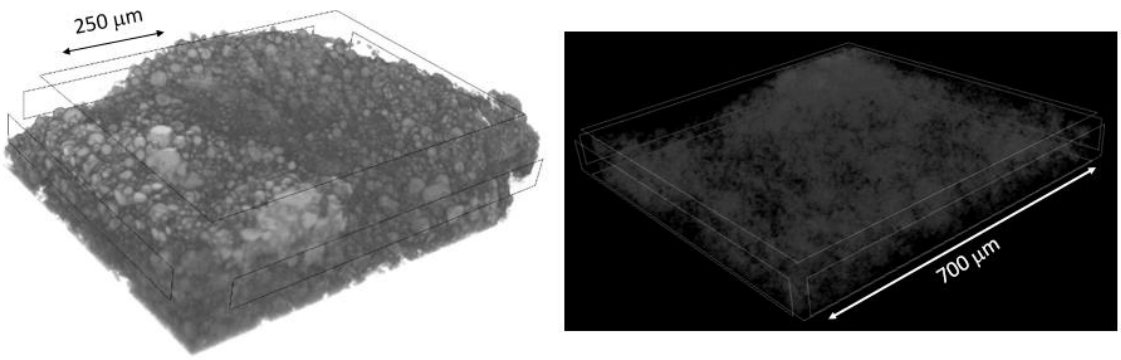

Figure 21. µCT images of an Ag-TiO_2/FP (r-FP) coating; external view (left) and density mapping (right; vacancies are displayed in black) from the same angle [85]

This structure provides high porosity, increased surface area and photocatalyst-accessibility which are beneficial for photocatalytic applications. However, it is also important, that the penetration depth of UV irradiation (254 nm) in the case of porous TiO_2 layers is merely at the magnitude of a few micrometers [165], therefore the radical formation may take place only on the very surface of the ~100 µm thick coating. The overall porosity of the r-FP layer was determined to be 74.8%: the reconstructed image can be seen on **Fig. 21**. This obtained relatively high porosity value is significantly higher than those of other sprayed photoreactive surfaces in the literature [166-168], however, it is important to note that µCT provides the sum of closed- and open porosity, while the related publications mostly provide open porosity data.

5.2.3. Photoreactivity of Ag-TiO_2/FP composite coatings

After the examination of wetting- and morphological properties, the photocatalytic performance of Ag-TiO_2/FP composite coatings was also studied.

At the S/G interface EtOH (g) was applied as test pollutant, as its photodegradation is an extensively studied process and mostly follows the ethanol → acetaldehyde → acetic acid → formaldehyde → formic acid → CO_2 route [63,169]. Despite the many intermediates, for the sake of simplicity, only the EtOH concentration was measured during the degradation experiments.

After 90 min blue LED light irradiation, the layers consist of pure photocatalyst completely decomposed the initial amount (c_0=0.36 mM) of the model compound at the S/G interface, while the composite coatings showed lower reaction rates (**Fig. 22 a)**).

This is in accordance with the lower accessibility of the Ag-TiO_2, due to the surrounding polymer matrix. Among the composites, the EtOH decomposed at the highest rate in the case of superhydrophobic r-FP layers, moreover, an increase was observed regarding the apparent first-order reaction rate constants (from k'=0.0034 min^{-1} to k'=0.0495 min^{-1}) with increasing Ag-TiO_2 content (**Fig. 22 a)**). For the sake of validation, reference photodegradation experiments were also conducted without catalyst (pure FP) and in with an r-FP coating in dark: during this latter measurement, the composite showed low activity (k'=0.0013 min^{-1}). Based on these results, it can be concluded that the presence of the photocatalyst was vital to achieve higher photodegradation efficiency.

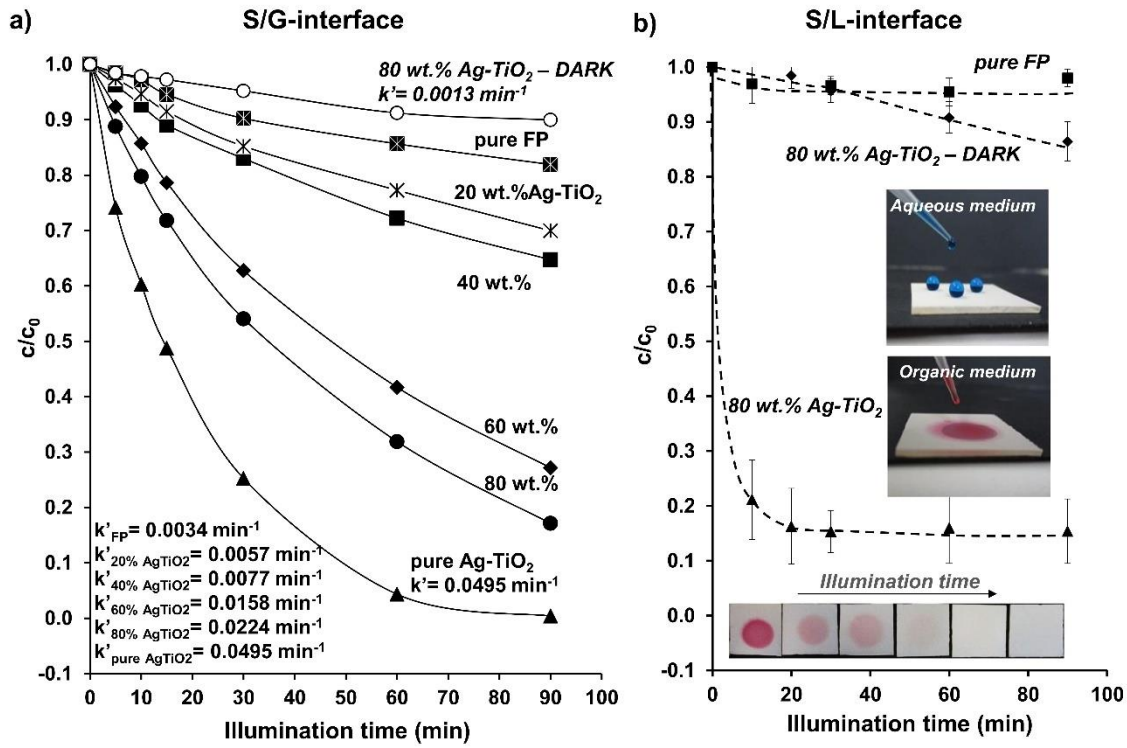

Fig. 22 EtOH (g) (c_0=0.36 mM) photodegradation by the help of Ag-TiO_2/FP composite surfaces and blue LED light (λ_{max}=405 nm). Relative concentrations as a function of illumination time with the determined apparent first-order reaction constants ($\ln(c/c_0)=-k't$) **a)** and the photodegradation of Sudan IV (c_0=0.020 g/l or 52.6 μM) on r-FP coatings as a function of LED-illumination time **b)** [85]

The photocatalytic behavior of the r-FP coatings was also studied at the S/L interface during dye adsorption and degradation tests of model pollutants with different polarities. 50-50 μl portions of organic Sudan IV (0.020 g/l in hexane) and aqueous MB (0.50 g/l) solutions were pipetted on the surface of the r-FP coating. The droplets of the organic Sudan IV solution spreaded completely and the dye was adsorbed on the coating, while the droplets of MB solution rolled off the surface without wetting and staining the composite coating (inserted pictures of **Fig. 22 b)**). Based on the concentration (0.02 g/l) and the volume (50 μl) of the Sudan IV solution and the 1.1 cm^2 area of the resulting dye stain, the specific surface concentration of the adsorbed dye was calculated to be 1.1 $\mu g/cm^2$. The photoinduced degradation and fading of the dye stains (photos in **Fig. 22 b**) was quantified based on diffuse reflectance spectra (calibration curve is shown in **Fig. A4**): the initial specific surface concentration (1.1 $\mu g/cm^2$) was reduced below 0.1 $\mu g/cm^2$ (~90% photodegradation efficiency) as a result of 90 min LED light irradiation. Together with the results of reference measurements, this implies the photocatalytic oxidation of Sudan IV. The photodegradation of Sudan IV by the help of P25 TiO_2 was studied in detail by Aarthi et al. [170].

It can be concluded that at the S/L interface, the photoactivity of the superhydrophobic r-FP coating was dependent on the polarity of the model molecules and the solvent: while the discoloration of apolar Sudan IV stains were efficient, the MB in aqueous solution remained intact due to the inadequate wetting and adsorption (The molecular structure comparison of the model pollutants can be seen in **Fig. A7**). The observed polarity-dependent wetting and photodegradation could be interesting in water treatment scenarios, where the polarity of the pollutants may vary.

5.3. Regulation of wetting and photoreactivity by matrix composition - characterization of Ag-TiO_2/FP+pHEA composite coatings

5.3.1 Wetting properties of Ag-TiO_2/FP+pHEA composite coatings

As it has been shown in the previous chapter, roughening hydrophobic fluorinated polyacrylate coatings by the addition of Ag-TiO_2 photocatalyst led to superhydrophobic character, while the photoreactivity of the catalyst was also influenced by the polymer matrix. To achieve the mentioned extreme water-repellency and the highest possible photoreactivity, the photocatalyst-loading was previously maximized at 80 wt.% (r-FP surfaces).

As I already chose the filler-loading, that leads to surface roughness, sufficient for elaborating extreme wetting characteristics, my next aim was to study the influence of changing matrix composition. For this purpose, hydrophilic poly(2-hydroxyethyl acrylate) (pHEA) (**Fig. 14**) was chosen as a second matrix material (**Chapt. 5.1.3.**). The effect of matrix composition on wettability was studied in the cases of both the sprayed pure polymer films and the Ag-TiO_2-containing composites through static Θ measurements. **Fig. 23** displays the initial Θ values as a function of matrix composition. As it can be seen, the increasing FP content resulted in increasing Θ, which means the pure polymer coatings became more hydrophobic. The pure pHEA coating has a relatively low Θ (27.4°), implying a hydrophilic character, however, at 20 wt.% fluoropolymer content the Θ reached 60° and further increased to 105° at 100 wt.% FP. Θ measurements also confirmed that the 80 wt.% Ag-TiO_2-containing coatings (r-FP and r-pHEA) have ehanced wettability, compared with the initial polymer surfaces, and even superhydrophilic behavior (Θ=0°) was achievevable at 100 wt.% pHEA matrix (r-pHEA). The Θ of smooth polymer layers ranged from 27.4 to 105.0°, however, the wetting character could be broadened by the addition of surface-roughening Ag-TiO_2 (Θ= 0°-150.9°), which indicates the enhancement of wetting character.

Besides static Θ measurements, the FP, pHEA, r-FP and r-pHEA composite coatings were subjected to advancing (Θ_{adv}) and receding (Θ_{rec}) contact angle measurements (**Fig. 24 a)**), as well [12]. In the case of the superhydrophobic r-FP coating, increasing droplet volume resulted in the reduction of Θ from $\Theta_{7.5\mu l}$=165.2° to

Θ_{adv} =$\Theta_{23.0\mu l}$=150.6°. This latter value is almost equal to the initial Θ (150.9°), which was determined after 15 min contact time, indicating the steady state condition in the case of the initial static Θ (**Fig. 23.**). The decrease in Θ upon drop enlargement can be attributed to the porosity of the coating: as the droplet penetrates the micro-/ and or nanostructure, a proposed Cassie-to-Wenzel wetting transition occurs. Upon determining $\Theta_{rec,}$ the measured Θ gradually decreased with decreasing drop volume, resulting in a final value much lower (Θ_{rec}=125.0°) than Θ=150.9°. This is probably a consequence of both the partial polymer-coverage of the hydrophilic photocatalyst particles and the already mentioned high porosity, which can retain the liquid front. In the case of the pure FP coating, the measured Θ_{adv} and Θ_{rec} were ~110° and ~45°, respectively, while in the case of pure pHEA film Θ_{adv}~35° and Θ_{rec}~24°. However, in the case of the superhydrophilic r-pHEA coating, the applied protocol was unable to provide adequate dynamic contact angle data due to the immediate spreading of water droplets, which also confirmed the superhydrophylic character.

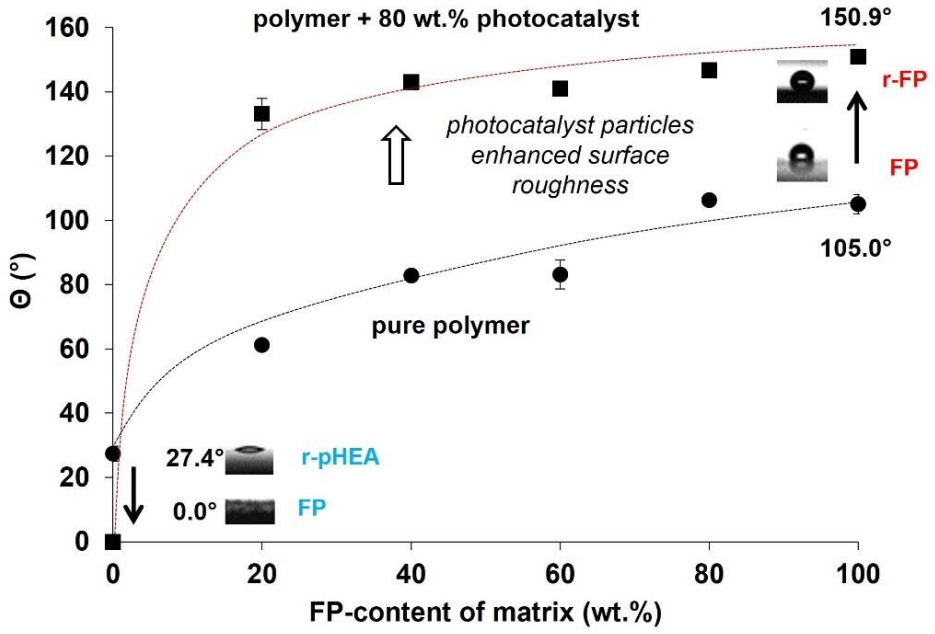

Figure 23. Apparent static water Θ-s of smooth polyacrylate layers and photocatalyst-containing rough composite coatings as a function of the FP content of the polymer matrix (T=25±0.5 °C) [139]

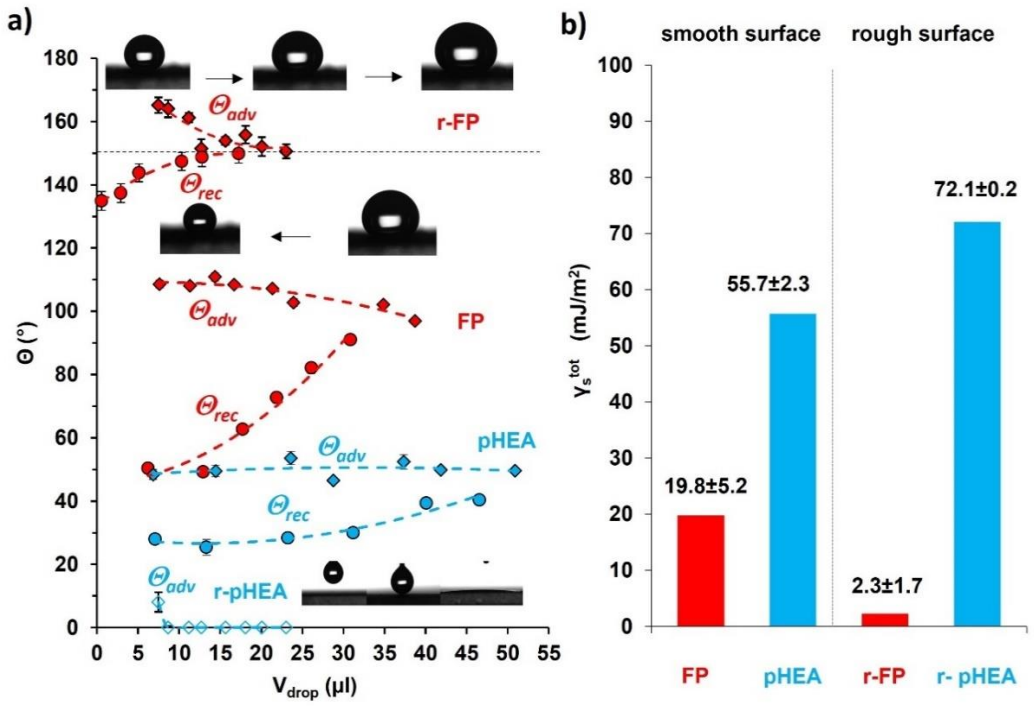

Figure 24. Measured (embedded needle) dynamic water contact angles of smooth pure polyacrylate layers (FP and pHEA) and 80 wt.% Ag-TiO_2-loaded rough composite layers layers (r-FP and r-pHEA) as a function of the drop volume (T=25±0.5 °C) **a)** and the γ_s^{tot} values calculated according to Chibowsky (**Eq. 2** [29]) **b)** [139]

As in the previous chapter, the corresponding surface free energies (γ_s^{tot}) were also determined based on Θ_{adv} and Θ_{rec} data, with the help of the model of Chibowski et al., (**Eq. 2**) [12,29]. The γ_s^{tot} values of pure FP and pHEA coatings were determined to be 19.8±5.2 and 55.7±2.3 mJ/m^2, respectively. The first value compliments with our previous results (**Chapt. 5.2.1.**) and with the literature [163], while the second higher value rather indicates hydrophilic character. The roughening-induced changes of γ_s^{tot} is shown in **Fig. 24 b)**. The increased roughness of a composite with 80 wt.% Ag-TiO_2 led to drastic changes regarding γ_s^{tot}: in the case of high energy (hydrophilic) pHEA matrix the γ_s^{tot} was increased to 72.1±0.2 mJ/m^2, while in the case of low-energy FP, γ_s^{tot} was decreased to 2.3±1.7 mJ/m^2. These results align with the previously observed enhancement of wetting character through the introduction of surface roughness.

The dynamic Θ-s were also determined applying the Wilhelmy method [19]. Each of the plots in **Fig. 25 a)** are recorded during distinct Θ measurements. Before explaining the results, it should be noted, that the dynamic wetting characterization of

superhydrophobic and porous surfaces is difficult and can easily be misinterpreted [171,172], as a reliable dynamic measurement requires homogenous sample, relatively smooth surface, and symmetric shape [19], which are altogether difficult to achieve. In case of a good run, both the slope values of the advancing and receding sections of the Θ vs. immersion depth plots are nearly zero and are equal: this also means, that the top and the bottom sections of the hysteresis loops should be parallel to each other, which is also an indicator of ideal samples and measurements [19].

In the case of the smooth FP coating, these conditions are fulfilled (Θ_{adv}= ~118°; Θ_{rec}= ~33°), however, the r-FP showed irregular hysteresis loop, which is attributed to the rough and heterogeneous surface. The obtained Θ_{adv}=180° should also be handled with skepticism as there are no examples for experimentally obtained Θ, exceeding 180°. However, the water-repellent character of the r-FP coating is shown in the inserted topmost image of **Fig. 25. a)**: the immersion of the superhydrophobized Wilhelmy-plate resulted in dented water surface. On the contrary, meniscus climbed up on the plate in the presence of the superhydrophilic, porous r-pHEA coating due to capillary attraction (Θ_{adv}= ~20°; Θ_{rec}= ~17°).

In conclusion, dynamic Θ measurements also proved the composition-dependence of wettability and the roughness-induced expansion of wetting ranges upon roughening.

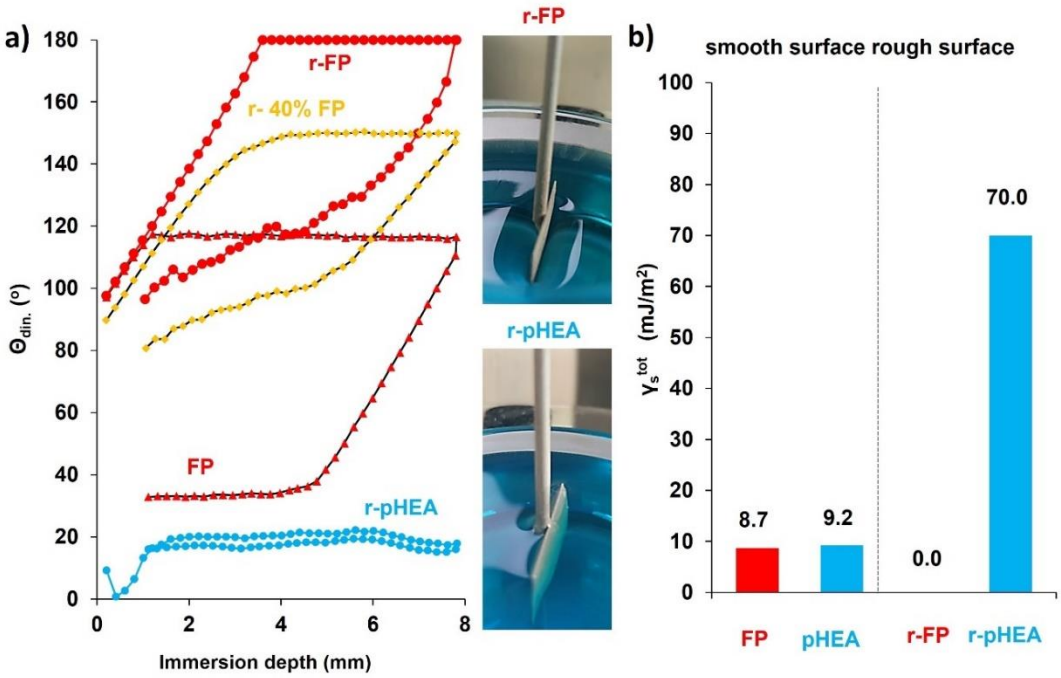

Figure 25. Measured (Wilhelmy-method) dynamic water contact angles of smooth pure polyacrylate layers (FP and pHEA) and 80 wt.% Ag-TiO_2-loaded rough composite layers layers (r-FP 40, r-40% FP and r-pHEA) as a function of plate immersion depth (T=25±0.5 °C) [139] **a)** and the γ_s^{tot} values calculated according to Chibowsky (**Eq. 2** [29]) **b)**

5.3.2 Surface morphology and porosity of Ag-TiO_2/FP+pHEA composites

As it was already presented via the SEM-images of the previous chapter (**Fig. 20**) the photocatalyst-free pure polymer coatings have smooth surface, which was also evidenced by mechanical profilometry (**Fig. 26.**): the measured R_q values of the smooth pHEA and FP coatings were 2.1±0.8 and 3.7±0.9 μm, respectively. As it was previously shown, the photocatalyst-loaded composites were decorated with quasi-spherical (d=5-40 μm) microscale-aggregates of the primer Ag-TiO_2 nanoparticles (**Fig. 19. d), e) and f)**), which is reflected by the the determined R_q values of the r-pHEA and r-FP composites (11.7±2.2 and 15.2±1.2 μm, respectively), while the nanoscale roughness is provided by the unique photocatalyst nanoparticles.

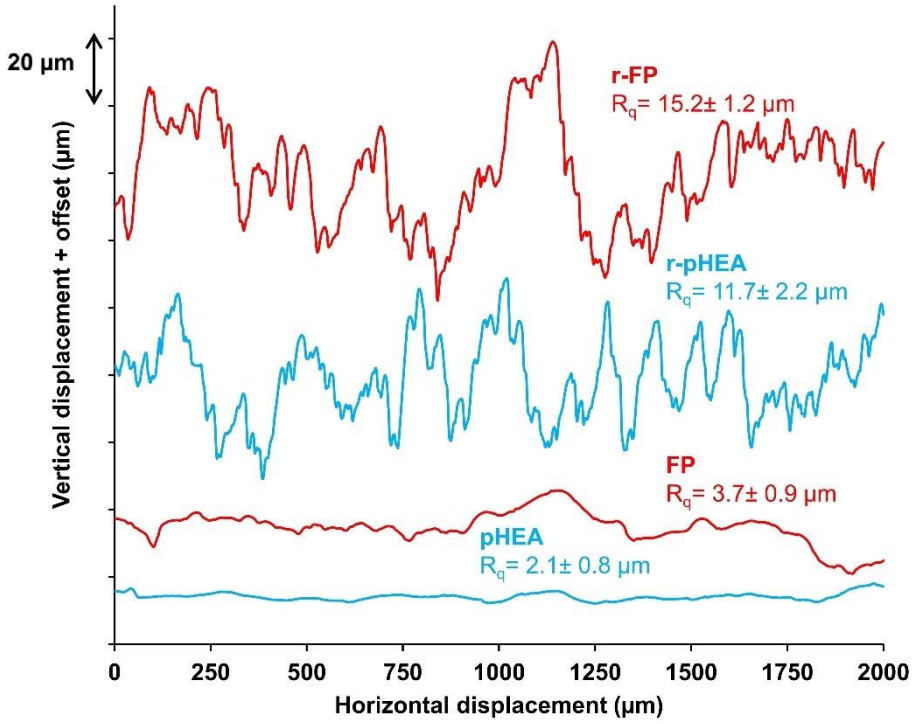

Figure 26. Profilometric curves of smooth polyacrylate (pHEA and FP) and their 80 wt.% Ag-TiO_2-containing rough composites (r-pHEA and r-FP) [139]

This structure also ensures high porosity and accessibility, which is advantageous in photocatalytic applications. However, it is also worth to note again, that the reported penetration depth of UV light (254 nm) into porous TiO_2 film is just a few micrometers [173], therefore the radical formation is only considerable on the very surface porous coatings, as their average thickness of was measured to be 91.3±10.4 µm. Besides thickness measurements, the nominal coating thickness was also estimated to be 19.3±3.2 µm, knowing the applied specific surface amount (5.3±0.5 mg/cm^2) and the previously determined densities of the ingrendients ($\rho_{Ag\text{-}TiO2}$: 4.32 g/cm^3; polymers: ~1.10 g/cm^3). The difference between the two values can be attributed to the high porosity, calculated to be roughly 78.9%, which is in good accordance with the previously measured 74.8% value (**Chapt. 5.2.2.**).

5.3.3. Photocatalytic properties of Ag-TiO_2/FP+pHEA composites

After the wetting- and morphological studies, photocatalytic behaviour at both S/G- and S/L interfaces was also investigated. The photoreactivity of semiconductor composite can be influenced by man factors, as texture, wetting character, and adsorption affinity towards the target chemical species are equally important [174,175].

As a result of 90 min of blue LED light illumination (λ_{max}=405 nm), pure coatings of Ag-TiO_2 were capable of decomposing ~100% of EtOH (g) at the S/G interface (c_0=0.36 mM), while the composites showed moderate reaction rates (**Fig. 27. a)**). Moreover, the apparent first-order decomposition rate constants (k') increased with increasing FP-content (and with increasing hydrophobicity) (**Fig. 27. b)**). The efficiency of direct photolysis (~12%) was exceeded in the case of all examined composites, regardless of their composition and the r-FP coating was capable of decomposing almost as much EtOH (88.3%) as pure Ag-TiO_2 films (99.4%). Therefore, the photoreactivity of these composite surfaces was evidenced at the S/G-interface applying EtOH as model VOC.

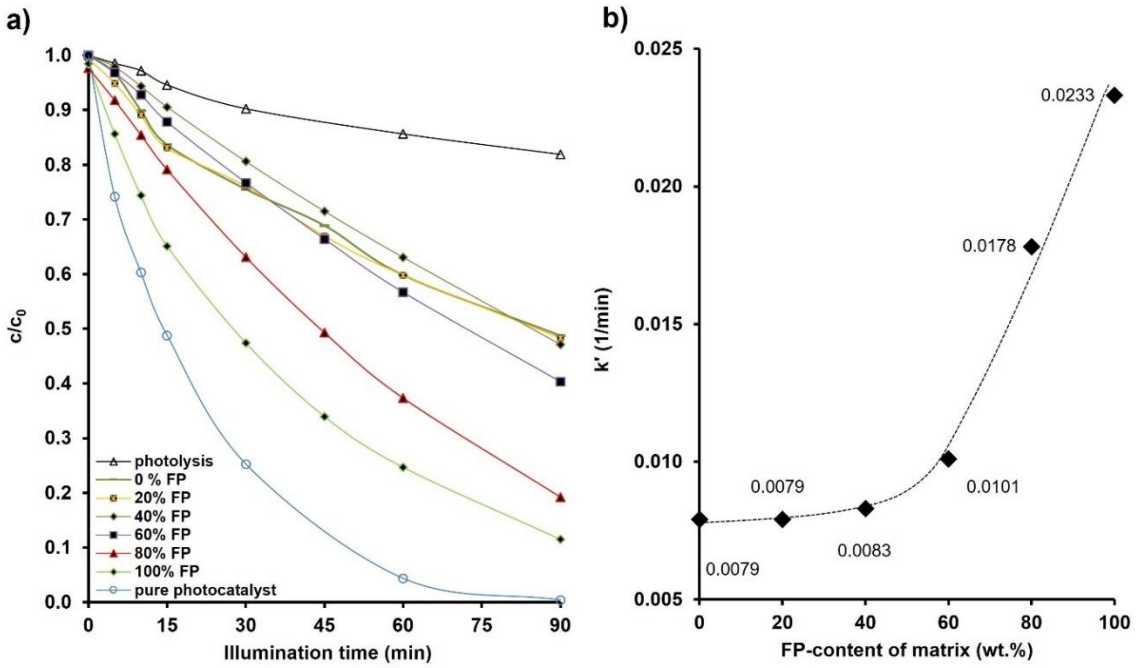

Figure 27. EtOH (g) (c_0=0.36 mM) photodegradation (blue LED, λ_{max}=405 nm) on Ag-TiO_2/FP+pHEA composites; c/c_0 as a function of illumination time **a)** and the determined apparent first-order rate constants for first-order decay (**Eq. 6**) **b)** [139]

The photoreactivity of was also studied at the S/L interface, applying UV-VIS spectrophotometry (**Fig. 28 and 29**) and MB as test molecule. Methylene-blue (MB) is a popular model compound in the evaluation of photodegradation efficiency, as it is easy-to-quantify via VIS spectrophotometry [175]. At neutral pH and in the presence of enough oxigen, the sole reason of the decolorization of MB solutions is the photocatalytic mineralization [175]. While using MB, the emission of the applied light source required to be low in the λ=350-480 nm range to avoid direct photolysis [180]: this condition is fulfilled as the applied blue LED has an emission maximum at λ= 405 nm (**Fig. A3**). Moreover, as the point of zero charge (PZC) of TiO_2 is at pH~6, therefore the adsorption of the positively charged MB molecules (**Fig. A7**) is promoted on the at pH~7 [176].

During the experiments, the aqueous MB solution could not spread on the superhydrophobic r-FP coating (see inserted photo in **Fig. 29 a)**) and therefore only 17.3% of the initial concentration (c_0=0.002 g/l) was decomposed after 90 min illumination.

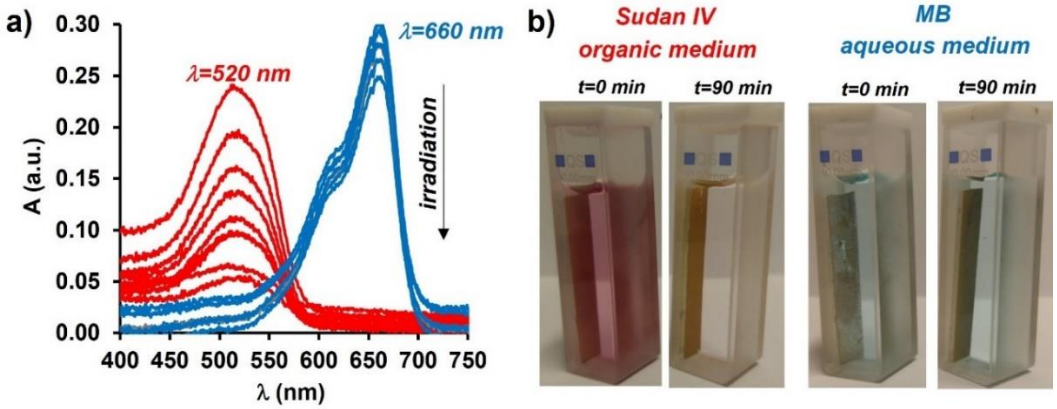

Figure 28. UV-VIS absorbance spectra of MB (c_0=0.002 g/l; 6.25 μM; d.H_2O) and Sudan IV (c_0=0.025 g/l; 65 μM; abs. EtOH) solutions during the photodegradation of dye molecules under blue LED irradiation (λ_{max}=405 nm) **a)** and photos of the superhydrophobic r-FP composite- and dye solution-containing cuvettes, taken after different illumination times **b)** [139]

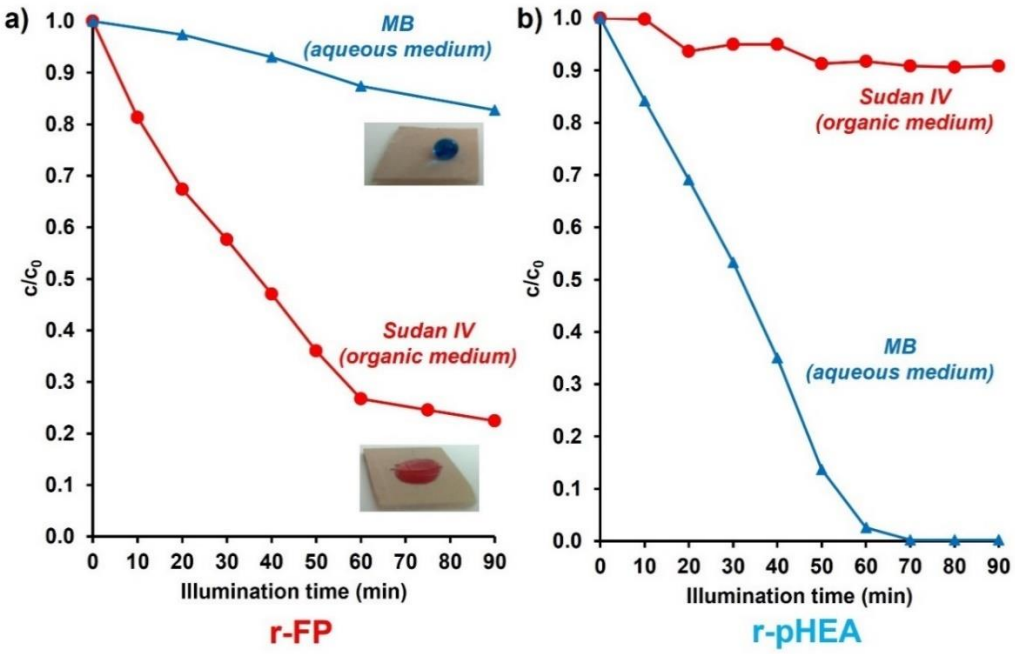

Figure 29. Photodegradation (λ_{max} = 405 nm) of MB (c_0=0.002 g/l; 6.25 μM; d.H_2O) and Sudan IV (c_0=0.025 g/l; 65 μM; abs. EtOH) by superhydrophobic r-FP **a)** and superhydrophilic r-pHEA **b)** composites, represented by relative concentration vs. illumination time curves (c/c_0 vs. t). The inserted photos show the behaviour of the two solutions on the superhydrophobic surface [139]

However, the photodegradation efficiency almost reached 80% in the case of the hydrophobic Sudan IV (c_0=0.25 mg/ml; in abs. EtOH), which can be attributed to the better wettability of the superhydrophobic coating towards the hydrophobic medium (**Fig. 29. a)**), and the resulting increased contact area between the photocatalyst and the dye-solution. When the r-FP coating is immersed into bulk aqueous medium, a layer of air bubbles remains attached to the surface, minimizing the size of the wetted area [177]. This layer can be seen in **Fig. 28. b)**, in the photo taken at t=0, however, it later (t=90) gets removed due to convection (in this scenario, as a result magnetic stirring).

These experiments were applying superhydrophilic r-pHEA composites, as well: in their cases, the results were the opposites, as the MB degradation was complete during the 90 min illumination period, while 91% of the initial amount of Sudan IV remained intact. As the superhydrophilic r-pHEA layer was well-wetted by both the organic and aqueous media, these results can be explained by the different polarities and adsorption affinities of the model pollutants [172,178].

According to the luminometry results (**Chapt. 4.3.20.**), the photocatalytic behaviour of the composite films at solid/water-interface can also be explained by their inherent ability to produce reactive oxygen-containing radicals in composition-dependent concentrations. As **Fig. 30 a) and b)** show, the luminometrically determined free radical concentrations (expressed as H_2O_2-equivalent) increase with the increasing hydrophilic pHEA content of the matrix, which non-surprisingly means that the more wetted a surface is, the higher is the achieved radical concentration and therefore the photodegradation efficiency, as well.

It should also be noted that the photodegradation (and the resulting loss of wetting character) of the polymer matrix by the forming reactive oxidative radicals could mean a problem during long-term irradiation. The effects of this degradation can be overcome by elaborating self-healing character [83,84,86], by applying other, more resistant matrix materials (such as elemental sulfur [179]) or by applying durable composite catalysts [180].

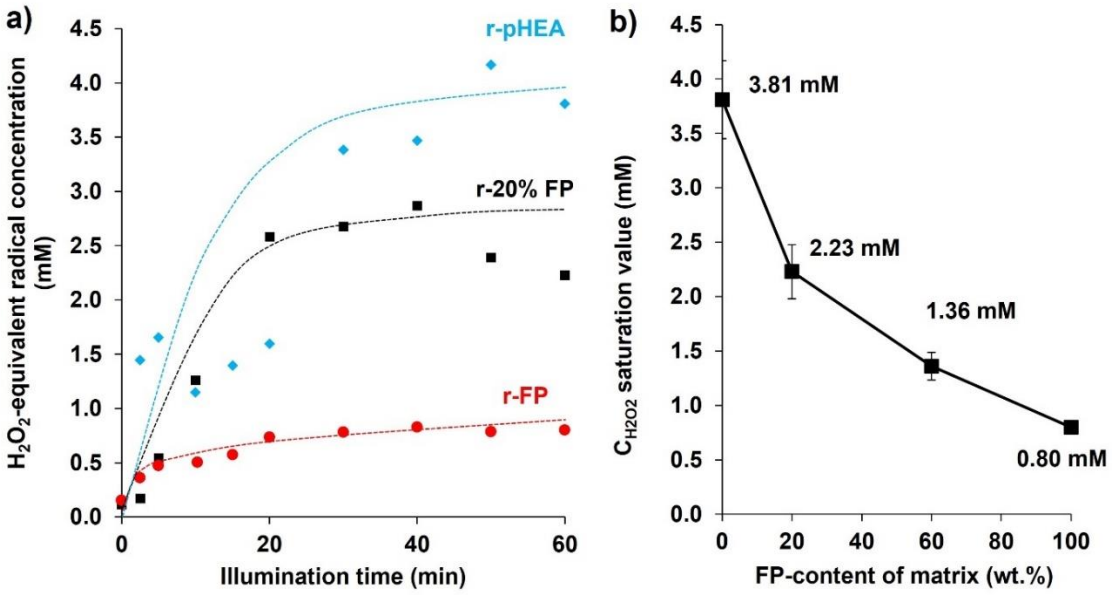

Figure 30. Luminometrically measured H_2O_2-equivalent concentrations of the evolved reactive radicals during the UV-illumination of Ag-TiO_2/FP+pHEA composite coatings as a function of time (the dotted curves are for visualization only) **a)** and the "saturation" values of the radical concentrations after 60 min illumination. **b)**

5.4. Regulation of wetting and photoreactivity by external magnetic field - characterization of Ag-TiO_2+cFe/PDMS grass composites

5.4.1. Morphology of magnetoresponsive Ag-TiO_2+cFe/PDMS composites

As it was presented before, the wettability of a solid is mostly defined by its surface texture and composition, however, in the case of the previously prepared coatings, these conditions were well set and relatively permanent (excluding the effects of chemical and mechanical degradation). In the case of Ag-TiO_2+cFe/PDMS magnetic grass composites, I chose to adjust surface morphology by directing the pillars using external magnetic field: the grass stiffens vertically when the field, perpendicular to the substrate is introduced, resulting in ordered texture, decreased contact area and adhesion between the aqueous phase and the composite, which means higher apparent Θ-s and lower s.a. values [132]. To provide reversible shape- and wetting transitions, the elasticity is a crucial [129-131].

To achieve proper elasticity, a two component, PDMS elastomer (Elastosil C1200 A&B; Wacker) was used as a matrix material, in the previously determined A : B = 1 : 1 (m : m) ratio (**Chapt. 5.1.4.**). To form elastic, hydrophobic composites with dual magnetoresponsivity and phoreactivity, the PDMS was loaded with 50.0-59.2 wt.% cFe microparticles (d=0.5-4 μm; **Fig. 31.**) and 6.3-16.7 wt.% Ag-TiO_2, respectively.

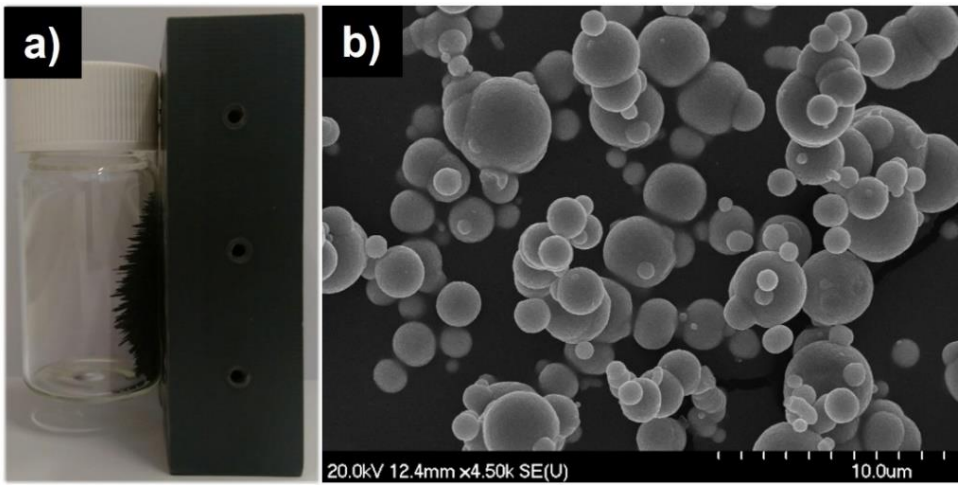

Figure 31. Demonstration of the magnetizability of cFe particles with the help of a bar magnet **a)** and SEM image of cFe particles **b)** [150]

The Ag-TiO_2+cFe/PDMS composites were prepared on glass substrates, exploiting the combination of spray-coating and magnetic field-directed self-assembly, which latter can be attributed to the fact, that magnetic particles also direct each other by their own magnetostatic forces in external magnetic field: these systems achieve free-energy minimum through the formation of ordered structures [133, 181], which in this instance are the Ag-TiO_2+cFe/PDMS strands.

Despite spray-coating is a simple, quick, and scaleable coating method, the product quality is affected by many parameters [182]. The volume of the nebulized droplets (and therefore the surface protrusions, as well) is mainly dependent on the viscosity and the γ_{LG} of the applied dispersion [183], the nozzle geometry, the applied pressure and the sprayed amounts are also crucial [182,183]. To achieve reversible wetting transition with a magnetic grass composite, the proper strand density and geometry (thickness and height) is essential [133], as the distance between the single strands have to be short enough to produce the desired rough surface in the presence of magnetic field, which then results in pinning contact between the strands and the water and therefore a seemingly (super)hydrophobic behaviour. Based on a previous study, these factors are mostly influenced by the applied magnetic flux density (can even be varied by changing the distance between the substrate and the permanent magnet) and the size of the nebulized droplets [133]. While higher flux density usually leads to denser grass [133], the self-assembly is also affected by the magnetostatic interactions between the unique particles, therefore the nebulized drop volume becomes more important as thinner strands attract less nebulized particles than the ones formed upon the drying of bigger droplets.

Yang et al. thoroughly studied the influence of these factors on wettability [133]. Their results imply, that the best way to achieve reversible wetting transitions is the application of a spraying dispersion, containing cFe, PDMS and toluene in an approximately 4.5 : 3 : 7.8 (mass-to-mass-to-mass) ratio, respectively, and the optimal sprayed volume of this dispersion to achieve the optimal grass height of ~2 mm is 3-4 ml. While grass density is important to achieve pinning contact and hydrophobic character in magnetic field, the proper grass height is essential for the collapsed, or randomly oriented state (without magnetic field). The starands have to be high enough to be able to provide increased contact area and adhesion upon collapsing under water droplets (0 T magnetic field), however, -according to my observations- even higher grasses may not be capable of reversible wetting transitions.

Before enhancing a magnetic grass composite with photocatalytic properties, the possible effects of the photocatalyst particle loading over the mentioned parameters has to be considered first. Fortunately, the conducted experiments indicated, that the composites could be loaded with Ag-TiO_2 nanoparticles without the loss of reversibly switchable wetting character. A spraying formula, similar to the published composition [133] was applied (4.5 : 3 : 9 = cFe : PDMS : toluene; mass-to-mass ratio) besides the addition of 0-16.7 wt.% Ag-TiO_2. As the SEM images of **Fig. 32** show, the strands became thicker, and their surfaces became rougher upon increasing the Ag-TiO_2 loading: the formed spherical-like protrusions are similar to those of the Ag-TiO_2/polyacrylate composite surfaces (**Chapt. 5.2.2.**). The grass-density was also reduced upon photocatalyst-addition, as it increased the dispersion density, and therefore the volume of nebulized droplets, as well. As the hydrophilic Ag-TiO_2 has low dispersibility in toluene, the upper limit of the nominal photocatalyst content was set to ~16.7 wt.%. Above this value, extreme aggregation was experienced, leading to the undisered mechanical vulnerability of the final product. In these cases, the adhesion to the glass substrate was insufficient: the strands were peeled off by the applied magnetic field, therefore reversible wetting transitions could not take place. As the dispersibility of cFe has higher dispersibility in both in toluene and in the PDMS matrix, the aggregation and the formation of surface irregularities are less significant without photocatalyst (**Fig. 32)**.

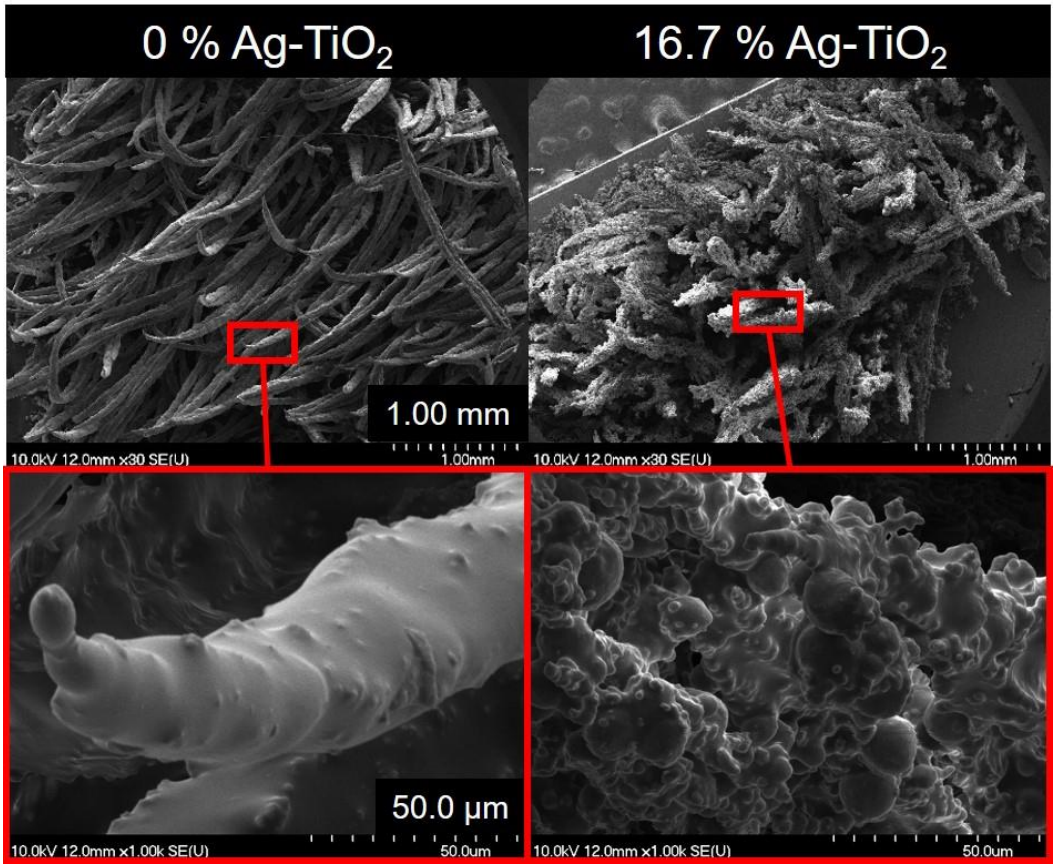

Figure 32. Strands of grass composites (in SEM images) with 0 and 16.7 wt.% nominal Ag-TiO_2 content, cured under 0.35 T magnetic field [150]

5.4.2. Wetting properties of Ag-TiO_2+cFe/PDMS composites

To quantify the magnetic field-dependent wettability of Ag-TiO_2+cFe/PDMS composites, Θ and s.a. measurements were conducted applying a 0.30 T magnetic field (by the proper placement of a permanent bar magnet) with force field lines directed vertically or horizontally to the glass substrate. Both sample series (sprayed and cured in 0.30 T and 0.35 T magnetic fields) were examined and the results are displayed in **Fig. 33**.

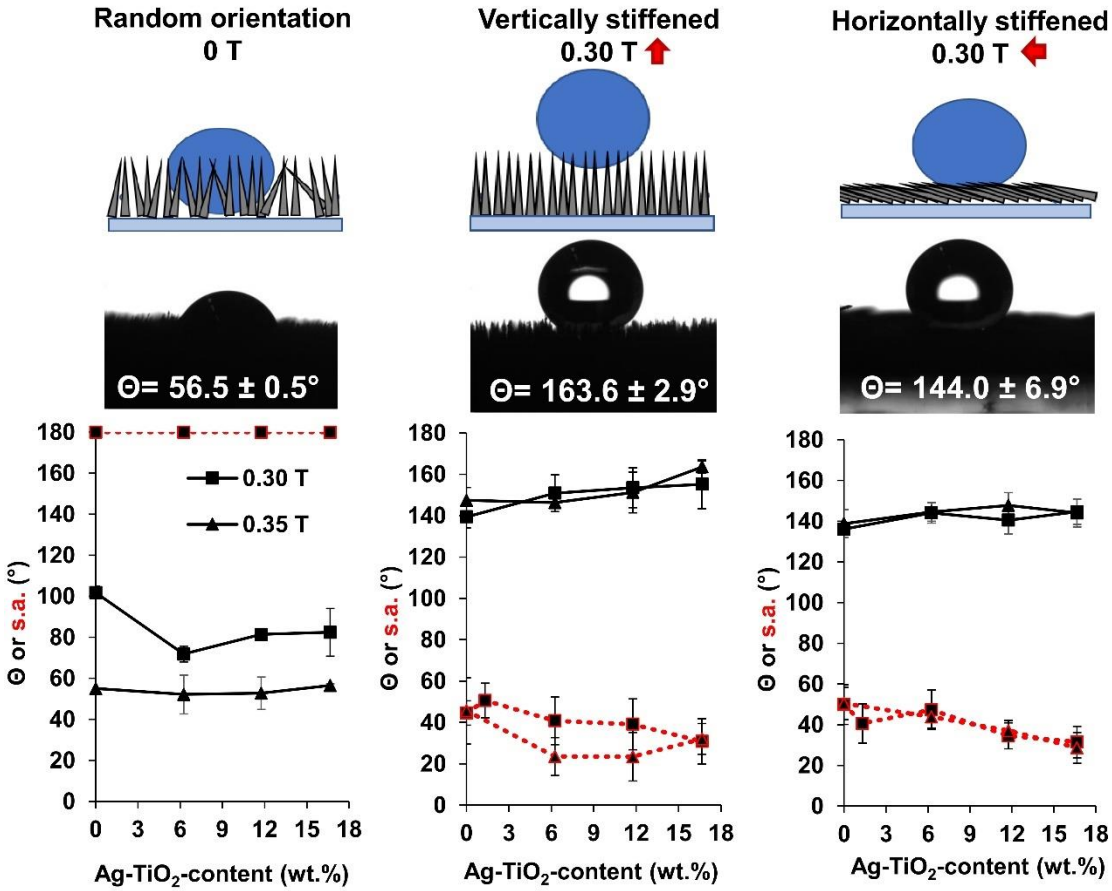

Figure 33. Scheme of the three wetting states and the corresponding drop images of Ag-TiO_2+cFe/PDMS composites with 16.7 wt.% Ag-TiO_2 (top) and apparent water contact (continuous lines) and sliding angles (dotted red lines) on magnetic grasses (cured under 0.30 T or 0.35 T magnetic fields) at the corresponding wetting states, as a function of the nominal photocatalyst loading [150]

As it was previously presented, the enhancement of the magnetic grasses with Ag-TiO_2 photocatalyst nanoparticles increases surface roughness. As a result of this (**Fig. 33**), the vertically stiffened strands (in the middle) have increasingly hydrophobic character, and even superhydrophobicity (150.9°<Θ<163.6°) can be achieved applying higher photocatalyst content (>6.3 wt.%). However, upon the removal of the magnet, the strands can be compressed by the impacting droplets, besides the Θ-s show a slight decrease as the photocatalyst content increases, which is a possible result of the increased overall surface area and the decreased grass density (**Chapt. 5.4.1.**) However, it is important to consider, that the measured Θ-s are apparent values only, as the droplets do not actually spread, but rather penetrate the grass. By other words, a higher

grass with lower density allows deeper penetration, that provides increased contact area and adhesion between the composite and the liquid [133]. This phenomenon was also observed during x-ray μCT measurements: as **Fig. A8** shows, the drop shapes are clearly visible due to the better contrast of μCT.

As it was mentioned before, grass density and wettability can also be dependent on the magnetic flux density: according to **Fig. 33,** also shows that the achievable Θ- and s.a. ranges were broader if a magnetic flux density of 0.35 T was applied, instead of 0.30 T. In vertically stiffened state (middle), the increasing Ag-TiO_2 loading, and roughness led to increasing Θ, as well, while the line contact mode of random orientation (left) has lower Θ-s as the contact area and adhesion increased [133].

Latter claim was evidenced by the exceptionally high s.a. value of 180° (**Fig. 33**, left), which was achievable regardless of the applied photocatalyst content (in the 0-16.7 wt.% range). However, upon vertical stiffening, the s.a. gradually decreases with increasing Ag-TiO_2 loading.

Besides studying the vertically stiffened- and randomly oriented states, the Θ-s and s.a.-s were also measured on horizontally stiffened composite strands (**Fig. 33**, on the right). This was achievable through turning the bar magnet by 90°, resulting in force field lines parallel to the substrate surface. Considering wettability, the horizontal- and vertical alignments are alike, as the rough-sided horizontal composite strands possess Θ-s almost identical to those of the vertically stiffened ones (**Fig. 33**, in the middle), which indicates similarities in the spacings between the tips of vertical strains and between the surface protrusions on their sides.

Although, the already presented literature example [133] describes broader s.a. ranges (e.g. 8-180°) in the case of the application of higher magnetic flux density during preparation (4.5 T), the examined flux density range (0.30-0.35 T range) had only a minor effect on wettability and led to narrower ranges.

However, thanks to the still broad s.a. ranges and the fast-response reversible switching, the Ag-TiO_2+cFe/PDMS composites (regardless of the composition) are capable of picking up and releasing water droplets. As **Fig. 34** shows, without magnetic field the randomly aligned strands (s.a.=180°) pick up a water droplet from a superhydrophobic r-FP coating, while upon the introduction of the 0.30 T permanent magnet, the droplet is released by the stiffening grass (Θ=163.9±2.9°, s.a.=32.0±7.4°) (**Fig 33**). This catch-release cycle is repeatable, regardless of the applied preparation conditions (0-16.7 wt.% Ag-TiO_2 or 0.30-0.35 T magnetic field), which provides robust

and versatile liquid manipulation capability and the subsequently presented visible light photoreactivity, as well.

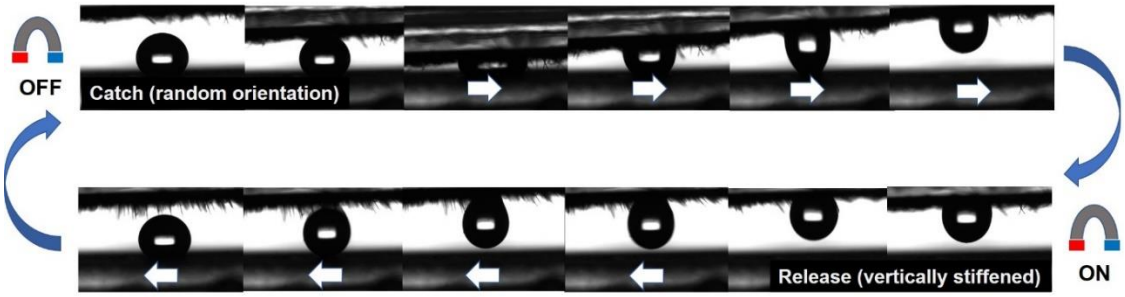

Figure 34. Water droplet catch-release cycle of an Ag-TiO_2+cFe/PDMS coating (16.7 wt.% Ag-TiO_2) [150]

Besides the presented Θ values of droplets (**Fig. 33**.), the magnetoresponsive wettability was also studied with bulk aqueous phase. As the images in **Fig. 35.** show, the position of a non-wetting region of the composite surface can arbitrarily be changed by changing the position of a 0.30 T bar magnet below the sample.

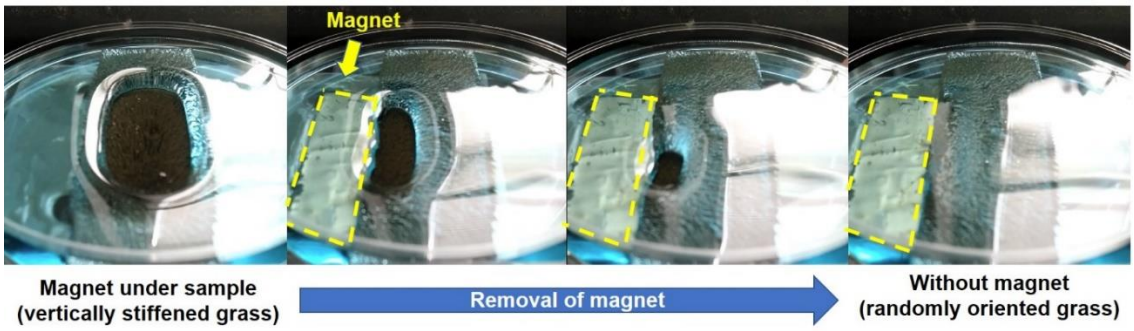

Figure 35. Magnetoresponsive wettability of an Ag-TiO_2+cFe/PDMS composite, demonstrated applying bulk aqueous phase [150]

5.4.3. Magnetic field-tailored photocatalytic properties of Ag-TiO_2+cFe/PDMS composites

In the followings, I studied the relation between the magnetoresponsive wettability and the photoreactivity of the composites during MB photodegradation experiments. As it was previously presented, the r-FP coating could only degrade ~20% of the MB in aqueous solution after 90 min illumination (blue LED-lamp; λ_{max}=405 nm) (**Chapt.**

5.3.2.), while in the case of Ag-TiO_2+cFe/PDMS composites with 63.3±1.6 mg/cm^2 specific mass and 16.7 wt.% nominal photocatalyst content, the hydrophobic character also led to moderate efficiency, which was also influenced by the external magnetic field (**Fig. 36**): without magnet, the grass collapsed under the liquid (**Fig. 35**), resulting in higher wetted area and higher photocatalytic efficiency (47.6±5.1% after 300 min), while when a 0.30 T magnet is placed under the sample, the photocatalytic efficiency was significantly lower due to the porr wetting and the pinning contact. **Fig. 36 a)** shows the absolute concentration changes with the corresponding adsorbed amount of MB, while **Fig. 36 b)** shows the relative (c/c_0) changes in MB solution concentration during LED light illumination.

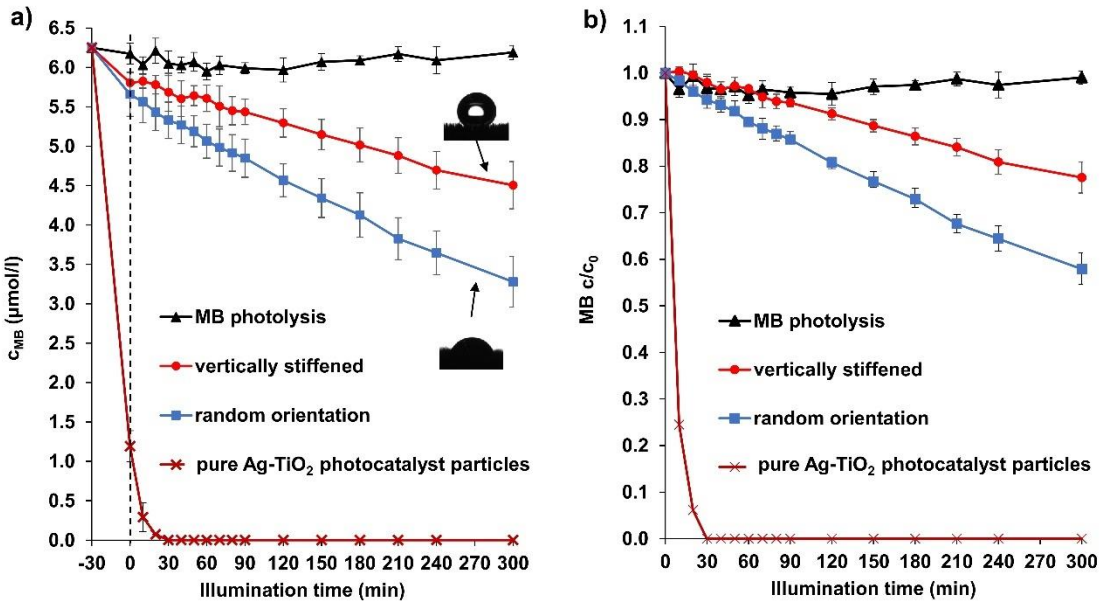

Figure 36. Changes is the absolute **a)** and relative **b)** concentrations of MB (c_0=2 mg/l M) during its photodegradation (blue LED; λ_{max}=405 nm) by the help of Ag-TiO_2+cFe/PDMS composites (63.3±1.6 mg/cm^2; 16.7 wt.% Ag-TiO_2) with different grass orientations. The direct photolysis of MB and the photocatalytic efficiency of pure Ag-TiO_2 are also displayed as references. [150]

The calculated photodegradation efficiencies were 42.1±3.5% (random orientation) and 22.4±3.3% (vertically stiffened), respectively after the 300 min illumination (**Fig. 36 b)**). Based on the preparation procedure, the nominal Ag-TiO_2 content of these samples were 0.208 g, therefore the MB degradation test were repeated repeated with this amount of pure Ag-TiO_2 as reference. During these tests, the pure

Ag-TiO_2 nanopowder completely decomposed the applied amount of MB (c_0=2 mg/l M), which is non-surprising as the well-dispersed, hydrophilic photocatalyst particles have higher accessible surface area (BET surface area of 53.5 m^2/g) than the composites (0.15 m^2/g). However, the photolysis of MB turned out to be insignificant (**Fig. 36**), and therefore it only had a minor contribution to the decolorization of MB solutions.

Thanks to the magnetoresponsive wetting and photoreactivity, the Ag-TiO_2+cFe/PDMS composites may seek further applications as sophisticated liquid manipulation tools.

5.5. Regulation of wetting and photoreactivity by temperature - characterization of Ag-TiO_2/PDMS-gr-pNIPAAm composite coatings

5.5.1. Characterization of pNIPAAm-grafted PDMS (PDMS-gr-pNIPAAm)

PDMS is an ideal candidate as a base material to form thermoresponsive surfaces as it is easy-to-process, has beneficial easy-to-tune elasticity, high chemical and mechanical resistance and its crosslinked networks can easily be enhanced by covalently bound ATRP-initiators to promote surface pNIPAAm-growth, which leads to the desired thermoresponsive wetting characteristics.

In this work I applied 10-undecenyl 2-bromoisobutyrate (initiator; INI) as a PDMS-compatible ATRP-initiator, that has well-described synthetic methods and characteristics in the literature [151,184].

As **Fig. 37 a)** shows, the INI is covalently bound to the PDMS-network by the Pt-complex catalyst content of the applied two-component Elastosil C1200 PDMS: besides keeping the optimal (1 :1 = m : m) ratio between the two PDMS-component (**Chapt. 5.1.4**) the increasing amount of added INI can result in a drastic decline of crosslinking density and therefore, elasticity. According to a previous study, the optimal m : m ratio between the PDMS and the INI is 11 : 0.13 (1.2 wt% INI), and the recommended upper limit is 11 : 0.5 (4.3 wt% INI) when Sylgard 184 PDMS is applied: if the INI content is increased above this level, the resulting copolymer might have viscous characteristics [114]. The results of our oscillatory rheology measurements (G' and G" vs. deformation curves in **Fig. 37 b)**) on bulk PDMS-co-INI samples support

these statements: it can be seen on Fig. 1 c), that the storage- (G') and loss moduli (G'') of the copolymers at 1% deformation show decreasing tendency with increasing INI content, indicating a more viscous character as the crosslinking density decreases. The G' values range from 141000 Pa to 5660 Pa and the G" values range from 18000 Pa to 2640 Pa with increasing INI content in the examined composition range (0-4.3 wt% INI).

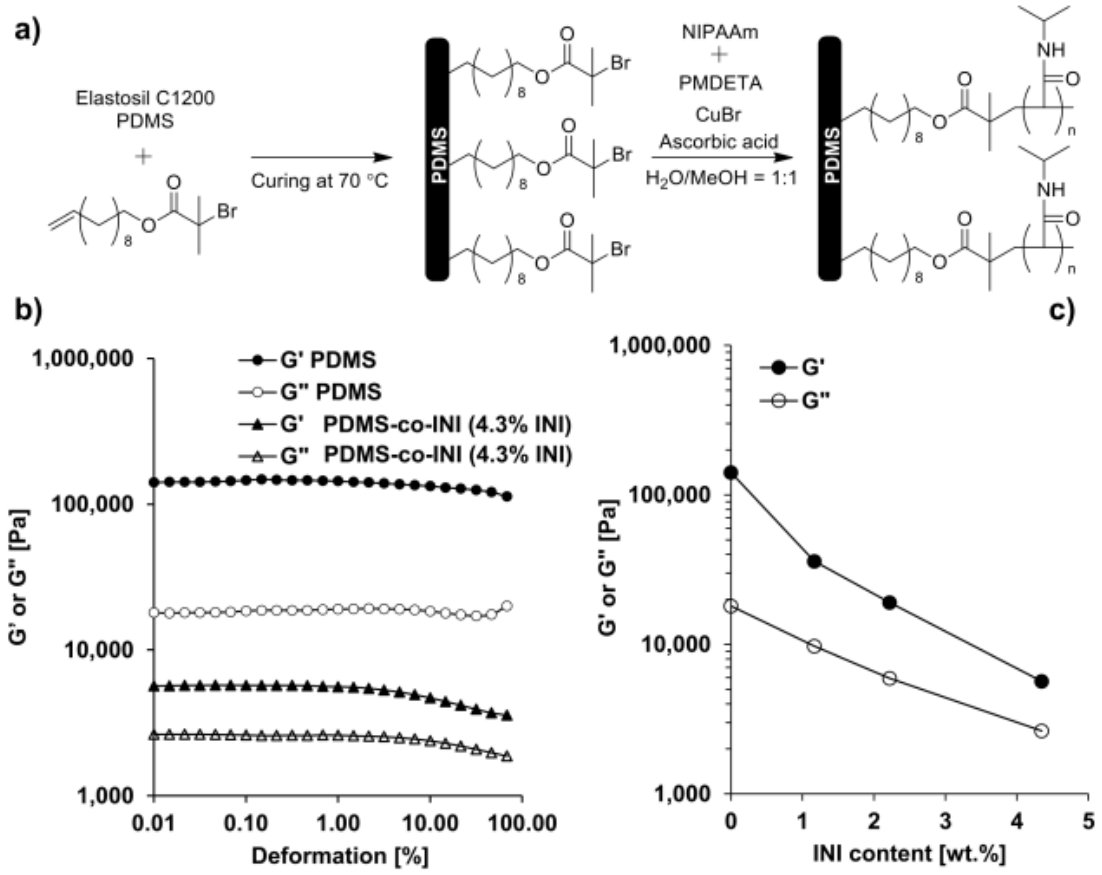

Figure 37. Synthetic scheme of PDMS-gr-pNIPAAm **a)** characteristic storage (G') and loss (G") moduli of PDMS and PDMS-co-INI (4.3 wt% INI) samples vs. the applied deformation **b)** as well as the evolution of G' and G" of PDMS-INI as a function of INI content at 1% deformation **c)** [185]

However, in our case the apparent elasticity and mechanical stability of PDMS-co-INI (4.3 wt% INI) bulk samples and thin films were still acceptable to conduct contact angle (Θ) measurements, and therefore this composition was also used in the following wetting studies to produce higher surface pNIPAAm-densities.

XPS measurements were also performed to charaterize the composition of the prepared surfaces (**Fig. 38**). The survey scans (**Fig. 38 a)**) reveal similar chemical composition for the PDMS-co-INI, PDMS-gr-pNIPAAm and Ag-TiO_2/PDMS-gr-pNIPAAm films. The main chemical species present can be attributed to the PDMS matrix (C: 49.4 at%; O: 24.2 at%; Si: 26.3 at%; Br: 0.1 at%), with binding energies in good accordance with previously published results (**Table A1 and A2**) [184,186]. The high resolution scans reveal faint Br 3d core lines (~70.22 eV) which indicate the presence of covalently bound INI in the copolymer surfaces (**Fig. 38 b)**).

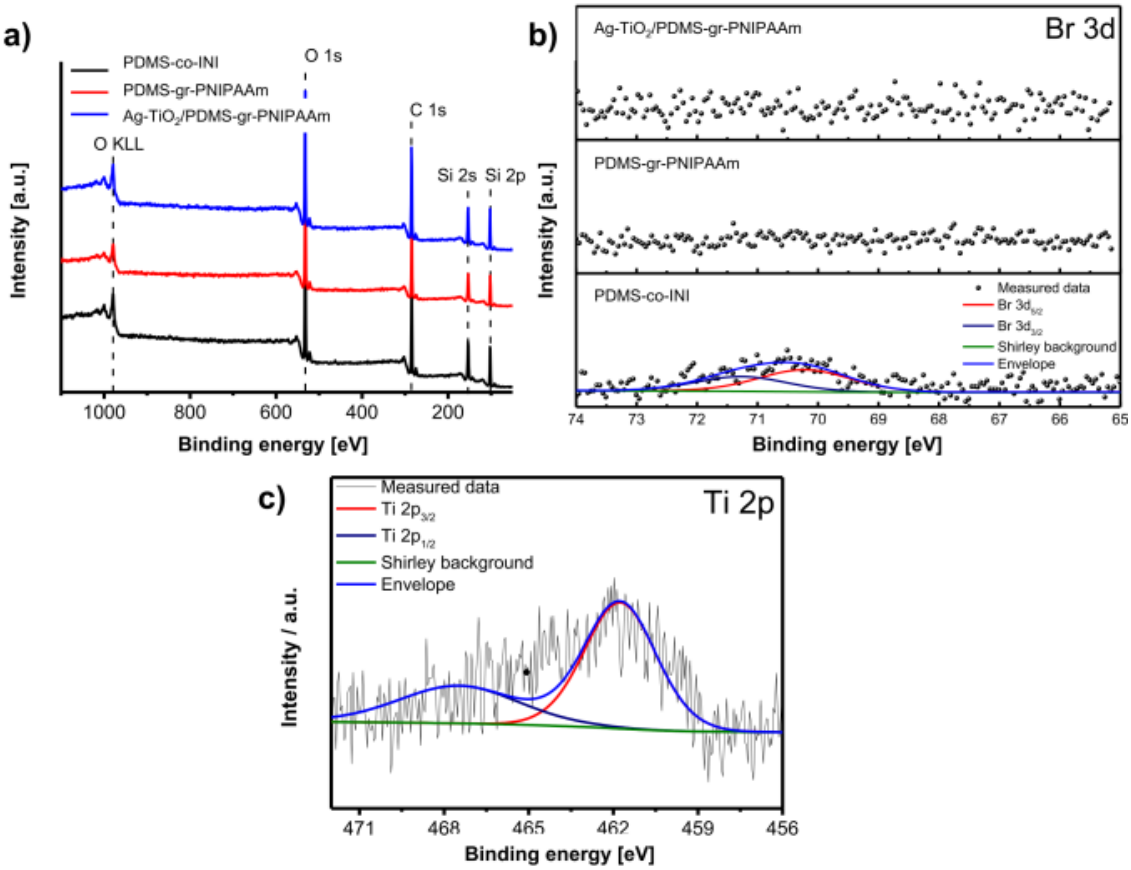

Figure 38. XPS-spectra of doctor blade-casted PDMS-co-INI, PDMS-gr-pNIPAAm and Ag-TiO_2/PDMS-gr-pNIPAAm films (4.3 wt% INI; 5 M pNIPAAm) **a)** indication of the Br 3d peak in all three samples **b)** Ti 2p peak from the XPS-spectrum of the Ag-TiO_2/PDMS-gr-pNIPAAm film **c)** [185]

The 200 µm thick, doctor blade-casted PDMS-co-INI layers (1.2 or 4.3 wt% INI) were charged with different concentrations (0.30, 0.60, 1.25, 2.50, 5.00, 6.25, 7.50 or 10.00 M) of NIPAAm monomer solution during ARGET-ATRP grafting to achieve the desired thermoresponsive characteristics of the resulting PDMS-gr-pNIPAAm layers

(**Fig. 37 a)**). The successfulness of the grafting process is evidenced during the application of various spectroscopy methods on PDMS-gr-pNIPAAm (4.3 wt% INI; 5 M NIPAAm) films. As the Raman-spectra of **Fig. 39** show, the peak – characteristic to the double bond of NIPAAm – at 1622 cm^{-1} Raman-shift [134] diminishes during the grafting process, however, the 2958 cm^{-1} peak of the isopropyl group (C-H symmetric streching vibration) remains in the spectrum of the final product with high relative intensity, indicating the formation of the grafted polymer chains with relatively homogeous distribution (at 1 μm lateral resolution) on the surface. This was evidenced via the relative intensity-mapping of the 2958 cm^{-1} peak (**Fig. 39**). On the contrary, the XPS-spectra of the PDMS-gr-pNIPAAm layer does not indicate the presence of nitrogen atoms (**Fig. 38 a)**) (possibly due to the low sensitivity of the technique towards nitrogen [187]) in the sample, and the elemental composition appeared to be very similar to the PDMS-co-INI films', however, the Br 3d peak at ~ 70.22 eV binding energy diminishes after the grafting step, which can be attributed to the consumption of the surface initiator (**Fig. 38 b)**). Latter can be explained by the fact, that as ATRP is a radical polymerization process, the polymer chains which are terminated by -Br are statistically less in number, since Br-radicals and growing polymer chain radicals are also capable of homologous recombination. [188]

The presence of pNIPAAm-associated surface nitrogen content was evidenced by EDX-spectroscopy (**Fig. 40 a) and b)**): as a result of monitoring the nitrogen K_α (0,396 eV) line, the nitrogen content of the surfacial layer was given to be 17.5±6.3 % and homogenously distributed along the surface in the case of PDMS-gr-pNIPAAm films, which is in good accordance with the results of Raman-mapping (**Fig. 39**) The differences between the XPS and EDX elemental analysis results can be explained by the previously mentioned low sensitivity of XPS towards nitrogen [187] and the different depth-profile capabilities of the two techniques: as the photoelectrons (XPS) are originated from the upper ~10 nm layer of the surface, the X-ray photons (EDX) can provide information on the composition of the upper 1-2 μm [189].

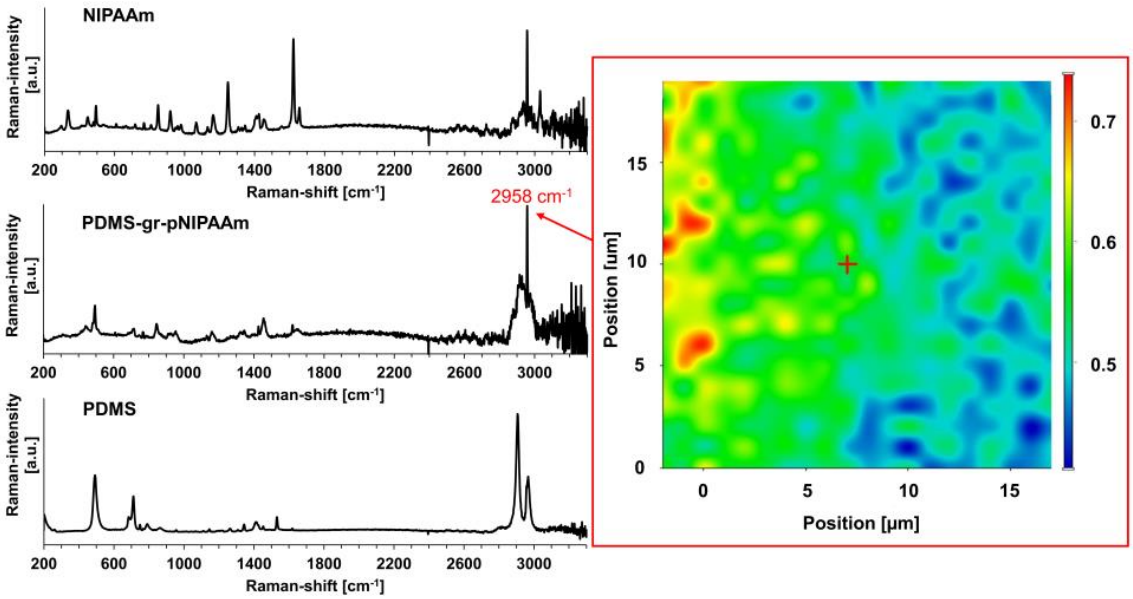

Figure 39. Raman-spectra of the NIPAAm, the initial PDMS and the PDMS-gr-pNIPAAm copolymer and the Raman-intensity heatmap of the peak with 2958 cm^{-1} Raman-shift along the surface of a PDMS-gr-pNIPAAm film (4.3 wt% INI; 5 M NIPAAm) [185]

To enhance the thermoresponsive layers with visible light photocatalytic activity, Ag-TiO_2 photocatalyst nanoparticles were incorporated into the PDMS-gr-pNIPAAm copolymer matrices.

By dispersing 15 wt% Ag-TiO_2 in the doctor blade-casted and spray-coated layers of PDMS-co-INI matrix, Ag-TiO_2/PDMS-co-INI composite layers were prepared. Grafting these layers with pNIPAAm results in the formation of the so-called Ag-TiO_2/PDMS-gr-pNIPAAm surfaces. As **Fig. 40 b)** shows, the EDX-spectrum of Ag-TiO_2/PDMS-gr-PNIPAAm (1.2 wt% INI; 5 M NIPAAm) indicates the presence of titanium on the surface in a moderate amount (~1 at%). This is in good accordance with the recorded XPS-spectra and elemental analysis (**Fig. 38 c), Tables A1 and A2**), as the Ti $2p_{3/2}$ peak is visible at 461.76 eV binding energy value greatly shifted to a more positive value from the literature value of Ti(IV) in TiO_2 (Ti $2p_{3/2}$ = 458.5 eV) [189]. This can be attributed to specific charging of the incorporated TiO_2 into the polymer matrix coupled with the low signal intensity. The derived Ti content from these is 0.2 at% (where the theoretical value is 0.7 at%). Similar to the previous results (**Fig. 38**), the XPS spectrum of Ag-TiO_2/PDMS-gr-pNIPAAm (1.2 wt% INI; 5 M NIPAAm) still does not contain any peaks related to surface nitrogen, however the element could be detected during EDX measurements in this case, as well (**Fig. 40**). According to the

recorded SEM-images (**Fig. 4**), the incorporated photocatalyst nanoparticles also enhance the surfaces with considerable surface roughness, which affected the surface wetting properties, as it is detailed in the following section. The detailed results of the XPS and EDX elemental analyses are shown in **Table A2 and A3**.

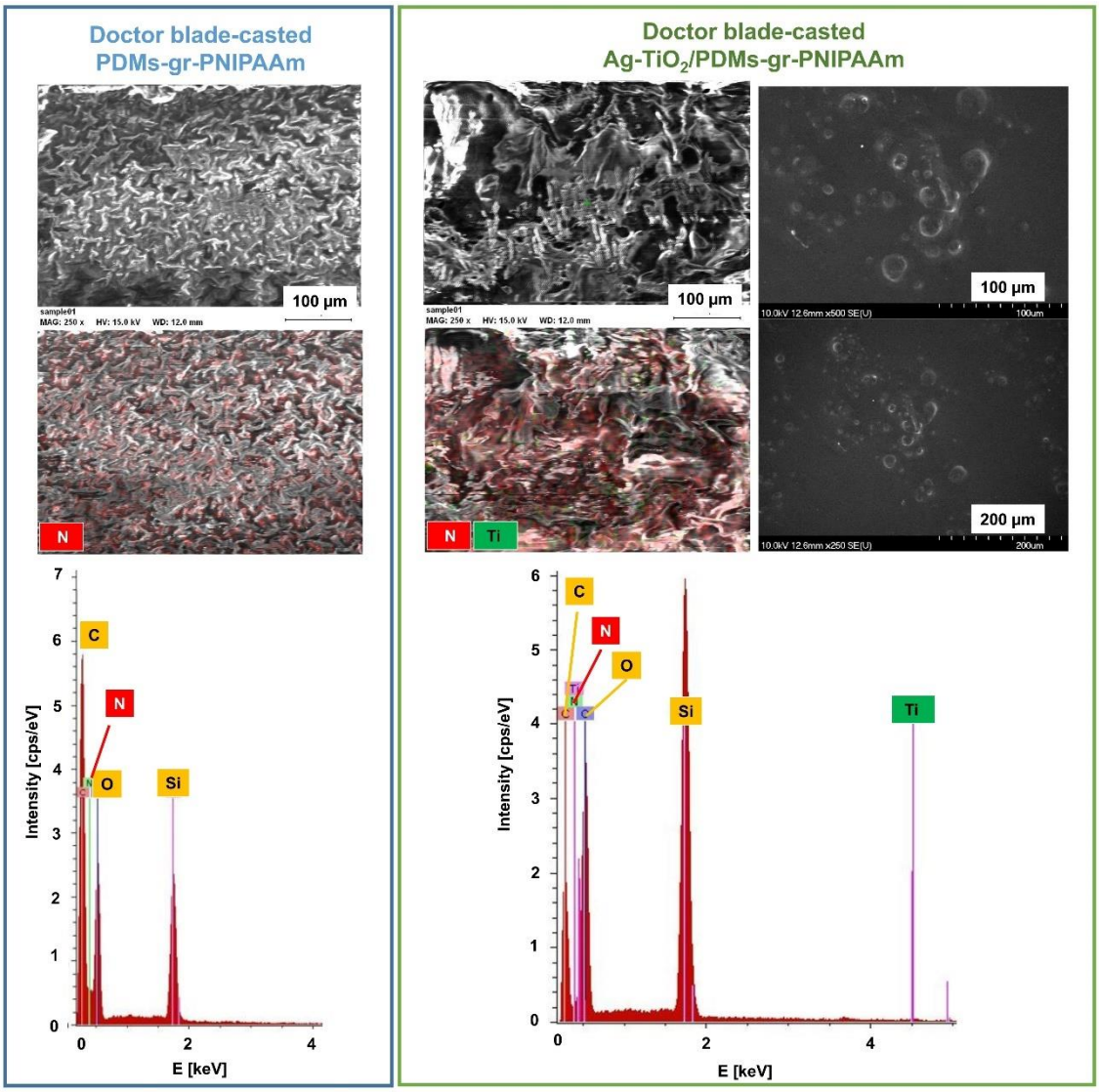

Figure 40. EDX-spectra and SEM-images of PDMS-gr-pNIPAAm and Ag-TiO_2/PDMS-gr-pNIPAAm surfaces (1.2 wt% INI; 5 M NIPAAm) with the distribution of nitrogen and titanium [185]

5.5.2. Thermoresponsive and composition-dependent wetting of PDMS-gr-PNIPAAm and Ag-TiO_2/PDMS-gr-pNIPAAm coatings

As it is already well known, the pNIPAAm owes its thermoresponsive wetting characteristics to its LCST at ~32 °C, above which an entropy-controlled precipitation occurs. In the case of our PDMS-gr-pNIPAAm (4.3 wt% INI) films, the heat effect of the desolvation of surface PNIPAAm-chains can be measured by DSC in the case of samples, prepared applying higher monomer concentrations (>2.5 M NIPAAm) during grafting: **Fig. 41 a)** indicates, that the measured LCST on the pNIPAAm-grafted polymer surfaces is somewhat higher (endothermic peak at ~34 °C) than in the case of the two-component pNIPAAm-water systems (~32 °C) [121], which can be attributed to the applied relatively high (2 °C/min) heating- and cooling speed during the DSC measurements. However, it is noteworthy that the temperatures of the peak maxima of the heating and cooling (exothermic peak of dissolution at 29-30 °C) processes give the expected average of ~32 °C. The heat-effect of the dissolution could only be detected when samples with higher (>2.5 M) monomer concentration were examined. Moreover, the prepared surfaces showed excellent thermal stability up to more than 300 °C in air atmosphere (TG-curves of **Fig. 41 b)**), which indicates their applicability in broad temperature ranges.

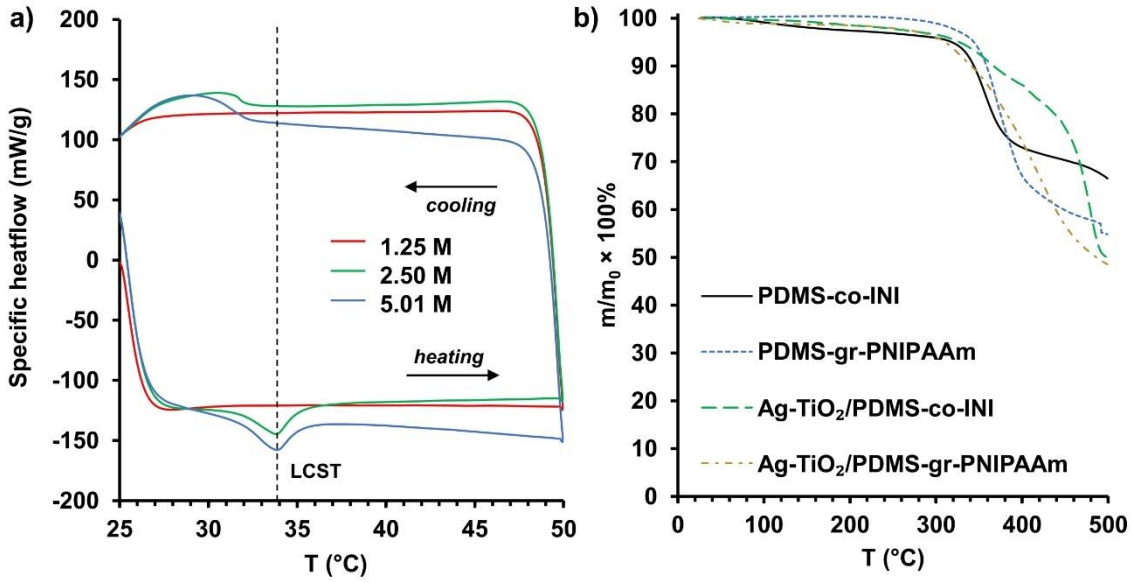

Figure 41. a) DSC-curves of PDMS-gr-pNIPAAm (4.3 wt% INI; 1.25, 2.00 and 5 M NIPAAm) films and **b)** TG-curves of PDMS-co-INI, PDMS-gr-pNIPAAm (4.3 wt% INI; 5 M NIPAAm) and their composites containing 15 wt.% Ag-TiO_2 [185]

After proving the presence of pNIPAAm chains on the PDMS surfaces by the means of DSC and the other analytical methods, the pNIPAAm-influenced wetting properties were also studied in details.

To quantify the thermally induced changes in wetting characteristics, Θ measurements were conducted on the pNIPAAm-grafted surfaces at 25, 40 and in some cases at 50 and 60 °C, applying the sessile drop technique. According to my observations at room temperature, the water droplets on the pNIPAAm-containing surfaces initially possess Θ-s similar to the ones, characteristic to the pure smooth PDMS surfaces (~105°), but they gradually decrease over time until reaching a minimum quasi-equilibrium value, after approximately 1 min. As **Fig. 42** shows, this contact-angle decline is dependent on the grafting monomer concentration, as higher NIPAAm concentrations presumably lead to longer PNIPAAm-chains and therefore, increased adhesion and wettability towards the sessile water droplets (up to 31.9° Θ difference between the 1 min wettabilities at 25 °C). The time-dependency of Θ and non-immediate spreading of the droplets could be explained by the gradual solvation of surface-bound pNIPAAm chains, which is attributed to the solvent-induced reorientation [190,191]: in a non-wetted state, the hydrophobic bakcbone of the polymer is oriented towards air, while the aqeous medium interacts with the hydrophilic amide goups, causing the observed hydrophobic-to-hydrophilic transitions over time. At 40 °C this Θ decrease is less significant (4.6°) as the temperature is above the LCST and the solvation of pNIPAAm does not occur (**Fig. 42**).

An another Θ-influencing factor is the rate of droplet evaporation: **Fig. 42** also shows that above 40 °C, the increased evaporation-rate results in more decreased Θ values after 1 min time intervals. **Fig. 42** also evidences the expected thermoresponsive wetting characteristics of the PDMS-gr-pNIPAAm surfaces: the equilibrium Θ values are higher above the LCST, which means a more hydrophobic character as the surface-bound pNIPAAm chains and the water become immiscible with eachother (Θ-s ranged from 48.0° to 108.7°).

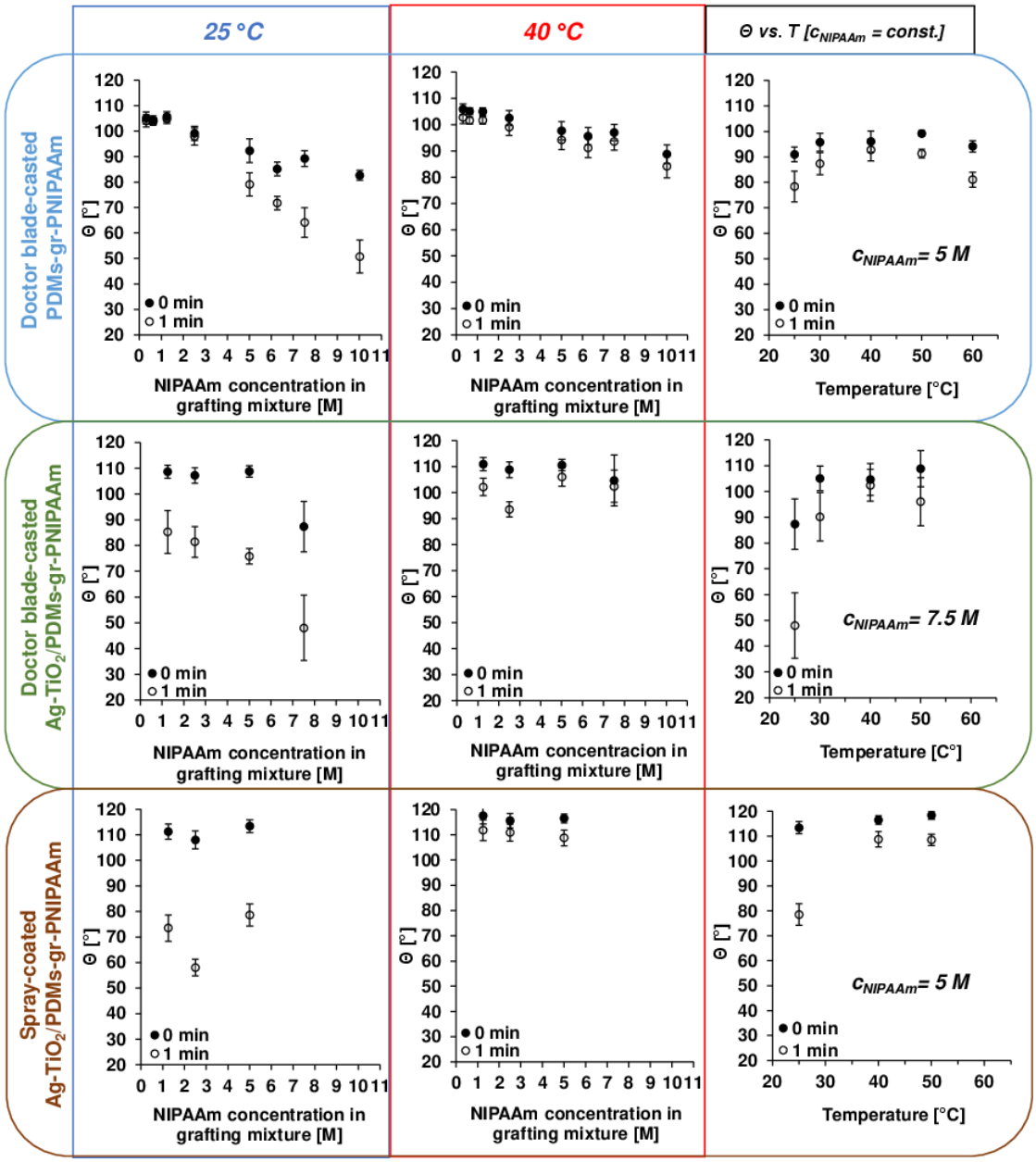

Figure 42. Θ values of doctor blade-casted and spray-coated PDMS-gr-pNIPAAm layers and Θ-s of spray-coated Ag-TiO_2/PDMS-gr-pNIPAAm layers (4.3 wt% INI) as a function of NIPAAm concentration in the grafting mixture, both at 25 and 40 °C with example Θ vs. T diagraphs at constant monomer concentration (right column) [185]

In the case of Ag-TiO_2/PDMS-gr-pNIPAAm films, the same wetting tendencies can be observed (**Fig. 42**), however the Θ values of the spray-coated layers in general, cover a broader range (even at lower pNIPAAm monomer concentrations) with the changing temperature: this can be explained by the increased surface roughness due to the addition of the photocatalyt nanoparticles [136]. As the addition of Ag-TiO_2 particles decreased the adhesion between the PDMS- films and the glass substrates, the maximum applicable NIPAAm monomer concentration was proven to be 7.5 M in the grafting mixtures: above this concentration, the polymer films detached from the substrates. This detachment can be attributed to the increase in surface waviness during grafting (it can be observed in **Fig. 40**), and the resulting decrease in the contact area between the films and the substrates.

This maximum acceptable concentration of NIPAAm was proven to be even lower (5 M) in the case of spray-coated Ag-TiO_2/PDMS-gr-pNIPAAm layers (**Fig. 42**) as the photocatalyst particles are more homogenously dispersed in these systems, which can result in a more significant decrease of film-substrate contact area and adhesion, which can lead to the detachment of the layers. This more homogenous distribution of the photocatalst particles is reflected in the results of Θ measurements: as it can be seen on Fig. 6, the Θ standard deviations (represented by the error bars) are smaller than in the case of doctor blade-casted films (**Fig. 42**). Moreover, the spray-coated films have higher achievable Θ values (even 117.5° at 0 min) over the LCST (**Fig. 42**), which also proves the roughness-enhanced hydrophobic character.

Besides the presented Θ values of different Ag-TiO_2/PDMS-gr-pNIPAAm (1.2 wt% INI) layers, the Θ values of 4.3 wt% INI-containing films were also measured and in their case the similar trends were observed. As the overall apparent mechanical stability of the 1.2 wt% INI layers was proven to be better than their 4.3 wt% INI counterparts', we decided to utilize these compositions in the following MB photodegradation tests, therefore the wetting properties of 4.3 wt% INI-containing systems were not studied and discussed in details.

5.5.3. Thermoresponsive photocatalytic performance Ag-TiO_2/PDMS-gr-pNIPAAm coatings

As the rate of heterogeneous photocatalytic reactions at the S/L-interface could be dependent on many factors, including the wetting character of the solid, the above-presented thermoresponsive wetting characteristics could - non-surprisingly - influence the photocatalytic performance of spray-coated Ag-TiO_2/PDMS-gr-pNIPAAm films, as well, which was proved by MB-photodegradation tests below (25 °C) and above (50 °C) the LCST of surface pNIPAAm.

The upper limit of the photocatalyst content of the examined composite layers (d= 19 mg/cm^2) was set to 15 wt% due to the extreme decline in mechanical durability and adhesive properties we experienced in the case of films with higher Ag-TiO_2-amounts. The PDMS : INI -ratio was also proven to be a critical when it comes to durability: as the incorporated nanoparticles and their aggregates also lower the crosslinking density, compositions with higher PDMS : INI-ratios are preferred in order to provide adequate mechanical integrity and adhesion to the supporting glass surface. Therefore, only spray-coated Ag-TiO_2/PDMS-gr-pNIPAAm (1.2 wt% INI; 5 M NIPAAm) layers were prepared for MB-photodegradation tests to avoid as much damage as possible during the experiments.

The recorded relative concentration (c/c_0) vs. illumination time curves can be seen on **Fig. 43.** As **Fig. 43** a shows, the photolysis of MB unsurprisingly has a higher reaction rate at 50 °C than at 25 °C. The thermosresponsive photocatalytic behaviour of Ag-TiO_2/PDMS-gr-pNIPAAm films is indicated by the differences between the MB-photodegradation efficiencies of the illuminated films and the photolysis (the direct photodegradation of MB) at different temperatures. **Fig. 43 c)** shows that the photodegradation efficiency of the layers is the same as the efficiency of the photolysis at 50 °C, while there is a 15.5 % difference between the efficiency of Ag-TiO_2-assisted photocatalytic degradation and the photolysis at 25 °C (**Fig. 43 c)**). This practically means the nullification of the photocatalytic effect of Ag-TiO_2 nanoparticles.

As it can be seen in **Fig. 43 a)**, the determined 15.5% difference in photodegradation efficiency can be considered as significant as the standard deviations of the relative concentrations (represented by the error bars), determined during 3 parallel measurements for each sample and temperature do not overlap.

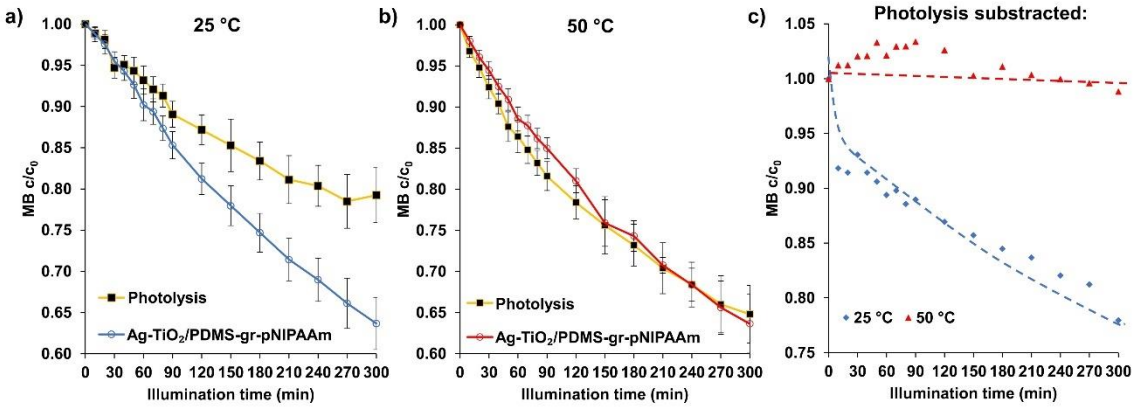

Figure 43. Photodegradation of MB on the S/L-interface upon Ag-TiO_2/PDMS-gr-pNIPAAm (1.2 wt% INI; 5 M NIPAAm) composite surface under blue LED illumination (λ_{max}= 405 nm) at 25 **a)**, 50 °C **b)** and at both temperatures after the substraction of the photolized concentration (MB c_0= 2 mg/l = 6.25 mM) **c)** The corresponding curves for MB photolysis are also presented [185]

According to an example for thermoresponsive photocatalytic particles from the literature, the nullification of photoreactivity can be explained by the hindered diffusion of the water-soluble dye molecules to the photocatalyst surface as the covering pNIPAAm-chains collapse and block the surface at temperatures over the LCST [126]. This proposed mechanism is depicted in **Fig. 44.** However, it is also important to note, that in similar photoreactive coatings the surface of photocatalyst particles is mostly covered in the matrix material [179] (also depicted in **Fig. 44**), which may photodegrade over time, resulting in a gradually increasing photodegradation efficiency towards the model pollutants as the photocatalyst particles become more exposed to incident light.

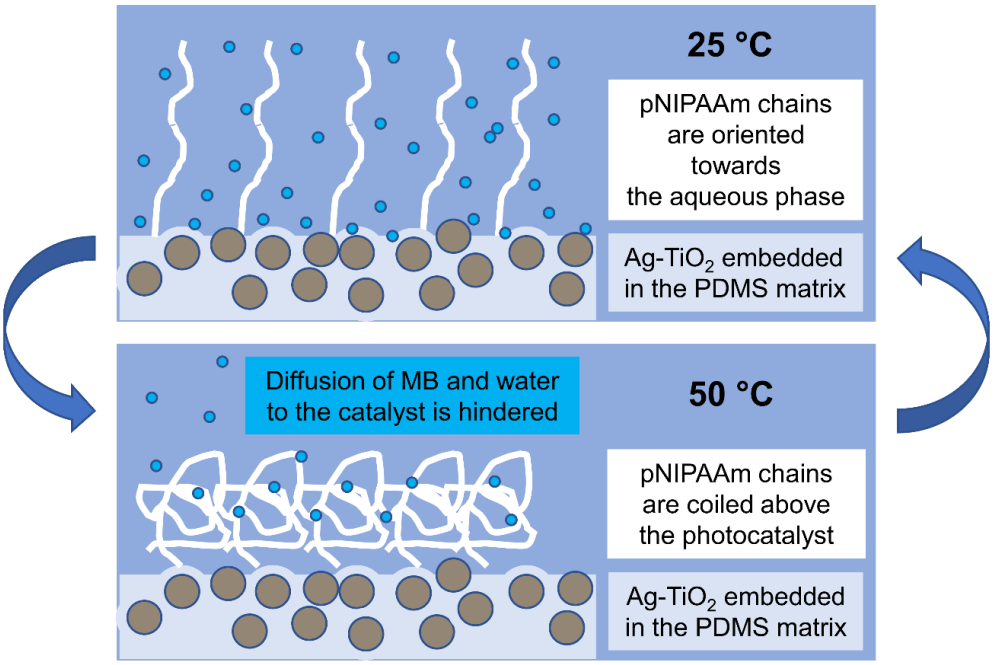

Figure 44. Proposed behaviour of the $AgTiO_2$/PDMS-gr-pNIPAAm composite surfaces in aqueous MB-solutions. The figure also represents the partial coverage of photocatalyst particle surfaces by the matrix material [185]

To support the obtained contact angle and photodegradation efficiency data, the γ_{tot} of the examined composites was also determined. As **Fig. 9 a)** shows, the advancing (Θ_{adv}) and receding (Θ_{rec}) contact angles at different temperatures do not differ significantly in the case of Ag-TiO_2/PDMS-co-INI (**Fig. 45 a)**), however, the dynamic Θs on Ag-TiO_2/PDMS-gr-pNIPAAm (**Fig. 45 b)**) increase as the temperature is elevated from 25 to 50 °C. The calculated (γ_s^{tot}) values are in good accordance with the wetting and photocatalytic experiments: while the γ_s^{tot} of Ag-TiO_2/PDMS-co-INI shows a slight decrease upon temperature-increase (from 7.54±0.42 to 4.71±0.47 mJ/m^2), this decrease is more emphasized in the case of Ag-TiO_2/PDMS-gr-PNIPAAm (from 42.12±5.75 to 8.22±1.25 mJ/m^2) (**Fig. 45 c)**). This surface free energy difference can also be the reason behind the different photodegradation efficiencies, as higher energy surfaces promote wetting and the adsoportion of photocatalytic substrates, in general.

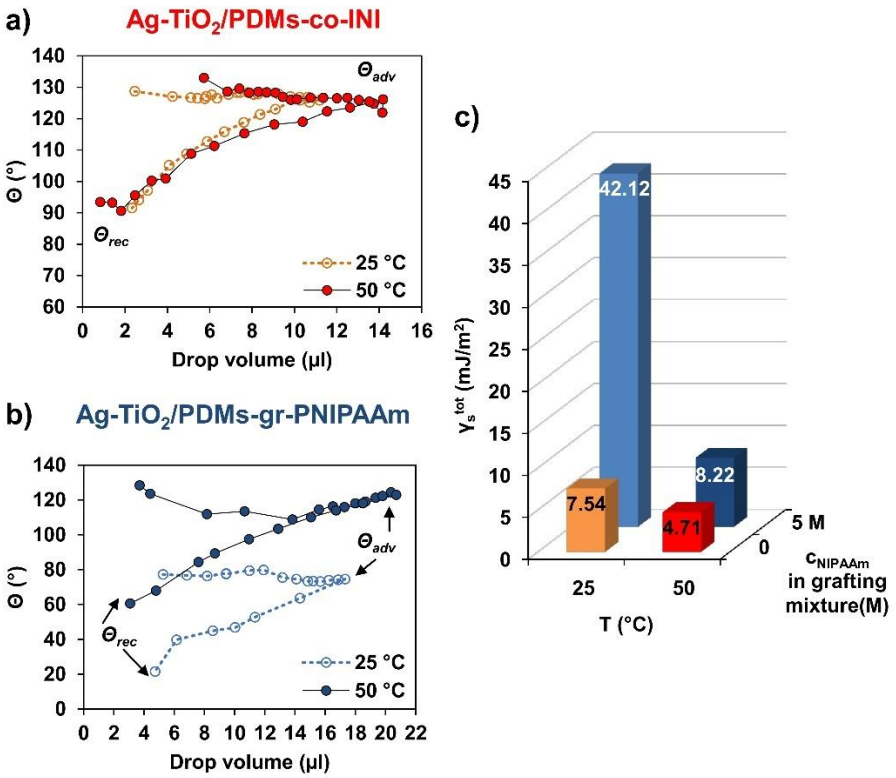

Figure 45. Θ values as a function of drop volume on Ag-TiO_2/PDMS-co-INI and **a)** on Ag-TiO_2/PDMS-gr-pNIPAAm (5 M NIPAAm) layers at 25 and 50 °C **b)** and the γ_s^{tot} values as functions of temperature and the grafting NIPAAm concentration (0 M for Ag-TiO_2/PDMS-co-INI) **c)** [185]

On the other hand, the observed photogedradation efficiencies may also be influenced by the temperature-dependent UV-VIS absorbance and thermal degradation of the MB solutions [192,193]. To examine this possibility, the UV-VIS spectra of the dye solutions were measured at both 25 and 50 °C and after 5 hours of 50 °C heat treatment. As **Fig. A9 a)** shows, the relative intensities of absorption peaks were barely influenced by the temperature in the 25-50 °C-range, however, a minor increase in the absorption around λ= 405 nm was observed **Fig. A9 b)**, which may contribute to the higher rate of direct MB-photolysis at 50 °C (**Fig. 43**). As the spectrum of the MB solution did not show changes either after the 5 h 50 °C treatment (**Fig. A9**), the thermal degradation during the photocatalytic experiments can be considered negligible.

5.6. Self-healing ability and photoreactivity - characterization of Ag-TiO_2/PDMS oleogel composite coatings

Due to their porosity and roughness, superhydrophobic surfaces are generally vulnerable [194]. The mechanical wear of superhydrophobic materials may lead to increased water-sticking (increasingly hydrophilic character) [195]. To overcome this limitation of their applicability, one can improve mechanical resistance by choosing appropriate materials [179] or by elaborating a self-healing character, like the one we can observe in the case of lotus leaf [196] (**Fig. 46**). To achieve this, the moisture-mediated hydrolysis-condensation polymerization reaction of dodecyl-trichlorosilane ($DDSiCl_3$) was selected, while the $DDSiCl_3$ was initially dispersed in a silicone oil-infused PDMS oleogel matrix (20 : 70 :100 = $DDSiCl_3$: silicone oil : PDMS; volumetric ratio). After the surface migration of these silane molecules, they undergo hydrolysis by the ambient moisture and condensation-driven self-assembly to produce a hydrophobic surfacial siloxane layer [197]. During my work, a soft, hydrophobic oleogel, consisting of 52.6 wt.% PDMS and 36.8 wt.% low-viscosity silicon oil (50 cP) was chosen to allow the rapid dissufion of $DDSiCl_3$ from the bulk gel to the gel/air-interface.

As **Fig. 46** shows, rough siloxane layers could form on the surface of bulk oleogel samples, even after two times complete mechanical removal of the previous layer. This regenerative behaviour is similar to the one of the lotus leaves, that can regrow their protrusions after their mechanical removal.

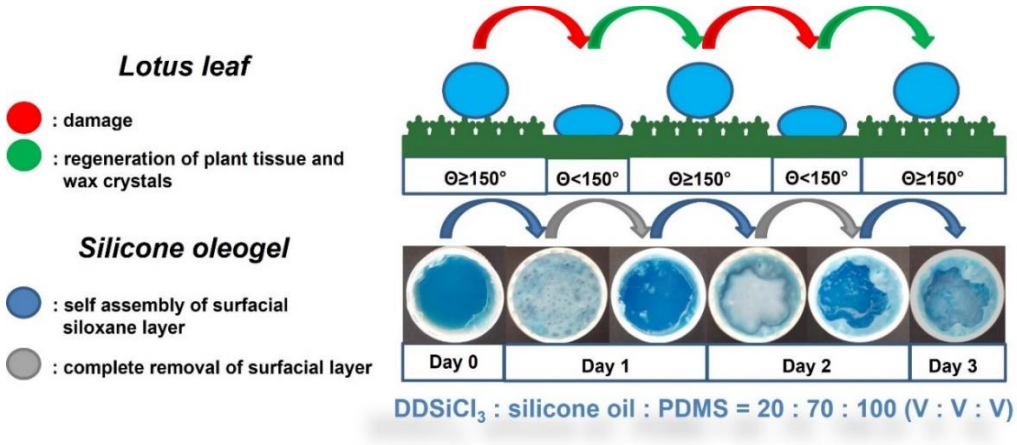

Figure 46. Self-healing of the lotus leaf (top) and the bulk $DDSiCl_3$-infused PDMS oleogel (bottom) [85]

As the initial soft oleogel was blue due to the dye-content of the PDMS, and the formed silicone layer was white, the formation of the upper layer was easy-to-follow, applying DR spectroscopy. **Fig. 47 a)** shows the recorded spectra, while **Fig. 47 b)** displays the extracted absorbance values (at λ=700 nm) as a function of time. The results revealed that the formed brighter silicone layer evolved relatively quickly, as after about 1.5 h, the slope of the A vs. t curve increased (from -0.136 to -0.023 h^{-1}), indicating a nearly steady state condition.

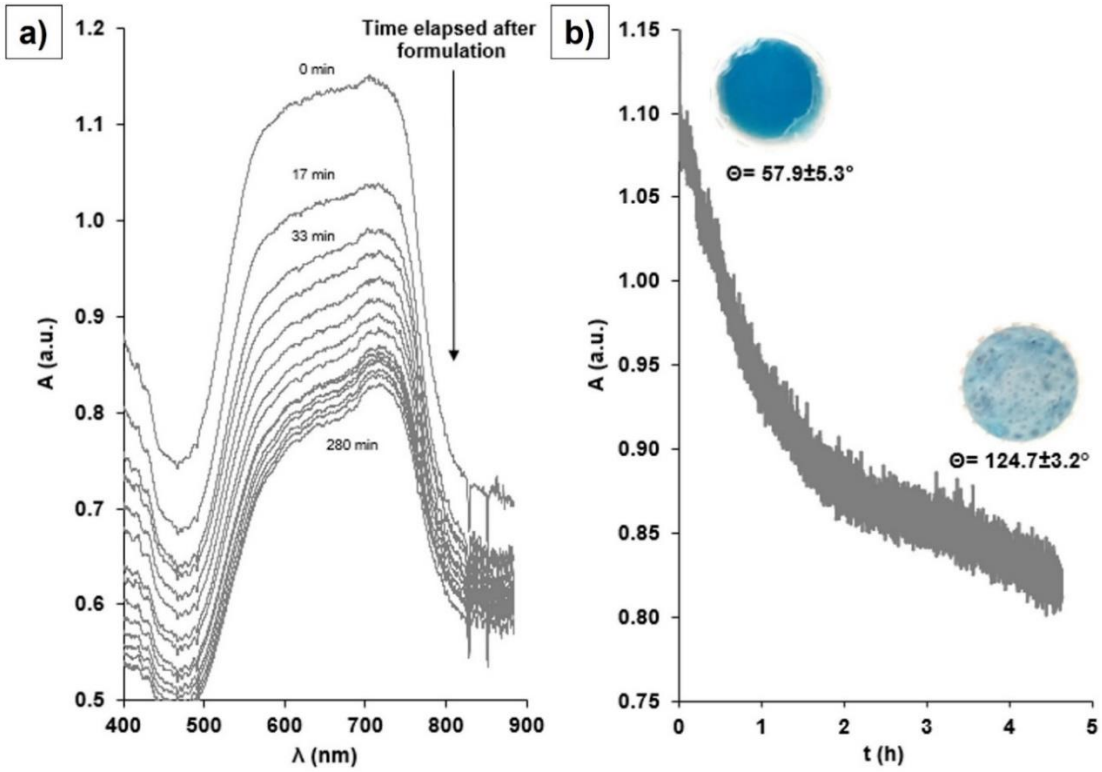

Figure 47. UV-VIS DR spectra of a $DDSiCl_3$-infused PDMS oleogel, recorded after certain time intervals following the gel formulation **a)** and the recorded absorbances at λ=700 nm with the images and Θ values of the initial formulated gel and the final product **b)** [85]

The surface morphology of the synthesized samples with- and without the self-assembled siloxane protrusions was also studied. **Fig. 48** shows the surface prophiles of a cured PDMS oleogel and the $DDSiCl_3$-infused oleogel after the formation of rough surficial layer (oleogel with self- assembled siloxane layer). While the self-assembled siloxane layer was micro-rough (R_q=0.4±0.1 μm) with a Θ value of 124.7°±3.2°, the Θ of the smooth (R_q≈0 μm) PDMS oleogel was only 57.9°±5.3°, indicating the more

hydrophobic nature of the formed siloxane layer. To achieve hierarchical roughness and superhydrophobic character, the oleogels were infused with 25 wt.% Ag-TiO_2. (Ag-TiO_2/PDMS oleogel), which further increased R_q to 13.8±1.4 μm and Θ to 151.6°±1.9°, achieving superhydrophobic character. The above discussed surface textures are also visible in the SEM images of **Fig. 48**.

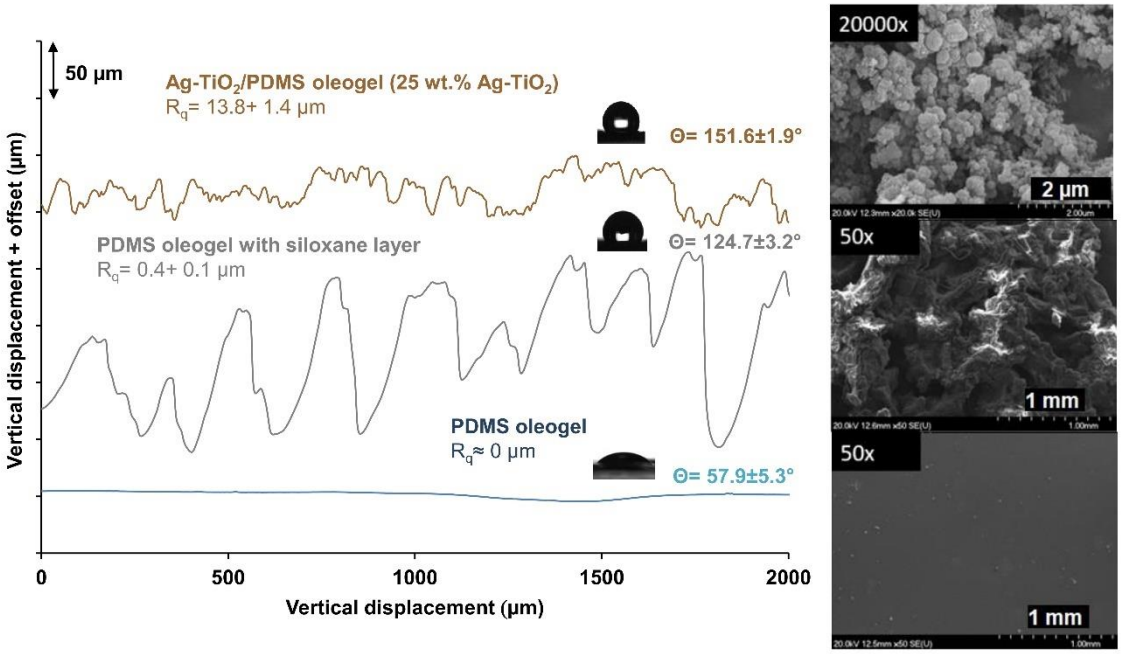

Figure 48. Respective profilometric curves, contact angles and SEM-images of the initial oleogel, the oleogel with siloxane layer and the 25 wt.% Ag-TiO_2-loaded oleogel composite [85]

The photocatalytic properties of the self-healing Ag-TiO_2/PDMS oleogel were also studied at the S/G-interface. As **Fig. 49** shows, Ag-TiO_2/PDMS oleogel (oleogel with 25 wt.% Ag-TiO_2) decomposed EtOH with ~50% efficiency, compared with the (k'=0.0112 min^{-1}) pure Ag-TiO_2 coating (k'=0.0495 min^{-1}) after 90 min irradiation. This clearly indicated the photocatalytic activity of the coating besides the above presented superhydrophobic and self-healing character. However, at Ag-TiO_2 loadings higher than 25 wt.% the mechanical integrity of the composites was very low, rendering them unable be used as coating materials due to the aggregation Ag-TiO_2 particles and the increasingly viscous character.

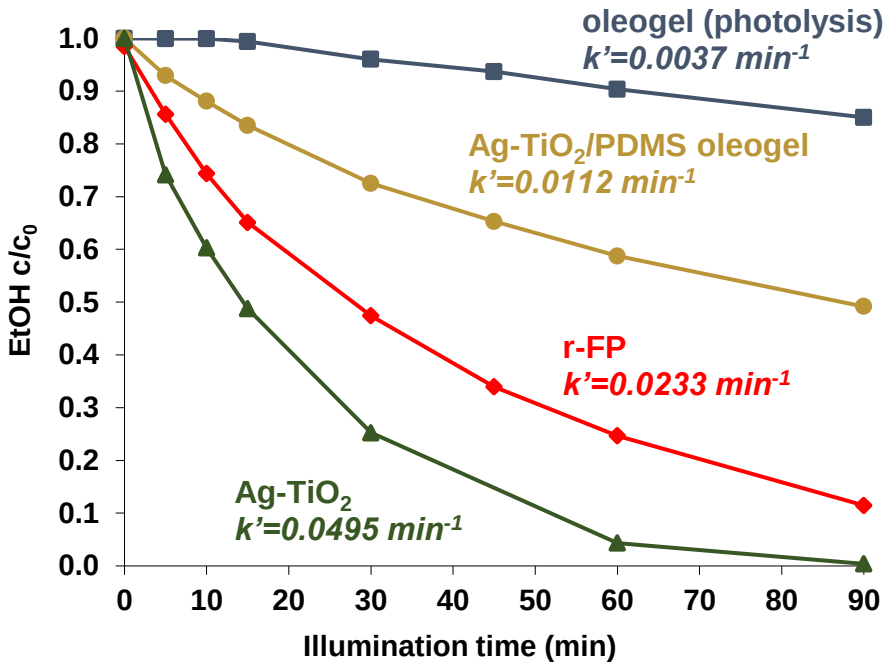

Figure 49. EtOH (g) (c_0=0.36 mM) photodegradation on Ag-TiO_2/polymer composites (blue LED light; λ_{max}=405 nm) as the function of illumination time. Besides the photodegradation curves of the Ag-TiO_2/PDMS oleogel samples (25 wt.% Ag-TiO_2), the degradation curves of r-FP, pure oleogel and Ag-TiO_2 layers are also displayed in comparison [85]

6. Summary

Nowadays, photoreactive interfaces and surfaces with extreme and/or tunable wettability are of high interest. During my doctoral work, I addressed the need for both functionalities by preparing various composites on the basis of visible light-active plasmonic Ag-TiO_2 photocatalyst nanoparticles, polyacrylates and PDMS.

At first, I presented that the wetting properties (Θ= 105.0°) of the smooth (R_q=3.7±0.9 μm), low energy (γ_s^{tot}=19.8±5.2 mJ/m^2) FP fluoropolymer coating could be increased by the addition of Ag-TiO_2. The coatings with different Ag-TiO_2/FP-ratio showed composition- and therefore roughness-dependent (R_q=3.7±0.9-15.2±1.2 μm) wettability, ranging from superhydrophilic- (pure photocatalyst; Θ=0°) to superhydrophobic (80 wt.% photocatalyst; Θ=150.9°) (γ_s^{tot}=6.5-71.9 mJ/m^2) character. The extreme wetting properties were the results of the hierarchical micro- and nano-roughness. The also highly porous (74.8 %) composites exerted visible light photoreactivity at the S/G interface: based on EtOH (g) photodegradation tests (blue LED; λ_{max}=405 nm), higher Ag-TiO_2 loadings resulted in higher decomposition rates (from k'=0.0034 min^{-1} to k'=0.0495 min^{-1}). The superhydrophobic, 80 wt.% Ag-TiO_2-containing surface adsorbed and photodegraded the apolar Sudan IV dye at the S/L-interface (0.92 mg dye/cm^2, 90 min irradiation time), while the non-wetting nature of aqueous MB solution hindered the photooxidation of this hydrophilic dye.

Besides keeping the 80 wt.% photocatalyst-loading, required for achieving the extreme, superhydrophobic wetting behaviour, in the followings, I investigated the effect of different matrix compositions on wettability and photoreactivity. As an additional, hydrophilic polyacrylate matrix component, pHEA was selected.

The wetting character of the smooth pHEA (Θ=27.4°, γ_s^{tot}=55.7±2.3 mJ/m^2) and low energy FP (Θ=105.0°, γ=γ_s^{tot}=19.8±5.2 mJ/m^2) coatings got highlighted, as their surface roughness was enhanced by the photocatalyst particles. In the case of the rough r-pHEA and r-FP coatings, superhydrophilic (Θ=0°, γ_s^{tot}≥72.1±0.2 mJ/m^2) and superhydrophobic characters were experienced, respectively, while the wettability of the composites was proven to be tunable by adjusting the matrix composition. The photocatalytic properties in these cases were also composition- and wettability-dependent: the determined EtOH(g) degradation efficiencies varied between 51.3% and 88.3% (0 and 20 wt.% overall FP content). At the S/L interface, the photodegradation

efficiency was also dependent on the polarity of the test dyes and their solvents: while the superhydrophobic r-FP composite photodegraded the hydrophobic Sudan IV dye (dissolved in abs. EtOH), the r-pHEA surface could photodegrade the MB in aqueous medium. The above-all advantage of these surfaces over previous photoreactive composite coatings is the matrix composition-dependent wettability, which could be interesting in water treatment scenarios, where the polarity of the pollutants varies on a broad scale.

As the popularity of microfluidic and liquid micro-manipulation techniques shows an increasing trend, the need for the development new functional surfaces with stimulus-responsive wettability is also emerging. This need was addressed through the preparationof PDMS- and carbonyl Fe-based composite grass coatings with magnetoresponsive wetting and visible light-photoactivity were prepared, applying a magnetic field-assisted spray-coating self-assembly technique. The composites possessed variable Θ- and s.a. ranges, depending on both the external magnetic field- and the Ag-TiO_2 loading, which latter enhanced the surfaces with considerable roughness. The achievable wetting ranges (with or without external magnetic field) were found to be broadening (in a magnetic field, perpendicular to the surface: 55° <Θ<147.4° → 56.5°<Θ <163.6°) with the increasing Ag-TiO_2 loading (0-16.7 wt.%).

The presence of Ag-TiO_2 also led to visible light-photoreactivity: during blue LED-illumination (λ_{max}=405 nm), the composites could decrease the MB-concentration (c_0=2 mg/l) at S/L-interface, at rates, depending on the external magnetic field. Without a magnet, the apparently hydrophilic (Θ=56.5±0.5°), randomly oriented grass decreased the initial MB concentration by 42.1±3.5% in 300 min, however, the degradation efficiency of the superhydrophobic (Θ=163.6±2.9°), vertically stiffened grass (in 0.30 T magnetic field) was only 22.4±3.3%. Moreover, utilizing the real-time tunable wettability the magnetic composites could be used for lossless droplet transportation, which prospects their application as multifunctional tools in liquid manipulation scenarios.

Besides magnetoresponsivity, the thermoresponsive property of pNIPAAm was also utilized: the prepared multifunctional Ag-TiO_2/PDMS-gr-pNIPAAm coatings were proven to be thermoresponsive (temperature: 25-50 °C) with real-time tunable wetting properties (Θ: 50.7°-108.9°) and tunable visible light-photoreactivity (blue LED-light;

λ=405 nm) at the S/L-interface during MB degradation experiments. The wettability also turned out to be dependent on the concentration of the grafting NIPAAm-monomer.

These prepared magneto- and thermoresponsive systems are among the first examples of marcoscopic composite surfaces with both stimulus-responsive wetting and photoreactivity. For example, these combined features may have promising future in photocatalysis-assisted membrane filtration or decontamination scenarios, where the well wetted state provides increased decomposition rates, while the liobhobic state may provide antifouling nature and self-cleaning character, allowing easier cleanup and increased reusability.

Finally, the outer surface of PDMS-oleogels was also rendered self-healing and hydrophobic, utilizing the humidity-mediated polymerization of $DDSiCl_3$ to form micro-roughened surficial layers. This mechanism could provide quick superhydrophobic recovery under ambient conditions, and therefore long-term durability to artificial superhydrophobic coating materials. The missing nano-roughness, and the superhydrophobic character was also achieved with the help of Ag-TiO_2, rendering the composites photoreactive, as well.

7. Összefoglalás

A fotoreaktív-, valamint az extrém és/vagy szabályozható nedvesedésű felületeket napjainkban fokozódó érdeklődés övezi. Doktori munkám során látható fényben aktív, plazmonikus Ag-TiO_2 fotokatalizátor nanorészecskékből, poliakrilátokból és PDMS-ből kiindulva hoztam létre egyszerre mindkét említett funkcióval rendelkező kompozit felületeket.

Elsőként bemutattam, hogy a vizsgált perfluorozott poliakrilátból (FP) készült hidrofób (Θ=105,0°; γ_s^{tot}=19,8±5,2 mJ/m^2), sík (R_q=3,7±0,9 μm) filmek nedvesedési karaktere Ag-TiO_2-vel történő érdesítéssel fokozható. A kapott bevonatok Ag-TiO_2/FP-arány függvényében változó felületi érdességgel és az érdességtől (R_q=3,7±0,9-15,2±1,2 μm) függő nedvesedéssel rendelkeztek a szuperhidrofiltől (tiszta fotokatalizátor; Θ=0°) a szuperhidrofóbig (80 m/m% fotokatalizátor; Θ=150,9°) terjedő Θ-tartományban (γ_s^{tot}=6,5-71,9 mJ/m^2).

Az extrém nedvesedési karakter megjelenése a porlasztásos úton kialakított filmek hierarchikus felületi mikro-, illletve nanoérdesség következménye. A nagy porozitású (74,8 %) bevonatok a Sz/G-határfelületen látható fény-fotoreaktivitással is rendelkeztek: kék fényű LED-lámpával (λ_{max}=405 nm) végzett EtOH(g)-fotodegradációs tesztek során a bevonatok fotoreaktivitása az Ag-TiO_2-tartalom növelésével fokozhatónak bizonyult (k'=0.0034 min^{-1}-től k'=0.0495 min^{-1}-ig terjedő tartományban).

Sz/F-határfelületen végzett tesztek során az apoláris Szudán IV színezék jól adszorbeálódott és teljes mértékben fotodegradálódott a 80 m/m% Ag-TiO_2-t tartalmazó szuperhidrofób bevonaton (0,92 mg színezék/ cm^2, 90 perces megvilágítás), míg a vizes oldat formájában felületre vitt hidrofil metilénkék (MK) adszorpciója és fotodegradációja ezen a felületen már nem volt kivitelezhető.

Az extrém, szuperhidrofób nedvesedési karakter eléréséhez szükséges 80 m/m% fotokatalizátor-tartalom megtartása mellett a továbbiakban a kompozit mátrix összetételének változtatásának nedvesedésre és fotoreaktivitásra gyakorolt hatása került minősítésre, pHEA, mint hidrofil mátrixalkotó poliakrilát felhasználásával.

Mind a nagy felületi szabadenergiájú, hidrofil sík pHEA- (Θ=27,4°, γ_s^{tot}=55,7±2.3 mJ/m^2), mind pedig a hidrofób sík FP (Θ=105,0°, γ=γ_s^{tot}=19,8±5,2 mJ/m^2) polimerfilm nedvesedési karaktere is hangsúlyosabbá vált a fotokatalizátorral való érdesítés

hatására, így a kapott r-pHEA és r-FP filmek szuperhidrofil- (Θ=0°, $\gamma \geq \gamma_s^{tot}$=72,1±0,2 mJ/m^2), valamint szuperhidrofób karakterre tettek szert, emellett a matrix összetételének változtatásával a nedvesedés hangolhatónak bizonyult.

E bevonatok fotokatalitikus sajátságai szintén összetétel- és nedvesedésfüggőnek adódtak: a meghatározott EtOH(g) fotodegradációs hatásfokok 51,3-88.3%-nak adódtak (0 és 20 m/m% FP-tartalom). A Sz/F-határfelületen tapasztalt katalitikus hatékonyság függött a modell szennyezők és az oldószer polaritásától: míg a szuperhidrofób r-FP kompozit a hidrofób Szudán IV-et (absz. EtOH-s oldatban) fotodegradálta nagy hatásfokkal, addig az r-pHEA a vizes közegben oldott metilénkék bontása során bizonyult hatékonynak. A bevonatok összetételfüggő nedvesedésének és fotoreaktivitásának egy potenciális felhasználási területe lehet a vízkezelés, ahol a széles skálán mozgó polaritású szennyezők lebontásában nyújthatnak megoldást.

A mikrofluidika és a folyadékmanipuláció térnyerésének köszönhetően egyre nagyobb igény mutatkozik új, stimulus-reszponzív nedvesedésű funkcionális felületek kialakítása iránt. Ennek fényében olyan karbonil-Fe és PDMS-alapú kompozitokat hoztam lére mágneses térben történő porlasztásos filképzéssel, melyek mágneses térrel szabályozható nedvesedéssel és látható fény-fotoreaktivitással rendelkeztek. A bevonatok nedvesedési- és szakadási szögei a külső mágneses térrel és fotokatalizátor-tartalommal szabályozhatónak bizonyultak: az Ag-TiO_2-tartalom növelése (0-16,7 wt.%). felületérdesítő hatású, ennél fogva pedig az elérhető nedvesedési tartomány kiszélesedését eredményezte (felületre merőleges mágneses térben: 55° <Θ<147,4° → 56,5°<Θ <163,6°)

A fotokatalizátor-tartalom a bevonatoknak látható fény-fotoreaktivitást is kölcsönzött: metilénkék (c_0=2 mg/l) Sz/F-határfelüelten végrehajtot fotodegradációja (kék fényű LED-lámpa; λ_{max}=405 nm; t=300 min) során mágneses tér jelenléte nélkül a jól nedvesedő (Θ=56,5±0,5°), véletlenszerű orientációjú mágneses fűvel 42,1±3,5%, míg a mágneses térrel (0,30 T) kimerevített, rosszul nedvesedő (Θ=163,6±2,9°) fűvel alacsonyabb, 22,4±3,3%-os degradációs hatásfokot értem el.

A kompozitok valós időben szabályozható nedvesedésüknek köszönhetően veszteségmentes folyadékcsepp-szállításra is alkalmasak, így akár multifunkciós folyadékmanipulációs eszközökként is felhasználhatók.

A magnetoreszponzív viselkedés mellett termoreszponzív pNIPAAm felhasználásával is kialakítottam kompozit bevonatokat: az Ag-TiO_2/PDMS-gr-

pNIPAAm filmek termoreszponzív (25-50 °C), ojtási NIPAAm-monomerkoncentrációtól is függő nedvesedési karakterrel (Θ: 50,7°-108,9°) és látható fény-fotoreaktivitással rendelkeztek (kék LED, λ_{max}=405 nm; metilénkék fotodegradáció Sz/F-határfelületen).

Mindemellett, a kialakított magneto-és termoreszponzív rendszerek az irodalomban bemutatott stimulus-reszponzív nedvesedéssel és fotoreaktivitással rendelkező makroszkópikus kompozit felületek első képviselői közt tarthatók számon. E tulajdonságok kombinációja felhasználható lehet például öntisztuló felületek és membránok alkalmazása során, ahol a jól nedvesedő állapot megnövelt fotodegradációs hatasfokot, míg a liofób állapot öntisztuló jelleget, ezáltal pedig nagyobb fokú tisztíthatóságot és újrafelhasználhatóságot biztosíthat.

Végezetül, bemutatásra került az is, hogy a PDMS-oleogél alapú bevonatok felületén, $DDSiCl_3$ páratartalom hatására végbemenő polimerizációja révén mikroérdes, öngyógyuló hidrofób réteg alakítható ki. A szuperhidrofób karakter kialakításához hiányzó nanoérdesség Ag-TiO_2 nanorészecskék hozzáadása révén került kialakításra, így a kapott kompozit rétegek fotokatalitikus tulajdonsággal is rendelkeztek.

8. References

[1] Chang H, Liu B, Zhang Z, Pawar R, Yan Z, Crittenden JC, et al. Environ Sci Technol 2021;55:1395–1418.
[2] Kaplan WD, Chatain D, Wynblatt P, Carter WC. J Mater Sci 2013;48:5681–5717.
[3] Gharabaghi M, Aghazadeh S. Curr Opin Colloid Interface Sci 2014;19:266–282.
[4] Lu G, Wang X-D, Duan Y-Y. Adv Colloid Interface Sci 2016;236:43–62.
[5] Li S, Huang J, Chen Z, Chen G, Lai Y. J Mater Chem A 2017;5:31–55.
[6] Wang Z, Elimelech M, Lin S. Environ Sci Technol 2016;50:2132–2150.
[7] Goh PS, Naim R, Rahbari-Sisakht M, Ismail AF. Sep Purif Technol 2019;227:115721.
[8] Wang J, Wang H, Xie J, Yang A, Pei A, Wu C-L, et al. Energy Storage Mater 2018;14:345–350.
[9] Shin S, Seo J, Han H, Kang S, Kim H, Lee T. Materials (Basel) 2016;9:116.
[10] Khan MF, Luong N, Kurian J, Brook MA. Chem Commun 2017;53:3050–3053.
[11] Mérai L, Deák Á, Dékány I, Janovák L. Adv Colloid Interface Sci 2022;303:102657.
[12] Drelich J. Surf Innov 2013;1:248–254. https://doi.org/10.1680/si.13.00010
[13] Schuster JM, Schvezov CE, Rosenberger MR. Procedia Mater Sci 2015;8:742–51.
[14] Albert E, Tegze B, Hajnal Z, Zámbó D, Szekrényes DP, Deák A, et al. ACS Omega 2019;4:18465–18471.
[15] Eral HB, 't Mannetje DJCM, Oh JM. Colloid Polym Sci 2013;291:247–260.
[16] Jafari M, Jung J. Sustainability 2017;9:2352.
[17] Aliabadi M, Konrad W, Stegmaier T, Arnim V, Kaya C, Liu Y, et al. J Appl Polym Sci 2021;138.
[18] Gao L, McCarthy TJ. Langmuir 2006;22:6234–6237.
[19] Volpe C Della, Siboni S. Surf Innov 2018;6:120–132.
[20] Hasegawa M, Endo H, Morita K, Sakaue H, Kimura S. Aerospace 2021;8:219.
[21] Gonzales J, Kurihara D, Maeda T, Yamazaki M, Saruhashi T, Kimura S, et al. Materials (Basel) 2019;12:2758.
[22] Gong Y, Xu J, Buchanan RC. Phys Sci Rev 2018;3.
[23] Jothi Prakash CG, Prasanth R. J Mater Sci 2021;56:108–135.
[24] Li C, Li M, Ni Z, Guan Q, Blackman BRK, Saiz E. J R Soc Interface 2021;18:20210162.
[25] Madeira DMF, Vieira O, Pinheiro LA, de Melo Carvalho B. Int J Chem Eng 2018;2018:1–7.
[26] Zisman WA. Adv Chem 1964;43:1–51.
[27] Annamalai M, Gopinadhan K, Han SA, Saha S, Park HJ, Cho EB, et al. Nanoscale 2016;8:5764–5770.
[28] Wu S. J Polym Sci Part C Polym Symp 2007;34:19–30.
[29] Chibowski E. Adv Colloid Interface Sci 2003;103:149–172.
[30] Rupp F, Gittens RA, Scheideler L, Marmur A, Boyan BD, Schwartz Z, et al. Acta Biomater 2014;10:2894–2906.
[31] Berry M V. Phys Educ 1971;6:001.
[32] Pirard R, Pirard J-P. Mercury porosimetry applied to precipitated silica., in: Stud Surf Sci Catal 2000;128:603–611.
[33] Gong X, Wang B, Li L. ACS Omega 2018;3:16398–16402.
[34] Guba S, Horváth B, Szalai I. J Magn Magn Mater 2020;498:166181.
[35] De S, Malik S, Ghosh A, Saha R, Saha B. RSC Adv 2015;5:65757–65767.
[36] Yao Y, Wei M, Kang W. Adv Colloid Interface Sci 2021;294:102477.
[37] Liu S, Liu J, Liu G, Liu Y, Zhong H. Appl Surf Sci 2020;505:144467.
[38] Wang X, Yuan S, Jiang B. J Chem 2019;2019:1–9.
[39] Kronberg B, Holmberg K, Lindman B. Surfactant Adsorption at Solid Surfaces. Surf. Chem. Surfactants Polym., Chichester, UK: John Wiley & Sons, Ltd; 2014, p. 153–173.
[40] Al-Wahaibi Y, Al-Hashmi A-A, Joshi S, Mosavat N, Rudyk S, Al-Khamisi S, et al. Mechanistic Study of Surfactant/Polymer Adsorption and Its Effect on Surface Morphology and Wettability. Day 2 Wed, April 05, 2017, SPE; 2017. https://doi.org/10.2118/185327-MS
[41] Wang R, Hashimoto K, Fujishima A, Chikuni M, Kojima E, Kitamura A, et al. Nature 1997;388:431–432.
[42] Hongru A, Xiangqin L, Shuyan S, Ying Z, Tianqing L. RSC Adv 2017;7:7052–9.
[43] McHale G. Langmuir 2007;23:8200–8205.
[44] Bhushan B, Nosonovsky M. Philos Trans R Soc A Math Phys Eng Sci 2010;368:4713–4728.
[45] Bormashenko E. Low Temp Phys 2016;42:622–35.
[46] Cao F, Guan Z, Li D. J Wuhan Univ Technol Sci Ed 2008;23:513–517.

[47] Giacomello A, Meloni S, Chinappi M, Casciola CM. Langmuir 2012;28:10764–10772.
[48] Sarkar A, Kietzig A-M. Soft Matter 2015;11:1998–2007.
[49] Liu S, Zhou Z, Zhou S, Cui J, Wang Q, Zhang Y, et al. J Taiwan Inst Chem Eng 2019;95:300–307.
[50] Anis SF, Lalia BS, Hashaikeh R, Hilal N. Sep Purif Technol 2021;275:119241.
[51] Li C, Zhang J, Han J, Yao B. Sci Rep 2021;11:459.
[52] De Nicola F, Viola I, Tenuzzo LD, Rasch F, Lohe MR, Nia AS, et al. Sci Rep 2020;10:1916.
[53] Lopes DM, Ramos SMM, de Oliveira LR, Mombach JCM. RSC Adv 2013;3:24530.
[54] Garg P, Ghatmale P, Tarwadi K, Chavan S. Biomimetics 2017;2:7.
[55] Zhang Y, Wu H, Yu X, Chen F, Wu J. J Bionic Eng 2012;9:84–90.
[56] Li J, Wang G, Meng Q, Ding C, Jiang H, Fang Y. Appl Surf Sci 2014;315:407–414.
[57] Xu Q, Zhang W, Dong C, Sreeprasad TS, Xia Z. J R Soc Interface 2016;13:20160300.
[58] Riedel J, Vucko MJ, Blomberg SP, Schwarzkopf L. Ecol Evol 2020;10:4640–4651.
[59] Stark AY, Mitchell CT. Integr Comp Biol 2019;59:214–226.
[60] Li S, Huang J, Chen Z, Chen G, Lai Y. J Mater Chem A 2017;5:31–55.
[61] Shen Y, Wu Z, Tao J, Jia Z, Chen H, Liu S, et al. ACS Appl Mater Interfaces 2020;12:25484–93.
[62] Meena MK, Sinhamahapatra A, Kumar A. Colloid Polym Sci 2019;297:1499–1505.
[63] Janovák L, Dernovics Á, Mérai L, Deák Á, Sebők D, Csapó E, et al. Chem Commun 2018;54:650–653.
[64] Wang H, Sun F, Wang C, Zhu Y, Wang H. Colloid Polym Sci 2016;294:303–309.
[65] Guo X-J, Xue C-H, Sathasivam S, Page K, He G, Guo J, et al. J Mater Chem A 2019;7:17604–17612.
[66] Li A, Wang G, Ma Y, Zhao C, Zhang F, He Q, et al. J Mater Res Technol 2021;11:135–143.
[67] Wang F, Lei S, Xu Y, Ou J. ChemPhysChem 2015;16:2237–2243.
[68] Wang G, Song D, Qiao Y, Cheng J, Liu H, Jiang J, et al. J Magnes Alloy 2021. https://doi.org/10.1016/j.jma.2021.08.002
[69] Qing Y, Long C, An K, Hu C, Liu C. J Colloid Interface Sci 2019;548:224–232.
[70] Liu Z, Pang X, Wang K, Lv X, Cui X. ACS Appl Mater Interfaces 2019;11:22809–22816.
[71] Dong Z, Vuckovac M, Cui W, Zhou Q, Ras RHA, Levkin PA. Adv Mater 2021;33:2106068.
[72] Wang C, Yao T, Wu J, Ma C, Fan Z, Wang Z, et al. ACS Appl Mater Interfaces 2009;1:2613–2617.
[73] Liu M, Li M-T, Xu S, Yang H, Sun H-B. Front Chem 2020;8:835
[74] Du K, Jiang Y, Liu Y, Wathuthanthri I, Choi C-H. Micromachines 2018;9:304.
[75] Li F, Yu Z, Shi H, Yang Q, Chen Q, Pan Y, et al. Chem Eng J 2017;322:33–45.
[76] Badica P, Batalu ND, Burdusel M, Grigoroscuta MA, Aldica G, Enculescu M, et al. Sci Rep 2021;11:9591.
[77] Kim J-H, Mirzaei A, Kim HW, Kim SS. Appl Surf Sci 2018;439:598–604.
[78] Marlena J, Tan JKS, Lin Z, Li DX, Zhao B, Leo HL, et al. NPG Asia Mater 2021;13:58.
[79] Gong D, Long J, Jiang D, Fan P, Zhang H, Li L, et al. ACS Appl Mater Interfaces 2016;8:17511–8.
[80] Wang X-Y, Zhang C, Sun S, Kalulu M, Chen L, Zhou X, et al. Colloids Surfaces A Physicochem Eng Asp 2019;578:123550.
[81] Ma J, Porath LE, Haque MF, Sett S, Rabbi KF, Nam S, et al. Nat Commun 2021;12:5210.
[82] Xiang S, Liu W. Adv Mater Interfaces 2021;8:2100247.
[83] Yuan G, Liu Y, Ngo C-V, Guo C. Opt Express 2020;28:35636.
[84] Shen Y, Wu Y, Shen Z, Chen H. Coatings 2018;8:144.
[85] Merai L, Varga N, Deák Á, Sebők D, Szenti I, Kukovecz Á, et al. Catal Today 2019;328:85–90.
[86] Tu K, Wang X, Kong L, Guan H. Mater Des 2018;140:30–36.
[87] Villegas M, Zhang Y, Abu Jarad N, Soleymani L, Didar TF. ACS Nano 2019;13:8517–8536.
[88] Wei C, Zhang G, Zhang Q, Zhan X, Chen F. ACS Appl Mater Interfaces 2016;8:34810–34819.
[89] Juuti P, Haapanen J, Stenroos C, Niemelä-Anttonen H, Harra J, Koivuluoto H, et al. Appl Phys Lett 2017;110:161603.
[90] Long Y, Yin X, Mu P, Wang Q, Hu J, Li J. Chem Eng J 2020;401:126137.
[91] Kim SJ, Kim HN, Lee SJ, Sung HJ. Phys Fluids 2020;32:091901.
[92] Rao Q, Lu Y, Song L, Hou Y, Zhan X, Zhang Q. ACS Appl Mater Interfaces 2021;13:40032–40041.
[93] Chang C-C, Wu C-J, Sheng Y-J, Tsao H-K. RSC Adv 2016;6:19214–19222.
[94] Armstrong S, McHale G, Ledesma-Aguilar R, Wells GG. Langmuir 2020;36:11332–11340.
[95] Mrinalini M, Prasanthkumar S. Chempluschem 2019;84:1103–1121.
[96] Bratek-Skicki A. Appl Surf Sci Adv 2021;4:100068.

[97] Brzezicki M. Sustainability 2021;13:9604.
[98] Zhang Y, Wang C, Zhao W, Li M, Wang X, Yang X, et al. Polymers (Basel) 2019;11:1869.
[99] Abdo GG, Zagho MM, Khalil A. Emergent Mater 2020;3:407–425.
[100] Jiang H, Ochoa M, Waimin JF, Rahimi R, Ziaie B. Lab Chip 2019;19:2265–2274.
[101] Zahn D, Weidner A, Saatchi K, Häfeli UO, Dutz S. Curr Dir Biomed Eng 2019;5:161–164.
[102] Seo J, Song M, Jeong J, Nam S, Heo I, Park S-Y, et al. ACS Appl Mater Interfaces 2016;8:23862–23867.
[103] Saitoh T, Suzuki Y, Hiraide M. Anal Sci 2002;18:203–205.
[104] Bakarich SE, Gorkin R, Panhuis M in het, Spinks GM. Macromol Rapid Commun 2015;36:1211–1217
[105] Wang Y, Song C, Yu X, Liu L, Han Y, Chen J, et al. Compos Sci Technol 2017;151:139–146.
[106] Fu Q, Rama Rao G V., Basame SB, Keller DJ, Artyushkova K, Fulghum JE, et al. J Am Chem Soc 2004;126:8904–8905.
[107] Zhang D, Cheng Z, Kang H, Yu J, Liu Y, Jiang L. Angew Chemie Int Ed 2018;57:3701–3705.
[108] Li C, Li M, Ni Z, Guan Q, Blackman BRK, Saiz E. J R Soc Interface 2021;18: 20210162.
[109] Yang X, Huang Y, Zhao Y, Zhang X, Wang J, Sann EE, et al. Front Chem 2019;7. https://doi.org/10.3389/fchem.2019.00826
[110] Etha SA, Desai PR, Sachar HS, Das S. Macromolecules 2021;54:584–596.
[111] Doberenz F, Zeng K, Willems C, Zhang K, Groth T. J Mater Chem B 2020;8:607–628.
[112] Kotsuchibashi Y. Polym J 2020;52:681–689.
[113] Zhang S, Wang J, Zhang X, Song W, Wang S. Sci China Mater 2019;62:597–603.
[114] Shivapooja P, Ista LK, Canavan HE, Lopez GP. Biointerphases 2012;7:32.
[115] Xiong X, Wu Z, Pan J, Xue L, Xu Y, Chen H. J Mater Chem B 2015;3:629–634.
[116] Spasojević M, Vorenkamp J, Jansen M, de Vos P, Schouten A. Materials (Basel) 2014;7:5305–5326.
[117] Kim YS, Kim MA, Lee C-M. Mater Technol 2019;34:639–644.
[118] Choe A, Yeom J, Shanker R, Kim MP, Kang S, Ko H. NPG Asia Mater 2018;10:912–922.
[119] Arotçaréna M, Heise B, Ishaya S, Laschewsky A. J Am Chem Soc 2002;124:3787–3793.
[120] Kawaguchi H. Gels 2020;6:26.
[121] Li M, Chen Z. J Polym Sci 2021;59:2230–2245.
[122] Sarwan T, Kumar P, Choonara YE, Pillay V. Front Mater 2020;7. https://doi.org/10.3389/fmats.2020.00073
[123] Yu W, Lou L-L, Li S, Ma T, Ouyang L, Feng L, et al. RSC Adv 2017;7:751–757.
[124] Zhang L, Zhang S, He B, Wu Z, Zhang Z. Zeitschrift Für Naturforsch B 2008;63:973–976.
[125] Lou L-L, Qu H, Yu W, Wang B, Ouyang L, Liu S, et al. ChemCatChem 2018;10:1166–1172.
[126] Jia H, Roa R, Angioletti-Uberti S, Henzler K, Ott A, Lin X, et al. J Mater Chem A 2016;4:9677–9684.
[127] Ma W, Wang H. Appl Mater Today 2019;15:263–266.
[128] Sedlacik M, Mrlik M, Babayan V, Pavlinek V. Compos Struct 2016;135:199–204.
[129] Tian D, Zhang N, Zheng X, Hou G, Tian Y, Du Y, et al. ACS Nano 2016;10:6220–6226.
[130] Lee S, Yim C, Kim W, Jeon S. ACS Appl Mater Interfaces 2015;7:19853–19856.
[131] Huang Y, Stogin BB, Sun N, Wang J, Yang S, Wong T. Adv Mater 2017;29:1604641.
[132] Sorokin V V., Sokolov BO, Stepanov G V., Kramarenko EY. J Magn Magn Mater 2018;459:268–271.
[133] Yang C, Wu L, Li G. ACS Appl Mater Interfaces 2018;10:20150–20158.
[134] Wang L, Zhao X, Zhang Y, Zhang W, Ren T, Chen Z, Wang F, Yang H. RSC Adv 2015;5:40437–40443
[135] Janovak L, Tallósy SP, Sztakó M, Deak A, Bitó T, Buzas N, et al. J Drug Deliv Sci Technol 2014;24:628–636.
[136] Deák Á, Janovák L, Csapó E, Ungor D, Pálinkó I, Puskás S, et al. Appl Surf Sci 2016;389:294–302.
[137] Zhang H, Guo J, Wang Y, Sun L, Zhao Y. Adv Sci 2021;8:2102156.
[138] Attri P, Kim YH, Park DH, Park JH, Hong YJ, Uhm HS, et al. Sci Rep 2015;5:9332.
[139] Merai L, Deak A, Sebok D, Csapo E, Kolumban TS, Hopp B, et al. Express Polym Lett 2018;12:1061–1071.
[140] Byrne J, Dunlop P, Hamilton J, Fernández-Ibáñez P, Polo-López I, Sharma P, et al. Molecules 2015;20:5574–5615.
[141] Ahmed SN, Haider W. Nanotechnology 2018;29:342001.
[142] Das K, Roychoudhury A. Front Environ Sci 2014;2. https://doi.org/10.3389/fenvs.2014.00053.

[143] Yu Y, Yang X, Zhao Y, Zhang X, An L, Huang M, et al. Angew Chemie Int Ed 2018;57:8550–8554.
[144] Gellé A, Moores A. Curr Opin Green Sustain Chem 2019;15:60–66.
[145] Georgiev P, Kaneva N, Bojinova A, Papazova K, Mircheva K, Balashev K. Colloids Surfaces A Physicochem Eng Asp 2014;460:240–247.
[146] Veres Á, Rica T, Janovák L, Dömök M, Buzás N, Zöllmer V, et al. Catal Today 2012;181:156–162.
[147] Tallósy SP, Janovák L, Nagy E, Deák Á, Juhász Á, Csapó E, et al. Appl Surf Sci 2016;371:139–150.
[148] Boldogkői Z, Csabai Z, Tombácz D, Janovák L, Balassa L, Deák Á, et al. Front Bioeng Biotechnol 2021;9. https://doi.org/10.3389/fbioe.2021.709462
[149] Zorba V, Chen X, Mao SS. Appl Phys Lett 2010;96:093702.
[150] Mérai L, Deák Á, Sebők D, Kukovecz Á, Dékány I, Janovák L. Polymers (Basel) 2020;12:1890.
[151] Liao W-P, Elliott IG, Faller R, Kuhl TL. Soft Matter 2013;9:5753.
[152] Dollimore D, Spooner P, Turner A. Surf Technol 1976;4:121–160.
[153] Simonsen ME, Sønderby C, Li Z, Søgaard EG. J Mater Sci 2009;44:2079–2088.
[154] Li X, Sun L, Ge A, Guo Y. Chem Commun 2011;47:947–949.
[155] Veres Á, Ménesi J, Juhász Á, Berkesi O, Ábrahám N, Bohus G, et al. Colloid Polym Sci 2014;292:207–217.
[156] Kőrösi L, Papp S, Ménesi J, Illés E, Zöllmer V, Richardt A, et al. Colloids Surfaces A Physicochem Eng Asp 2008;319:136–142.
[157] Awazu K, Fujimaki M, Rockstuhl C, Tominaga J, Murakami H, Ohki Y, et al. J Am Chem Soc 2008;130:1676–1680.
[158] Chaudhary D, Khare N, Vankar VD. Ceram Int 2016;42:15861–15867.
[159] Bayer I S, Steele A, Loth E. Chem Eng J 2013;221:522–530.
[160] Sánchez-Correa F, Vidaurre-Agut C, Serrano-Aroca Á, Campillo-Fernández AJ. J Appl Polym Sci 2018;135:46158.
[161] Hosokawa K, Sato K, Ichikawa N, Maeda M. Lab Chip 2004;4:181.
[162] Kameya Y, Yabe H. Coatings 2019;9:547.
[163] Tavana H, Simon F, Grundke K, Kwok DY, Hair ML, Neumann AW. J Colloid Interface Sci 2005;291:497–506.
[164] Fujishima A, Rao TN, Tryk DA. J Photochem Photobiol C Photochem Rev 2000;1:1–21.
[165] Zhang J, Wang J, Zhao Z, Yu T, Feng J, Yuan Y, et al. Phys Chem Chem Phys 2012;14:4763.
[166] Song K, Cui Y, Liu L, Chen B, Hirose K, Shahiduzzaman M, et al. Sci Rep 2022;12:1582.
[167] Zhang C, Chaudhary U, Das S, Godavarty A, Agarwal A. J Therm Spray Technol 2013;22:1193–1200.
[168] Solonenko OP, Ando Y, Nishiyama H, Kindole D, Smirnov AV, Golovin AA, et al. Surf Coatings Technol 2018;333:39–51.
[169] Nimlos MR, Wolfrum EJ, Brewer ML, Fennell JA, Bintner G. Environ Sci Technol 1996;30:3102–3110.
[170] Aarthi T, Narahari P, Madras G. J Hazard Mater 2007;149:725–734.
[171] Hoffman RL. J Colloid Interface Sci 1975;50:228–241.
[172] Dussan EB. Annu Rev Fluid Mech 1979;11:371–400.
[173] Wahl A, Augustynski J. J Phys Chem B 1998;102:7820–7828.
[174] Mejia JCM, Angeles L, Almanza R. Comput Water, Energy, Environ Eng 2014;03:36–40.
[175] Houas A. Appl Catal B Environ 2001;31:145–157.
[176] Tschirch J, Dillert R, Bahnemann D, Proft B, Biedermann A, Goer B. Res Chem Intermed 2008;34:381–392.
[177] Krasowska M, Zawala J, Malysa K. Adv Colloid Interface Sci 2009;147–148:155–169.
[178] Wu F, Liu W, Qiu J, Li J, Zhou W, Fang Y, et al. Appl Surf Sci 2015;358:425–435.
[179] Lantos E, Mérai L, Deák Á, Gómez- Pérez J, Sebők D, Dékány I, et al. J Mater Sci Technol 2020;41:159–167.
[180] Janovák L, Deák Á, Tallósy SP, Sebők D, Csapó E, Bohinc K, et al. Surf Coatings Technol 2017;326:316–326.
[181] Mehdizadeh Taheri S, Michaelis M, Friedrich T, Förster B, Drechsler M, Römer FM, et al. Proc Natl Acad Sci 2015;112:14484–14489.
[182] Hess DR. Respir Care 2000;45:609–622.
[183] Steckel H, Eskandar F. Eur J Pharm Sci 2003;19:443–455.
[184] Matyjaszewski K, Miller PJ, Shukla N, Immaraporn B, Gelman A, Luokala BB, et al. Macromolecules 1999;32:8716–8724.

[185] Merai L, Deak A, Szalai B, Samu GF, Katona G, Janovak L. Express Polym Lett 2022;16:34–51.
[186] Beamson G, Briggs D. High resolution XPS of organic polymers: The Scienta ESCA300 database. Wiley, New-York 1992
[187] Wagner CD. Anal Chem 1972;44:1050–1053.
[188] Wang Y, Zhong M, Zhang Y, Magenau AJD, Matyjaszewski K. Macromolecules 2012;45:8929–8932.
[189] Paterson E, Swaffield R. X-ray photoelectron spectroscopy. Clay Mineral. Spectrosc. Chem. Determ. Methods, Springer, Netherlands Dordrecht; 1994, p. 226–259. https://doi.org/10.1007/978-94-011-0727-3_6
[190] Biesinger MC, Lau LWM, Gerson AR, Appl Surf Sci 2010;257:887–898.
[191] Wang X. Sci China Ser B 2005;48:553.
[192] Fernández-Pérez A, Marbán G. ACS Omega 2020;5:29801–29815.
[193] Ahn C, Zeng X, Li L, Obendorf SK. Fash Text 2014;1:22.
[194] Xu H, Crick CR, Poole RJ. J Mater Chem A 2018;6:4458–4465.
[195] Verho T, Bower C, Andrew P, Franssila S, Ikkala O, Ras RHA. Adv Mater 2011;23:673–678.
[196] Li Y, Li Q, Zhang C, Cai P, Bai N, Xu X. Chem Eng J 2017;323:134–142.
[197] Wang L, Urata C, Sato T, England MW, Hozumi A. Langmuir 2017;33:9972–9978.

9. Appendices

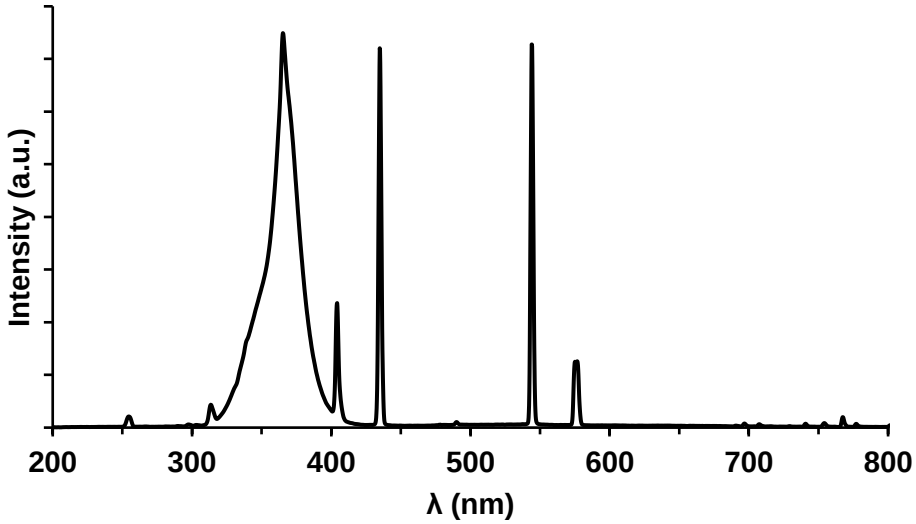

Figure A1. Emission spectrum of the UV light source, applied in the photoinitiation of HEA polymerization

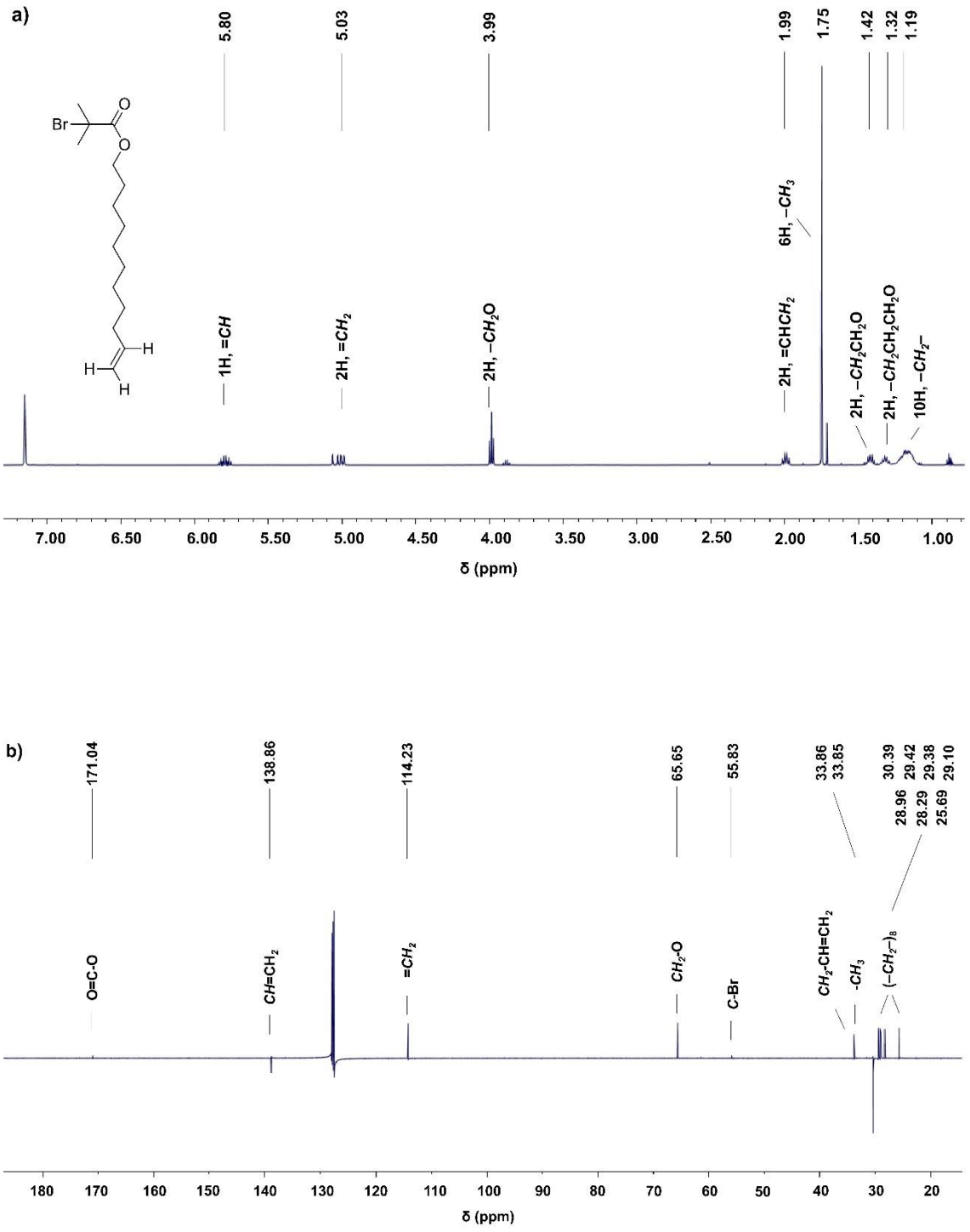

Figure A2. ^{1}H NMR **a)** and ^{13}C NMR **b)** spectra of 10-undecenyl 2-bromoisobutyrate (INI) recorded in C_6D_6 solvent

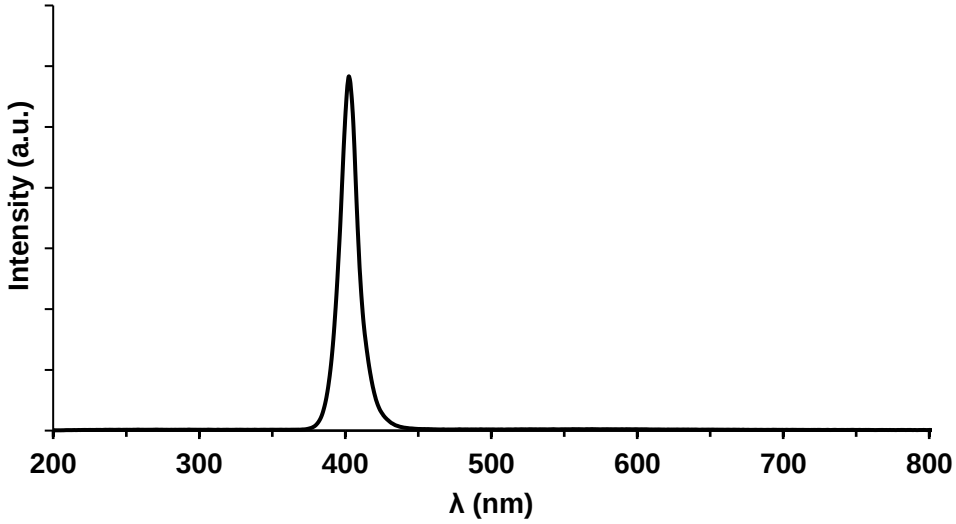

Figure A3. Emission spectrum of the LED light source, applied in photocatalytic experiments

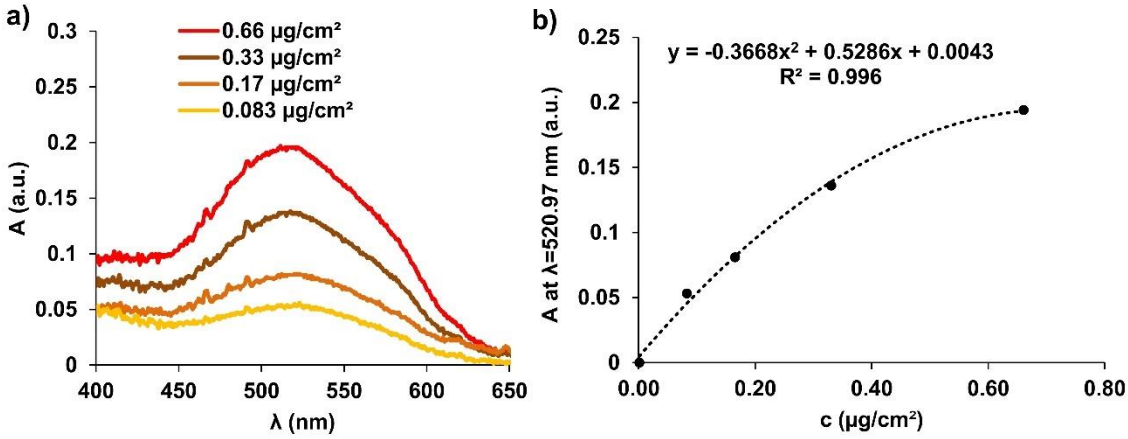

Figure A4. DR spectra of Sudan IV dye spots with different specific mass on r-FP surfaces **a)** and the calibration curve, determined accordign to the measured absorbance values at λ=520.97 nm **b)**

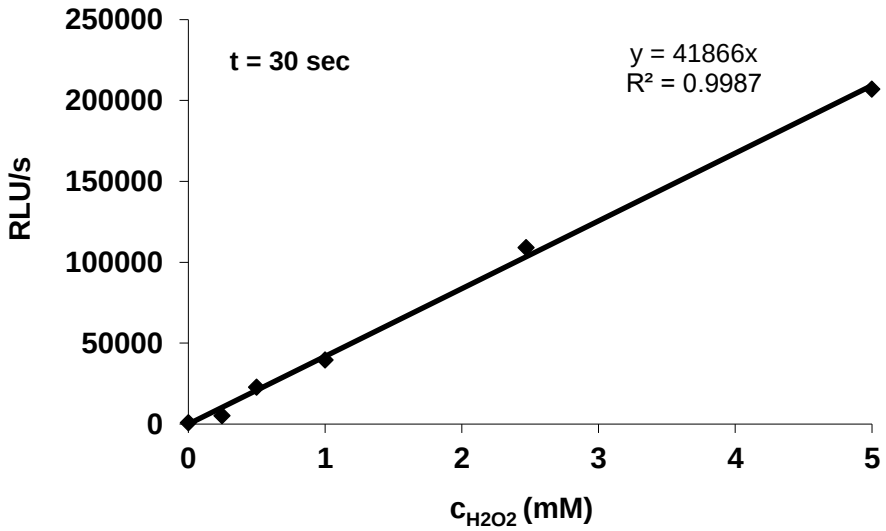

Figure A5. Luminometric calibration curve for the quantification of free radicals (Relative Light Unit/s vs. H_2O_2 concentration)

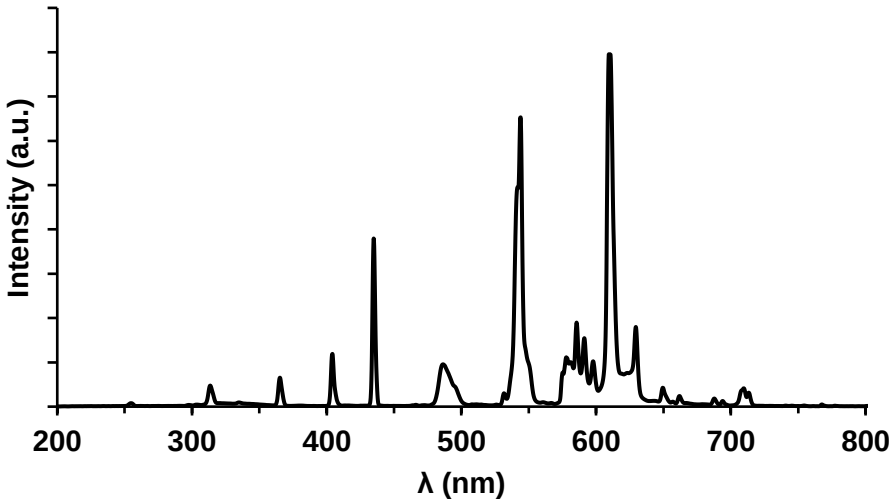

Figure A6. Emission spectrum of the UV light source, applied during luminometry measurements (15 W low pressure Hg gas lamp; λ_{max}=365 nm; LightTech, Hungary)

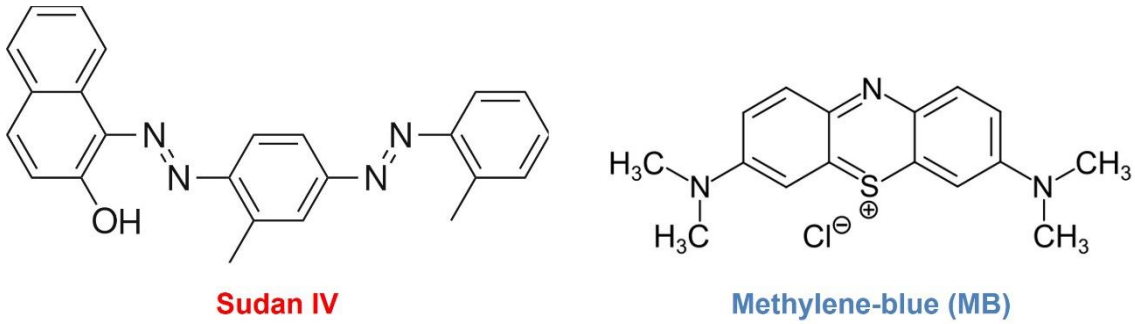

Figure A7. Structural formulas of Sudan IV and MB

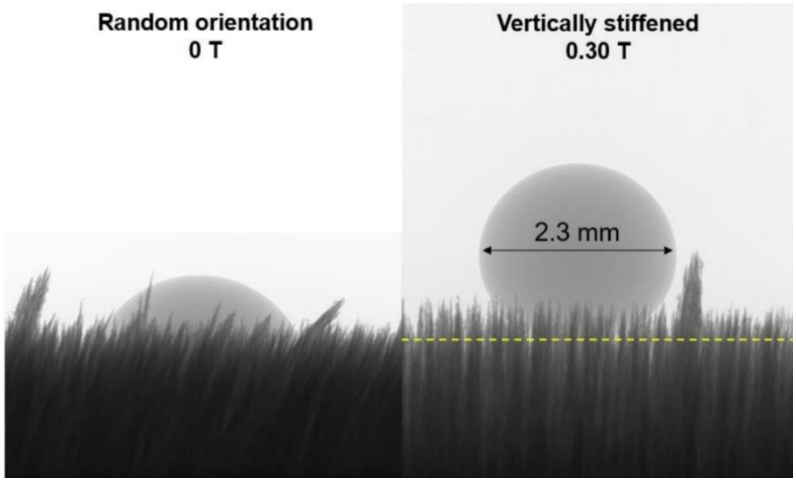

Figure A8. X-ray CT images of water drops on randomly oriented (left) and vertically stiffened (right) magnetic grasses with 16.7 wt.% nominal Ag-TiO_2 content [150]

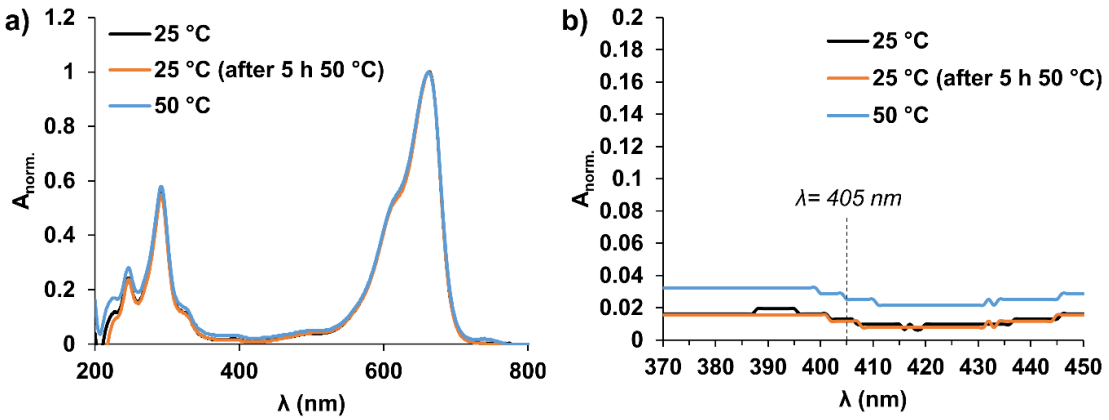

Figure A9. Normalized UV-VIS spectra of c_0= 2 mg/l (6.25 µM) MB solution at 25 °C, 50 °C and at 25 °C after 5 hours of storage at 50 °C **a)** and the absorptions at wavelengths near the emission wavelength (λ=405 nm) of the applied LED lightsource **b)**

Table A1. Characteristic XPS peaks of PDMS-based doctor blade-casted layers (1.2 wt% INI; 5 M NIPAAm)

Sample	**Peak maxima (eV)**				
	C 1s	**O 1s**	**Si $2p_{3/2}$**	**Br $3d_{5/2}$**	**Ti $2p_{3/2}$**
PDMS-co-INI	284.56	532.00	101.80	70.22	-
PDMS-gr-pNIPAAm	284.45	532.00	101.75	-	-
Ag- TiO_2/PDMS-gr-pNIPAAm	284.35	532.00	101.76	-	461.76
Literature value [115,186]	284.38	532.00 (BE ref)	101.79	70.50	458.50

Table A2. Elemental composition of different PDMS-based doctor blade-casted layers (1.2 wt% INI; 5 M NIPAAm) based on XPS spectral data

Element	**Elemental composition (at.%)**		
	PDMS-co-INI	PDMS-gr-pNIPAAm	Ag-TiO_2/PDMS-gr-pNIPAAm
Silicon	26.3	26.7	26.0
Oxygen	24.2	24.0	23.6
Carbon	49.4	49.3	50.2
Bromine	0.1	-	-
Titanium	-	-	0.2

Table A3. Elemental composition of different PDMS-based doctor blade-casted layers (1.2 wt.% INI; 5 M NIPAAm) based on EDX spectral data.

Element	**Elemental composition (at.%)**			
	PDMS-co-INI	Ag-TiO_2/PDMS-co-INI	PDMS-gr-pNIPAAm	Ag-TiO_2/PDMS-gr-pNIPAAm
Silicon	7.9	13.8	6.5	9.3
Oxygen	85.8	60.3	44.8	72.2
Carbon	6.3	25.7	31.2	6.3
Nitrogen	-	-	17.5	12.0
Titanium	-	0.2	-	0.2

10. Acknowledgements

Im am thankful for the support and guidance of my supervisor, ***Dr. László Janovák***, who not only instructed my doctoral work but gave me a free hand in implementing my own ideas, as well. I also owe special thanks to ***Prof. Dr. Imre Dékány***, who raised my interest in colloid and interface science and allowed me to join his group.

I would also like to thank ***Dr. Ágota Imre-Deák*** for conducting the S/G-photocatalytic tests, electron microscopy and profilometry measurements, ***Dr. Norbert Varga*** for conducting the preliminary study of the dissertation, and ***Zsuzsanna Hőrits*** for her technical assistance.

I am also thankful for the work of our cooperators, namely ***Dr. Gergely Ferenc Samu*** for the XPS study, ***Dr. Gábor Katona*** for the Raman-microscopy measurements, ***Dr. Dániel Sebők*** for conducting CT- and DR kinetic studies and ***Barnabás Molnár*** for NMR-spectra recording.

The work, as it is, could not be implemented without my co-supervised students ***Edina Balog*** and ***Balázs Szalai***, whom I also owe special thanks to.

Non-distinctively, I would like to say thank you for the helpfulness and the patience of our entire research group. My family also deserves an honorary mention: my studies could not have been carried out without their support.

I would also like to acknowledge the financial support of the grant GINOP-2.3.2-15-2016-00013 (Ministry of Human Capacities). The dissertation was prepared with the professional support of the Doctoral Student Scholarship Program of the Co-operative Doctoral Program of the Ministry of Innovation and Technology financed from the National Research, Development and Innovation Fund.

11. List of Publications

Hungarian Scientific Bibliography (MTMT) identifier: 10064997

Original research articles related to the PhD dissertation:

[1] **Mérai L**, Deák A, Sebok D, Csapó E, Kolumbán TS, Hopp B, et al. *Photoreactive composite coating with composition dependent wetting properties*. Express Polym Lett 2018;12:1061–71.
https://doi.org/10.3144/expresspolymlett.2018.93
IF=2.875

[2] **Mérai L**, Varga N, Deák Á, Sebők D, Szenti I, Kukovecz Á, et al. *Preparation of photocatalytic thin films with composition dependent wetting properties and self-healing ability*. Catal Today 2019;328:85–90.
https://doi.org/10.1016/j.cattod.2018.10.015
IF=5.875

[3] **Mérai L**, Deák Á, Sebők D, Kukovecz Á, Dékány I, Janovák L. *A Stimulus-Responsive Polymer Composite Surface with Magnetic Field- Governed Wetting and Photocatalytic Properties*. Polymers 2020;12:1890.
https://doi.org/10.3390/polym12091890
IF=4.329

[4] **Mérai L**, Deák Á, Szalai B, Samu GF, Katona G, Janovák L. *Visible light-photoreactive composite surfaces with thermoresponsive wetting and photocatalytic properties.* Express Polym Lett 2022;16:34–51.
https://doi.org/10.3144/expresspolymlett.2022.4
IF=3.952

Other publications:

[5] **Mérai L**, Imre-Deák Á, Dékány I, Janovák L. *Utilization of Solid/ Liquid Phase Boundary Interactions on functional surfaces: Fundamentals, Recent Advances and General Considerations – A Unifying Approach*. Adv Colloid Interface Sci 2022;303:102657. https://doi.org/10.1016/j.cis.2022.102657

IF=12.984

[6] Abdelghafour MM, Imre-Deák Á, **Mérai L**, Janovák L. *Photoreactive Composite Coatings with Tunable Surface Wetting Properties and Their Application Possibilities*, in Green Photocatalytic Semiconductors – Recent Advances and Apllications (Springer), Ed.: Garg S, Chandra A 2022, p. 209–56. https://doi.org/10.1007/978-3-030-77371-7_8 (book chapter)

[7] Janovák L, Dernovics Á, **Mérai L**, Deák Á, Sebők D, Csapó E, et al. *Microstructuration of poly(3-hexylthiophene) leads to bifunctional superhydrophobic and photoreactive surfaces*. Chem Commun 2018;54:650–3. https://doi.org/10.1039/C7CC07671A

IF=6.164

[8] Janovák L, Turcsányi Á, Bozó É, Deák Á, **Mérai L**, Sebők D, et al. *Preparation of novel tissue acidosis-responsive chitosan drug nanoparticles: Characterization and in vitro release properties of Ca^{2+} channel blocker nimodipine drug molecules.* Eur J Pharm Sci 2018;123:79–88. https://doi.org/10.1016/j.ejps.2018.07.031

IF=3.532

[9] Mótyán G, **Mérai L**, Kiss MA, Schelz Z, Sinka I, Zupkó I, et al. *Microwave-assisted synthesis of biologically relevant steroidal 17- exo -pyrazol-5'-ones from a norpregnene precursor by a side-chain elongation/heterocyclization sequence*. Beilstein J Org Chem 2018;14:2589–96. https://doi.org/10.3762/bjoc.14.236

IF=2.595

[10] Lantos E, **Mérai L**, Deák Á, Gómez- Pérez J, Sebők D, Dékány I, et al. *Preparation of sulfur hydrophobized plasmonic photocatalyst towards durable superhydrophobic coating material*. J Mater Sci Technol 2020;41:159–67. https://doi.org/10.1016/j.jmst.2019.04.046

IF=8.067

[11] **Mérai L**, Rajkumar T, Janovák L, Sápi A, Szenti I, Nagy L, et al. *Sulfur nanoparticles transform montmorillonite into an inorganic surfactant applicable in thermoplastics processing*. Polym Test 2020;85:106419.https://doi.org/10.1016/j.polymertesting.2020.106419

IF=4.282

[12] **Mérai L**, Janovák L, Kovács DS, Szenti I, Vásárhelyi L, Kukovecz Á, et al. Fast optical method for characterizing plasmonic nanoparticle adhesion on functionalized surfaces. Anal Bioanal Chem 2020;412:3395–404. https://doi.org/10.1007/s00216-019-02307-x

IF=4.157

[13] Abdelghafour MM, Deák Á, **Mérai L**, Ágoston Á, Bélteki R, Sebők D, et al. Photocatalytic elimination of interfacial water pollutants by floatable photoreactive composite nanoparticles. Environ Pollut 2020;266:115285. https://doi.org/10.1016/j.envpol.2020.115285

IF=8.071

[14] Kiss T, Katona G, **Mérai L**, Janovák L, Deák Á, Kozma G, et al. *Development of a Hydrophobicity-Controlled Delivery System Containing Levodopa Methyl Ester Hydrochloride Loaded into a Mesoporous Silica*. Pharmaceutics 2021;13:1039. https://doi.org/10.3390/pharmaceutics13071039

IF=6.290

[15] Janovák L, Deák Á, **Mérai L**, Tallósy S P, Dékány I. *Öntisztuló felületek alkalmazása szerves anyagok eliminálására, ill. biológiai rendszerek ártalmatlanítására*. Magy Kémiai Folyóirat. 2019;125:83–90. https://doi.org/10.24100/MKF.2019.02.83

[16] Janovák L, Deák Á, **Mérai L**, Dékány I. *Vízlepergető és fény hatására öntisztuló vékonyrétegek*. Magy Kem Lapja. 2018;2:48-52.

[17] Janovák L, Deák Á, **Mérai L**, Tallósy S P, Nagy E, Dékány I, *A nanorészecskék antimikrobiális hatásai*. Semmelweis felismerésének határokat áttörő üzenete – Semmelweis-emléknap tanulmánykötet, Pécsi Akadémiai Bizottság, Pécs, 2020, ISBN 978-963-429-466-5DOI: 10.15170/EKTK.2019.00002

All publications: ΣIF=73.382

Nyilatkozat

Alulírott ***Mérai László***, kijelentem, hogy a doktori értekezésemben foglaltak saját munkám eredményei, és csak a hivatkozott forrásokat (szakirodalom, eszközök, stb.) használtam fel.

Tudomásul veszem azt, hogy doktori értekezésemet a Szegedi Tudományegyetem könyvtárában, a kölcsönözhető könyvek között helyezik el.

aláírás

dátum